Numerical Modelling of Tides and Storm Surges in the Bay of Bengal

Thesis

submitted to

Goa University

for the Degree of

Doctor of Philosophy

in

Marine Sciences

by

Sindhu Mole

National Institute of Oceanography

Dona Paula, Goa – 403004, India

March 2012

Dedicated to ….....

Kaartic

Kanettan

Amma and Pappa

Statement

As required under the University Ordinance 0.19.8 (vi), I state that the present thesis entitled '**Numerical modelling of tides and storm surges in the Bay of Bengal**' is my original research work carried out at the National Institute of Oceanography, Goa and that no part thereof has been submitted for any other degree or diploma in any University or Institution.

The literature related to the problem investigated has been cited. Due acknowledgements have been made wherever facilities and suggestions have been availed of.

SINDHU MOLE

National Institute of Oceanography, Goa
March 2012

Certificate

This is to certify that the thesis entitled '**Numerical modelling of tides and storm surges in the Bay of Bengal**' submitted by **Sindhu Mole** for the award of the degree of Doctor of Philosophy in the Department of Marine Sciences is based on her original studies carried out by her under my supervision. The thesis or any part thereof has not been previously submitted for any degree or diploma in any University or Institution.

A S UNNIKRISHNAN

National Institute of Oceanography, Goa
March 2012

Acknowledgements

Thank you so much God for all your blessings.

Completing the Ph.D thesis has been probably the most challenging activity of my life. During the journey, I worked and acquainted with many people who contributed in different ways to the success of this study and made it an unforgettable experience for me. It is a pleasure to convey my gratitude to them.

First and foremost I would like to express my deep gratitude to my guide Dr A. S. Unnikrishnan, for all the patient guidance, stimulating suggestion and invaluable advices he has provided throughout my doctoral research endeavour. His insightful observations and constructive criticism helped me to establish the overall direction of the research and to move forward with investigation in depth.

I take this opportunity to sincerely acknowledge the Council of Scientific and Industrial Research for providing financial assistance in the form of Junior Research Fellowship and later Senior Research Fellowship.

I am thankful to Dr. S. R. Shetye the Director, NIO, for granting me permission to carry out work and utilize the facilities of the institute to accomplish my research work.

I wish to thank Dr. S. S. C. Shenoi, for his invaluable help and constructive comments on the work at the early stage of its development. I owe my sincere thanks to Dr. D. Shankar for his suggestions and advice.

I would like to thank Prof. G. N. Nayak, Prof. H. B. Menon, Department of Marine Sciences, Goa University and my co-guide Dr. Aftab Can for all their support on several occasions, both scientific and administrative.

It would have been difficult for me to shape up my manuscript on bathymetry without the help of Mr. Suresh. His timely and efficient contribution greatly enhanced the quality of the paper and I express my deepest appreciation for his assistance.

I would like to thank the Geodetic and Research Branch, Survey of India, Dehra Dun for providing the hourly tide gauge data.

Softwares such as GMT and GRASS-GIS have been used extensively in this thesis. I would like to express my gratitude to Mr. Michael for his willingness to

answer my queries on GMT anytime and for all his help and support during my stay in NIO. I appreciate the support received from Nagesh in learning GRASS-GIS.

My special thanks to Mr. Sundar, Mr. Simon, Mr. Vijayan, Mr. Sudeesh, Dr. Yatheesh and Mr. Mani Murali.

I extend my sincere thanks to Dr. Manoj who helped me to familiarize and understand the basic FORTRAN code used in numerical models. In addition, I am thankful to our system administrators Dattaram, Kaushik, Krupesh and Ashok for solving all computer related problems.

All my labmates at NIO made it a convenient place to work. I am extremely indebted to my friends Ricky, Suprit, Al Safany and Tejna for creating a friendly environment in the lab and helping me to get acquainted with Linux and Fortran. I express my special thanks to Dr. Aparna for providing valuable suggestions and comments on the thesis. The instant assistance from Nidheesh and Subeesh in expediting the simulation of the storm surges for revising the manuscript on storm surges deserves special mention. I thank Vijith for going through the thesis and providing valuable comments. I express my gratitude to them and to Soumya, Manu, Vinod, Remya and Vipin for all their help and support during my stay in Goa.

The informal support and encouragement of my dear friends Pallavi, Samrudhi and Pramila has been indispensible. I wish to thank my friends Nagaraju, Jagadish, Iqqu, Bajish, Saji, Vidya, Remya and Balu for their cheerful and enthusiastic company and support. Special thanks to my friends Swaroop, Noufara and Philip for the support and encouragement.

My acknowledgement will be incomplete if I do not express my gratitude and deep appreciation to my dearest friends Murali, Nisha, Ajay, Vijay, Aboobacker, Sini and Vineesh whose support and caring have enlightened and entertained me over the many years of friendship. Murali, Aboobacker and Nisha also went through the thesis and provided valuable comments and suggestions.

I cannot ask more from my Amma and Pappa, for being wonderful parents. Their love is my inspiration and driving force. They have given me their support

throughout, as always, for which my mere expression of thanks does not suffice. Binu, my dear brother, has always been very caring and supportive. I express my deepest gratitude to my in-laws for their unconditional support and care. I owe a huge debt of gratitude to Jayasree who took care of my son when I was busy with my research work.

Words fail me when it comes to acknowledge my soul mate, my shadow and light, my ever loving husband Krishnakumar. These past years have not been an easy ride for both of us; his sacrifice and patience are beyond words. I truly thank him for being my side even when I was irritated and depressed. I doubt that I will ever be able to convey my appreciation fully, but I owe him everything for being so patient, understanding and self-sacrificing.

Last but not least, it is time to admire my cute little son Kaartic, the most adorable gift of the God and for being so understanding at this small age. During the past years, I could not give my full attention and time to him. But he never complained or troubled and always allowed me to work with all his smiles. Therefore, now it is the time to compensate for all the lost days and embrace each and every moment of joy and happiness with him to the fullest. My life is meaningless without you, dear Kaartic.

Finally I would like to thank everybody who helped me directly or indirectly to the successful realization of this thesis.

SINDHU MOLE

National Institute of Oceanography, Goa
March 2012

Abstract

The massive destruction and loss of human life associated with a tropical cyclone can be attributed mainly to the sudden inundation and flooding of the coastal areas produced by storm surges. Storm surges are caused through the action of the high wind stress and pressure gradient. In addition, the phasing of astronomical tide relative to ocean surge is very critical. The most disastrous destruction often results when an extreme storm surge event occurs in conjunction with high tides, for example, during Bangladesh cyclone in 1970, the peak surge coincided with high tide killing more than 300000 people. Whereas a comparable surge in May 1963 occurred at low tide and hence was far less destructive. Thus real time monitoring and warning of storm surges in the Bay of Bengal are of great concern.

During the last few decades, much effort has been directed to the modelling of storm surges generated by intense cyclonic systems in the Bay of Bengal. A large number of location specific high resolution models have been developed to study the impact of cyclonic events along the coast of different countries in the Bay of Bengal and along the east coast of India. However, only a few attempts have been done to develop large scale storm surge models for the Bay of Bengal. Moreover, most of the storm surge models have been developed to simulate individual storm surge events. It is also essential to include tides in the storm surge model itself in order to obtain accurate estimates of total water level as the non-linear interactions between tides and storm surge affects the simulated water levels.

It is very well known that accurate bathymetric datasets are essential to produce reliable modelling results. A variety of bathymetric datasets with different coverage, resolutions, and accuracies are now available. Among these is the ETOPO5 [National Geophysical Data Centre (NGDC), 1988] that are now in wide use. ETOPO5 has been generated by digitizing the depth contours above 200 m from hydrographic charts. Subsequently, the ETOPO5 dataset is not reliable in regions where the depth values are less than 200 m. The shallow-water bathymetric data are usually collected and managed by regional organizations for regional interests. Hence the shallow-water bathymetric datasets are often not as

coordinated internationally and not as standardized as deep-water datasets. This leads to the use of different sources of bathymetry data by the ocean modellers.

Objectives of the present study are as follows

- Generate improved reliable bathymetric dataset for the continental shelf of the Indian Ocean.
- Simulation of tides and generation of co-range and co-tidal charts of the major semi-diurnal and diurnal constituents for the Bay of Bengal.
- Develop storm surge model to simulate total water levels and derive surges caused by low pressure systems identified during the past 27 years (1974-2000) in the Bay of Bengal.
- Estimation of return levels of extreme sea-level events at major coastal stations along the east coast of India.

Chapter 1 describes the background, area of study, motivation for the study and objectives.

Chapter 2 describes the numerical model used in the present study. The vertically integrated 2D model developed by Unnikrishnan et al. [1999] was used to simulate tides in the Bay of Bengal. The governing equations (equation of continuity and momentum equations), represented in Cartesian co-ordinates, were solved using an explicit finite difference scheme on an Arakawa C grid of resolution approximately 9.2 km. The time step chosen was 12 seconds to satisfy the Courant-Friedrichs-Lewy (CFL) criterion. The model domain extends from 1.5°N to 23°N and 79°E to 103°E with open boundaries along 79.8°E and 1.5°N.

The major input for the numerical model is bathymetry which can influence the accuracy of the simulated tides. In addition, accurate bathymetry of the bay is very essential to get accurate simulations of tides and surges as most of the coastal region bordering Bay of Bengal, especially the head bay, Gulf of Martaban and Malacca Strait, are very shallow and characterized by sudden change in depth contours. Hence, the bathymetry data for the present work was obtained from one of our recent works [Sindhu et al., 2007] in which improved shelf bathymetry for the Indian Ocean was prepared by digitizing the depth contours and sounding depths less than 200 m from the hydrographic charts published by the Naval

Hydrographic Office, India. The digitized data was then merged with the ETOPO5 dataset (masked for depths lower than 200 m) through appropriate blending techniques. The modified dataset showed significant improvements in many regions in the Bay of Bengal, such as the head bay, Gulf of Martaban, Malacca Strait and around Andaman Islands. Chapter 3 describes the methodology used in generating the modified shallow water bathymetry and the assessment of its improvements over original ETOPO5 dataset.

Chapter 4 describes the simulation of tides in the Bay of Bengal. The driving force for the tidal model was applied at the open boundaries in the form of composite tidal elevations derived from the global tidal model, FES2004. The time series of the simulated tidal elevations, extracted at selected grid points along the coast of Bay of Bengal, were harmonically analyzed using the TASK2000 software to extract the amplitude and phase of major semi-diurnal (M_2, S_2 and N_2) and diurnal constituents (K_1 and O_1), referred as model derived tidal constituents. The simulated tidal elevations covering a period of 30 days agreed fairly well with the observed hourly tide gauge data at Paradip, Visakhapatnam and Chennai, with root mean square error less than 7.5 cm. In addition, the amplitude and phase of the model derived major tidal constituents were compared with those obtained from Admiralty Tide Table (ATT) for 13 Standard Ports and 31 Secondary Ports and were found to agree favourably, with correlation coefficient of 0.99 for M_2, S_2 and N_2 and 0.92 for O_1.

The validated tidal model was used to simulate major tidal constituent separately in order to construct the co-range and co-tidal charts for the Bay of Bengal. The amplitudes of semi-diurnal tides increase from the southern boundary towards the northern coast of Bay of Bengal, with maxima in the head bay, Gulf of Martaban and Malacca Strait. The variation of the diurnal tides is small compared to the semi-diurnal tides.

The detailed analysis of the co-range charts reveals that semi-diurnal constituents (M_2, S_2, N_2) amplify in areas characterized by wide continental shelf (approximately 200 km) such as the head bay and along the southern coast of Myanmar, (the amplitudes are doubled), which is in agreement with Clarke and

Battisti [1981] theory. The diurnal constituent K_1 shows marginal amplification in these regions, but amplifies significantly in the north eastern end of the head bay. The head bay is also characterized by two degenerate amphidromic points. The geometrical configuration, in addition to the wide continental shelf, could contribute to the amplification of both semi-diurnal and diurnal tides in the north eastern end of head bay. The highest amplification of semi-diurnal is observed in the Gulf of Martaban and the diurnal tide K_1 also shows relatively significant amplification in this region, which could be due to its funnel shaped geometrical configuration and wide continental shelf. In the Malacca Strait, the amplitudes of semi-diurnal and diurnal tides increase towards the southern region. The diurnal constituents K_1 and O_1 have maximum amplitudes in the Malacca Strait. A virtual amphidromic point is also identified for M_2 tide in the Malacca Strait.

The forcing and the boundary conditions of the validated tidal model were appropriately defined to simulate the storm surges caused due to cyclones that affected the coast of Bay of Bengal, which is described in Chapter 5. The pressure field and the wind stress associated with low pressure systems (LPS) were estimated using Holland cyclone model. The parameters, such as the radius of maximum winds, core pressure and the position of the core of the cyclone required as input for Holland cyclone model, were obtained from Indian Daily Weather Report and Mausam, which are also documented in National Institute of Oceanography Report [2004] .

The storm surge model was forced with tides and meteorological forcing, simultaneously, former derived from FES2004 and applied along the open boundaries and latter estimated from Holland model for each of the 136 event and applied at each grid point of the model domain at every time step of the storm surge model. The tidal forcing was included in the storm surge model itself, rather than adding the individual tidal model output and the surge model output, in order to take into account the non-linear interaction between tides and surges. Therefore, the storm surge simulation gave the total sea level and the depth mean current due to combined effect of tide and meteorological forcing as output. In order to compute the storm surge component of total sea level, the storm surge model was

simulated with tidal forcing alone and the resulting tidal elevations were subtracted from the total sea level. The model results were validated by comparing the simulated level due to few selected cyclones that crossed the coast of Paradip, Visakhapatnam and Chennai with the observed hourly tide gauge data available at these locations and fairly good agreement was obtained.

The 5, 50 and 100-year return level for the total sea level and surge component were estimated for 26 stations along the east coast of India using the r-largest annual maxima method. The spatial variation of return levels of total sea level along the east coast of India shows an increase towards the head bay, the lowest being at Nagapattinam and the highest being at Sagar Island, which is similar to the increasing tidal range. However, the spatial variation of the return levels of surge component is found to be affected by shallow bathymetry and wide continental shelves. The variations in surge return levels along the east coast of India show that shallow and wide coastal shelves result in larger surges than deep and narrow shelves. At some regions in the southern part such as Surya Lanka and Machilipatnam, though 100-year return levels of total sea-level are not very high (3.17 m and 3.19 m, respectively) because of the relatively lower tidal ranges, high return levels of surge component (0.96 m and 0.66 m, respectively) are found. In addition to the role of shallow depths (5.0 and 6.1 m, respectively) at the two stations, the high return levels of surge component are attributed to the effect of geometrical configuration at Surya Lanka and width (100 km) and orientation of continental shelf at Machilipatnam. Similarly, the 100-year return levels of total water level at Chandipur is not high as that at Sagar Road, but the return level of surge component is found to be the highest due to its geometrical configuration.

The results described above are summarized in Chapter 6.

Contents

Statement iii

Certificate iv

Acknowledgements v

Abstract viii

List of Tables xvii

List of Figures xviii

1 Introduction 1

1.1 Overview 1

1.1.1 Tropical cyclones 1

1.1.2 Storm surges 2

1.1.3 Factors determining storm surge heights 3

1.1.4 Tides 4

1.1.5 Storm surge prediction methods 6

1.1.6 Extreme value analysis 7

1.2 Cyclones and storm surges in the Northern Indian Ocean 8

1.3 Area of study – Bay of Bengal 12

1.4 Storm surges in the Bay of Bengal 14

1.5 Motivation for the present study 15

1.6 Objectives 19

2 Model Description 21

2.1 Introduction 21
2.2 Governing equations 21
2.3 Finite difference formulation 22
2.3.1 Finite differencing of spatial derivative....23
2.3.2 Finite differencing of time derivative 24
2.3.3 Relation between grid spacing and time step 25
2.4 Finite difference form of governing equations....26
2.4.1 Treatment of continuity equation....27
2.4.2 Treatment of advective term 29
2.4.3 Treatment of Coriolis term 30
2.4.4 Treatment of pressure gradient term....30
2.4.5 Treatment of viscosity term 31
2.4.6 Continuity equation in finite difference form 31
2.4.7 Momentum equations in finite difference form....32
2.5 The initial and boundary conditions....36
2.5.1 Initial conditions 36
2.5.2 Closed boundary conditions 36
2.5.3 Open boundary conditions....38
2.6 Summary 41

3 Generation of bathymetric datasets for numerical model 42

3.1 Introduction 42
3.2 Data and methodology 45
3.2.1 Generation of improved bathymetric grids....45
3.2.2 Models used....50
3.3 Results and Discussions 51
3.3.1 Improvements in the modified bathymetry....51
3.3.2 Evaluation of the modified bathymetric datasets....53
3.4 Conclusion....59

4 Simulation of tides in the Bay of Bengal 60

4.1 Introduction 60
4.2 Data and methodology 61
4.2.1 Global Tidal Model - FES2004 61
4.2.2 Tidal Model for the Bay of Bengal 65
4.3 Tuning of the tidal model 73
4.4 Validation of the tidal model 74
4.4.1 Comparison with observed sea level data 74
4.4.2 Comparison with observed amplitudes and phases of tidal constituents 75
4.4.3 Statistical analysis to assess model performance 81
4.4.4 Comparison between simulated and predicted tides extracted from Indian Tide Tables 85
4.5 Simulation of tidal constituents 91
4.6 Co-range and co-tidal charts 91
4.6.1 General features 91
4.6.2 Characteristic features 98
4.7 Conclusions 111

5 Simulation of storm surges in the Bay of Bengal 113

5.1 Introduction 113
5.2 Data and methodology 114
5.2.1 Holland cyclone model 114
5.2.2 Storm surge model 115
5.2.3 Cyclone data for Holland model 117
5.2.4 Schematization 120
5.3 Validation of the storm surge model 125
5.3.1 The surge at Paradip due to 7 August 1981 cyclone 127
5.3.2 The surge at Paradip due to 3 June 1982 cyclone 127
5.3.3 The surge at Paradip due to 1 August 1984 cyclone 128
5.3.4 The surge at Visakhapatnam due to 25 November 1976 cyclone 128

5.3.5 The surge at Visakhapatnam due to 12 August 1986 cyclone.....129
5.3.6 The surge at Chennai due to 4 November 1978 cyclone.....129
5.4 Extreme sea level analysis.....131
5.4.1 Return periods of extreme events along the east coast of India ..133
5.5 Conclusions.....143

6 Summary **145**
6.1 Concluding remarks.....150
6.2 Future perspectives.....151

Bibliography **152**

Annexure: Published Papers **165**

List of Tables

1.1 Major tidal constituents. 5

1.2 Important shallow water tidal constituents 6

1.3 Nomenclature for Low Pressure Systems and their damage potential 10

1.4 Distribution of Cyclones and Severe Cyclones in the Bay of Bengal and Arabian Sea 11

1.5 List of major storm surges that affected the coast of Arabian Sea during 1782-1996 11

1.6 List of major storm surges that affected the coast of Bay of Bengal during 1937-1985 12

3.1 List of hydrographic charts used for digitization for different regions in the Indian Ocean 44

4.1 The name and location of 13 Standard Ports and 31 Secondary Ports as documented in the Indian Tide Tables and Admiralty Tide Tables, respectively 68

4.2 Error statistics for the model derived amplitudes and phases of the major tidal constituents. 85

4.3 The spring and neap tidal ranges at the 13 Standard Ports estimated from simulated tidal elevations 90

4.4 The shelf scale parameter (SP) and the amplification factor (AF) estimated for M_2, S_2, N_2 and K_1 at coastal stations 101

5.1 Error statistics for the simulated surge component at Paradip, Visakhapatnam and Chennai 131

5.2 The 5-year and the 50-year simulated return levels at 26 stations along the east coast of India 134

5.3 The return periods of pressure drop (Δp) for the cyclones in the Bay of Bengal 136

List of Figures

1.1 Map of the Bay of Bengal, including Andaman Sea and Malacca Strait, which forms the area of present study 16

1.2 The amplitudes of semi-diurnal and diurnal constituents at Chennai, Visakhapatnam, Paradip, Akyab, Sabang, and Sibolga 17

2.1 Schematic representation of variables η, h and H 23

2.2 General layout of Arakawa C grid showing distribution of variables η, u and v within a grid element 25

2.3 Definition of η, U and V point staggered on the computational $(\boldsymbol{i},\boldsymbol{j})^{\text{th}}$ grid element and the grids surrounding it 28

2.4 Schematic representation of the model grids showing the distribution of the variables used in the continuity equation to compute $\boldsymbol{\eta_{i,j}^{k+1}}$ 32

2.5 Schematic representation of the model grids showing the distribution of variables used to compute $\mathbf{U_{i,j}^{k+1}}$ in x-directed momentum equation 34

2.6 Schematic representation of the model grids showing the distribution of variables used to compute $\mathbf{V_{i,j}^{k+1}}$ in y-directed momentum equation 35

2.7 Approximation of actual coastal boundary into stair step configuration 37

3.1 Extent of different hydrographic charts used for digitization 47

3.2 A section of the ocean bottom topography off Paradip (20.167°N) showing comparison between different blending techniques 49

3.3 The difference in depths (anomaly) between the modified ETOPO5 and the original ETOPO5 dataset for the Indian Ocean. 52

3.4 The bathymetry obtained from the original and modified ETOPO5 for the head bay 54

3.5 The bathymetry obtained from the original and modified ETOPO5 for the Gulf of Martaban 55
3.6 The bathymetry obtained from the original and modified ETOPO5 for the Malacca Strait 55
3.7 The bathymetry obtained from the original and modified ETOPO5 for the Andaman Islands 56
3.8 Comparison of the observed sea surface elevation at Mumbai (Apollo Bandar) and Veraval with that simulated using original and the modified ETOPO5 57
3.9 The vertically averaged cross-shore and along-shore component computed from the observed current at Bombay High and that simulated using the original and the modified ETOPO5 58
4.1 Distribution of amplitude and phase of M_2 tide in the Bay of Bengal obtained from global tidal model (FES2004) 63
4.2 Distribution of amplitude and phase of S_2 tide in the Bay of Bengal obtained from global tidal model (FES2004). 63
4.3 Distribution of amplitude and phase of N_2 tide in the Bay of Bengal obtained from global tidal model (FES2004) 64
4.4 Distribution of amplitude and phase of K_1 tide in the Bay of Bengal obtained from global tidal model (FES2004) 64
4.5 Distribution of amplitude and phase of O_1 tide in the Bay of Bengal obtained from global tidal model (FES2004) 65
4.6 Scatter plot of the amplitudes of M_2, S_2, K_1 and O_1 extracted from FES2004 and that obtained from Admiralty Tide Tables at the 44 coastal stations 66
4.7 Model domain showing the 5 min computational grid and the location of 114 coastal stations at which the simulated tidal elevations were extracted 67
4.8 Model bathymetry 71
4.9 Comparison of simulated and observed tidal elevations at Paradip, Visakhapatnam, and Chennai 76

4.10 Comparison of the model derived and observed amplitudes of M_2, S_2, and N_2. 77
4.11 Comparison of the model derived and observed amplitudes of K_1 and O_1 78
4.12 Comparison of the model derived and observed phases '*g*' of M_2, S_2, and N_2 79
4.13 Comparison of the model derived and observed phases '*g*' of K_1 and O_1 80
4.14 Scatter plot of the model derived and observed amplitudes of M_2, S_2, K_1 and O_1 extracted at 44 stations 83
4.15 Scatter plot of the model derived and observed phases of the tidal constituents 84
4.16 Comparison of simulated tidal elevations with predicted high and low water levels obtained from Indian Tide Tables (ITT) at Trincomalee, Kakinada and Port Blair 86
4.17 Comparison of simulated tidal elevations with predicted high and low water levels obtained from ITT at Shortt Island and Sagar Roads. 87
4.18 Comparison of simulated tidal elevations with predicted high and low water levels obtained from ITT at Akyab, Amherst and Mergui 88
4.19 Comparison of simulated tidal elevations with predicted high and low water levels obtained from ITT at Pinang and Pelabuhan Klang 89
4.20 Co-range and co-tidal charts of M_2 tide for the Bay of Bengal 93
4.21 Co-range and co-tidal charts of S_2 tide for the Bay of Bengal 94
4.22 Co-range and co-tidal charts of N_2 tide for the Bay of Bengal 95
4.23 Co-range and co-tidal charts of K_1 tide for the Bay of Bengal 96
4.24 Co-range and co-tidal charts of O_1 tide for the Bay of Bengal 97
4.25 The amplification factor (AF) for M_2, S_2, N_2 and K_1 tide and the shelf width at different stations along the coast of Bay of Bengal 103

4.26 Detailed view of co-range and co-tidal chart of M_2 tide in the head bay, along the coast of Orissa and along the coast of Bangladesh.....104
4.27 Detailed view of co-range and co-tidal chart of S_2 tide in the head bay, along the coast of Orissa and along the coast of Bangladesh.....105
4.28 Detailed view of the co-range and co-tidal chart of M_2 along the coast of Myanmar.....106
4.29 Detailed view of the co-range and co-tidal chart of S_2 tide along the coast of Myanmar.....107
4.30 Detailed view of the co-range and co-tidal lines of M_2 in the Malacca Strait.....109
4.31 Detailed view of the co-range and co-tidal chart of S_2 tide M_2 in the Malacca Strait.....109
4.32 Detailed view of the co-range and co-tidal chart of K_1 tide. M_2in the Malacca Strait.....110
5.1 Monthly frequencies of cyclones classified as Depression, Deep Depression, Cyclone Storm and Super Cyclonic Storms for the period 1974 - 2000 118
5.2 Frequency distribution of core pressure and wind speed of cyclones identified during the period 1974 - 2000.....119
5.3 Tracks of cyclone that hit the eastern coast of India in different months during the period 1974-1982 121
5.4 Tracks of cyclone that hit the eastern coast of India in different months during the period 1983-1991 122
5.5 Tracks of cyclone that hit the eastern coast of India in different months during the period 1992-2000 123
5.6 Monthly frequencies of cyclones that hit the states of Tamil Nadu, Andhra Pradesh, Orissa and West Bengal located along the east coast of India during the period 1974–2000 124
5.7 Tracks of some selected cyclones that caused storm surges at Paradip, Visakhapatnam and Chennai 126

5.8 Comparison of the simulated total sea level and observed total sea level produced due to the selected cyclone events 130
5.9 A 3D view of the bathymetry along the east coast of India. 138
5.10 The 5-year return total sea level and surge level for 26 stations along the east coast of India 139
5.11 The 50-year return total sea level and surge level for 26 stations along the east coast of India 140
5.12 The 100-year return total sea level and surge level for 26 stations along the east coast of India 142

Chapter 1

Introduction

1.1 Overview

Storm surges are the fluctuations in water level generated during the passage of low pressure systems (LPS), such as tropical or extra-tropical cyclones, over a coastal or inland water body which can last up to a few days. Storm surges constitute one of the world's foremost natural disasters. A brief description of the general characteristics of tropical cyclones is given below, while the extra-tropical cyclones that usually form in the mid-latitudes is beyond the scope of the present study. The major factors that affect the height of storm surges and the methods used for the prediction of storm surges are also described in the following sections.

1.1.1 Tropical cyclones

Tropical cyclones are large revolving vortices with a ring of strong winds around a warm core and extending horizontally from 150-1000 km and vertically to about 12-14 km above sea level. The core has an average radius of about 20-30 km and is almost cloud free with light winds. It is surrounded by a wall of clouds (known as eye wall) arranged in the form of hollow cylinder rising up to an altitude of 15-18 km and a radial thickness of 10-15 km. This zone, though very narrow, constitutes the most hazardous zone as it is characterized by largest pressure gradient, strongest winds (V_{max}), heavy rainfall, high vertical velocity and strongest convection. The evolution of cyclones is defined in different stages from genesis to dissipation with a life of two to three weeks. The atmospheric and oceanographic conditions favourable for the formation of tropical cyclones are:

- Warm ocean waters with temperatures above 26.5°C to a minimum depth of 50 m;
- High amount of moisture at mid-troposphere elevations;
- An unstable atmosphere which cools rapidly with increasing altitude such that heated air parcels near the warm surface can rise freely into the atmosphere to cool down and condense;
- The presence of pre-existing near-surface disturbance to provide a localized spin (vorticity) and low level convergence;
- Significant Coriolis forces to rotate the cyclone;
- Relatively calm winds in the upper troposphere so that rising air columns and clouds can grow continuously into a vertical column without being cut off.

Tropical cyclones rotate counter-clockwise in the Northern Hemisphere and clockwise in the Southern Hemisphere. Tropical cyclones normally decay when they move into unfavourable environment such as land or over cooler waters in higher latitudes. The three major destruction causing hazards associated with the landfall of tropical cyclones are extreme wind speeds, heavy rains and storm surges.

1.1.2 Storm surges

The passage of cyclones over ocean surface impacts the surface elevation in two distinctly different ways. Firstly, the water surface responds to the pressure gradient associated with a cyclone through the *inverted barometer effect*, wherein a 1-hPa (mb) decrease of atmospheric pressure increases the sea level by about 1 cm [Pugh, 2004]. Secondly, drag forces, proportional to the square of wind speed, are generated at and parallel to the sea surface due to strong winds. These forces set up sea level gradient which result in a flow in the direction of wind in shallow waters. The impact of low pressure on sea surface elevation is minimal in comparison to the water being pushed towards the shore by the wind. These fluctuations in the sea surface elevations caused due to pressure gradient and strong winds are known as storm surges. The maximum surge height is produced when the cyclone crosses the coast [Murty et al., 1986].

1.1.3 Factors determining storm surge heights

The nature and magnitude of storm surges at a particular location depends upon the meteorological parameters associated with the tropical cyclone and the physical characteristics of the coastal areas. The meteorological factors affecting the height of storm surge include:

- The intensity of the cyclone, which is defined by the high horizontal pressure gradient and maximum wind speed attained at the eye wall.
- The forward speed of the cyclone - longer the storm stays at a location, larger will be the amount of transport and surge height. Due to the complimentary effect of forward motion and the counter-clockwise rotation of the cyclone in the Northern Hemisphere, highest (positive) surge for a cyclone occurs at the northeast quadrant of the storm's track. A negative surge may also occur on the northwest quadrant of the cyclone track due to offshore winds in this region.
- The radius of maximum winds which is measured radially from the cyclone centre to the location of highest wind speeds. Peak storm surge may vary drastically within a relative short distance along the coastline depending on the radius of maximum winds.
- The angle of approach to the coast; surge height is maximum for a tropical cyclone that moves onshore perpendicular to the coastline as this maximizes the onshore water transport.

The physical characteristics of a coastal area that influence the surge heights are:

- Bathymetry,
- Width of continental shelf,
- Configuration of coastline.

Another factor that determines the extent and severity of storm surges on coastal areas is the phase of the tide during which cyclone crosses the coast. If the peak surge elevation occurs at the time of high tide, the total sea level will be very high and will, thereby, produce the maximum impact. Hence, in order to estimate surge heights and their impact on coastal areas, information on the phase of tide at the time tropical cyclones crosses the coast is as important as the cyclone parameters.

1.1.4 Tides

Tides are the periodic oscillations in sea level produced by the combination of gravitational force of the moon and the sun and the centrifugal force generated as the earth rotates about the common centre of mass of earth-moon-sun system. Tides propagate as long waves on the rotating earth. The combined constraint of ocean basin geometry and the influence of the Coriolis force results in the development of amphidromic systems, in each of which the tidal wave rotates around the amphidromic point in counter-clockwise direction in the Northern Hemisphere and in clockwise direction in the Southern Hemisphere. The tidal range is zero at amphidromic point and increase outward away from it. The positioning of these points in an ocean basin depends on the geometry of the basin, including the coastal configuration and bathymetry, and they can even occur inland as degenerate amphidromic points.

Tides can be represented as a sum of N number of harmonic constituents. The major tidal constituents, their periods and angular speeds are tabulated in Table 1.1. The general form of representing each of the tidal constituent is

$$H_n cos(\omega_n t - g_n) \tag{1.1}$$

where, H_n is the amplitude, ω_n is the angular speed (related to period T_n as $\omega_n = 2\pi/T_n$), g_n is the phase lag of the observed constituent relative to the theoretical Equilibrium Tide obtained by adjusting 'G_n' to a particular time meridian. 'G_n' is the phase lag of the constituent on the Equilibrium Tide at Greenwich, in Greenwich Mean Time. The relation between the two phase lag is as follows:

$$G_n = g_n + T_z \omega_n \tag{1.2}$$

where T_z is the time zone defined as the shift in time at any place with respect to the Greenwich Mean Time.

The tides, however, behave differently as they enter small water bodies such as marginal seas and estuaries. The propagation of tides in these areas is affected by the shape of the marginal sea, bathymetry and configuration of sea bed (width and slope of continental shelf). As tides propagate into shallow waters, the non-linear mechanism causes transfer of tidal energy to other frequencies, which are

represented as shallow water tidal constituents known as overtides and compound tides (Table 1.2). The frequency of an overtide (such as M_4, M_6) is always an exact multiple of the frequency of the constituent that undergoes transformation in shallow waters. A compound tide results from the shallow-water interaction of two major tidal constituents (such as MS_4 is generated by the interaction of M_2 and S_2).

The propagation of tides in ocean and marginal seas can be represented by co-range and co-tidal charts of tidal constituents; the former helps to visualize the amplitudes of the tide while the latter provides a convenient way to illustrate the progression of tides. Co-range lines indicate locations where amplitudes of the tides are same. A co-tidal line connects locations where the phase of tide is same.

Table 1.1 Major tidal constituents [Pugh, 1987]

.

	Tidal species	Name	Speed (°/hour)	Period (hour)
Semi-diurnal	Principal lunar	M_2	28.9841	12.4206
	Principal solar	S_2	30.0000	12.0000
	Larger elliptical lunar	N_2	28.4397	12.6584
	Smaller elliptical lunar	L_2	29.5285	12.1916
	Declinational lunar	K_2	30.0821	11.9673
Diurnal	Luni-solar	K_1	15.0411	23.9344
	Principal lunar	O_1	13.9430	25.8194
	Principal solar	P_1	14.9589	24.0659
	Larger elliptical lunar	Q_1	13.3987	26.8684
	Elliptical lunar	J_1	15.5854	23.0984
	Smaller elliptical lunar	M_1	14.4920	24.8412
Long Period	Lunar semi-monthly	M_f	1.0980	327.85
	Lunar Monthly	M_m	0.5444	661.31
	Solar Annual	S_a	0.0411	8765.76
	Solar semi-annual	S_{sa}	0.0821	4383.05

Table 1.2 Important shallow water tidal constituents [Pugh, 1987].

Tidal species	Name	Speed (°/hour)
Long-period	Msf	1.016
Semi diurnal	$2SM_2$	31.016
	$2MS_2$	27.968
Fourth diurnal	M_4	57.968
	MS_4	58.984
	S_4	60.000
Sixth diurnal	M_6	86.952
	$2MS_6$	87.968

1.1.5 Storm surge prediction methods

The casualties and damages caused by storm surges can be limited if surges are predicted reasonably well in advance in order to implement effective warnings and evacuations of threatened areas. Earlier approaches for the prediction of surge heights included the use of empirical formulae that correlate the sea surface elevations with atmospheric pressure exerted on sea surface and strength and direction of prevailing winds [Rao and Mazumdar, 1966; Flierl and Robinson, 1972; Choudhury and Ali, 1974; Das et al., 1978; Qayyum, 1983; Chowdhury, 1994]. However, these methods require long term observation data to establish appropriate correlations.

The best approach is to apply numerical techniques to solve the vertically integrated form of the hydrodynamic equations [Murty et al., 1986; Dube et al., 1997]. It involves spatial discretization of the study area and the governing equations (equation of continuity and momentum equations) using either finite difference or finite element method and integration of the resulting equations over time using a suitable time stepping procedure. The numerical models based on these equations, which include non-linear interactions, is a most powerful method for practical prediction of surges especially for regions with complex bathymetry and coastline configuration. The accuracy in the simulation of storm surges using

numerical models depends on various input parameters such as storm characteristics, bathymetry, tides and representation of the coastal geometry. The implicit inclusion of tides in the storm surge model is essential to provide accurate estimates of total water level as the non-linear interactions between tides and storm surge affects the simulated water levels [Johns et al., 1985; McInnes et al., 2003].

1.1.6 Extreme value analysis

It is essential to quantify the risk of storm surges in order to formulate proper and effective risk management to mitigate the large scale damages caused due to storm surges. Once the heights of surges due to different cyclonic events in a coastal area are determined, it is possible to derive estimates of extreme sea levels; such as return periods, using statistical techniques. A return period is a statistical measurement, expressed as the reciprocal of the exceedance probability of an event, which denotes the average recurrence interval over an extended period of time. For instance, at a given location, the 50-year return period storm surge height being 2.46 m denotes that the probability of maximum surge height to exceed 2.46 m next year is only 0.2 (i.e., 1/50). Return period estimates are typically required for risk analysis and to design coastal protection structures which will be capable of withstanding an event of a certain return period.

The methods used for the estimation of exceedance probability are the annual maximum method [Jenkinson, 1955; Gumbel, 1958], r-largest annual maxima method [Smith, 1986; Tawn, 1988], joint probability method (JPM) [Pugh and Vassie, 1979], revised joint probability method (RJPM) [Tawn and Vassie, 1989] and exceedance probability method [Middleton and Thompson, 1986; Hamon et al., 1989]. Annual maximum method uses the annual maximum value in several years to fit a Generalized Extreme Value (GEV) distribution [Bury, 1999]. However, the disadvantage of the classical annual maximum method is the use of only the highest value of sea level in a year. Additionally, a successful application of the annual maximum method requires several years of data. In order to overcome the drawbacks, the r-largest annual maximum method

was developed by Smith [1986] and Tawn [1988], which allows to incorporate more than one maximum in a year and therefore more reliable estimates of return periods can be obtained using less number of years. The JPM involves the combination of individually estimated Probability Density Functions (*pdf*) of tide and surge. However, the nature of combination of the *pdf* depends on whether there is interaction between tide and surge. This method is not applicable at locations with short length of data and when the site is surge dominant. Later, the JPM was improved by Tawn and Vassie [1989] to obtain the revised joint probability method (RJPM). An alternative method of obtaining extreme sea level estimates from short data sets is the exceedance probability method (EPM).

1.2 Cyclones and storm surges in the Northern Indian Ocean

The cyclonic disturbances formed in the Northern Indian Ocean are categorized according to their maximum sustained wind speeds and each category has been assigned with different nomenclatures as defined by WMO [2010] and shown in Table 1.3. The expected damage potential of cyclones based on their intensities, as suggested by Attri and Tyagi [2010] is also summarized in Table 1.3. On an average, about 5 to 6 tropical cyclones generate every year in northern Indian Ocean, of which 2 or 3 could develop into severe cyclones, with more number of cyclones (4:1 ratio) developing in the Bay of Bengal than in the Arabian Sea [Dube et al., 1997]. Table 1.4, reproduced from Figure 1 of Niyas et al. [2009], shows the frequency of cyclones and severe cyclones in the Bay of Bengal and Arabian Sea during the last 118 years from1891 to 2008. Though Arabian Sea and Bay of Bengal are northward extension of Indian Ocean separated by Indian subcontinent with many physiographic similarities, some of the meteorological and oceanographic parameters are strikingly different which are responsible for higher frequencies of cyclogenesis over Bay of Bengal than Arabian Sea [Mooley and Shukla, 1989]. During the pre-monsoon season (April-May), the highest temperature is observed in the Northern Indian Ocean which remains to be above

28°C in the Bay of Bengal even after the onset of monsoon due to strong near-surface stratification and weaker winds in the Bay [Shenoi et al., 2004]. The high SST enhances the convective activities in the atmosphere. This, in turn, strengthens the near-surface stratification giving rise to a cyclic process with positive feedback. Shenoi et al. [2004] demonstrated that these favourable characteristics of the Bay are responsible for more cyclogenesis in the Bay of Bengal than in the Arabian Sea.

The months of October, November and December (post-monsoon season) are found to be principal season for cyclone formation over the Bay of Bengal, followed by the pre-monsoon months of March, April, and May [Attri and Tyagi, 2010]. Niyas et al. [2009] examined long term data from 1891 to 2008 and observed a decrease in the frequency of cyclone formation over the Bay of Bengal, with the maximum rate of decrease during monsoon season. However, in the months of May and November, they observed an increase in the frequency of cyclone formation. The tropical cyclones formed in the Bay of Bengal usually move toward west, north-west or north and finally curve towards east and move into north-east corner of the bay, and thereby, affecting the east coast of Sri Lanka and India, coast of Bangladesh, and north western coast of Myanmar.

Though the cyclones generated in the Northern Indian Ocean are weaker and smaller than those generated in Pacific and Atlantic Ocean, the death toll is highest. According to Frank and Hussain [1971], there were a total of 9-recorded cases of heavy human loss over past 300 years, in which 7 (77%) cases occurred in the Indian subcontinent. Among the destruction causing parameters associated with tropical cyclones, storm surges produce the major devastations. The destruction due to storm surge flooding is a serious concern along the coast of Bay of Bengal (Bangladesh, east coast of India, Myanmar, and Sri Lanka) and Arabian Sea (west coast of India, Pakistan and Oman). However, since the formation of cyclones in the Arabian Sea is less compared to that in the Bay of Bengal (Table 1.4), the frequency of storm surges affecting the coastline of Arabian Sea is lower than that affecting the coastline of Bay of Bengal. Still, a few major destructive surges have occurred along the eastern coast of Arabian Sea as well, particularly

along the coast of Pakistan and that of Gujarat (India) [Joseph et al., 2010]. Dube et al. [1997] had listed out the storm surges that caused major destruction and loss of life at different places along the coast of Arabian Sea during 1782-1996, which are shown in Table 1.5. A list of major storm surges that produced high death tolls along the east coast of India and the coast of Bangladesh, selected from Murty et al. [1986], is shown in Table 1.6.

Table 1.3 Nomenclature for Low Pressure System (LPS) defined by WMO [2010] and their damage potential as defined in Attri and Tyagi [2010].

Weather systems	Maximum wind speeds		Damage Expected
	V_{max} (knots)	V_{max} (km/hr)	
Low Pressure (LP)	< 17	< 31	
Depression (D)	17 – 27	31 – 51	
Deep Depression (DD)	28 – 33	52 – 61	Minor damage to loose and unsecured structures
Cyclonic Storm (CS)	34 – 47	62 – 88	Damage to thatched huts. Breaking of tree branches causing minor damage to power and communication lines
Severe Cyclonic Storm (SCS)	48 – 63	89 – 118	Extensive damage to thatched roofs and huts. Minor damage to power and communication lines due to uprooting of large avenue trees. Flooding of escape routes.
Very Severe Cyclonic Storm (VSCS)	64 – 119	119 – 221	Extensive damage to kachcha houses. Some damage to old buildings. Large-scale disruption of power and communication lines. Disruption of rail and road traffic due to extensive flooding. Potential threat from flying debris.
Super Cyclones	> 120	> 222	Extensive structural damage to residential and industrial buildings. Total disruption of communication and power supply. Extensive damage to bridges causing large scale disruption of rail and road traffic. Large-scale flooding and inundation of seawater. Air full of flying debris.

Table 1.4 Distribution of Cyclones and Severe Cyclones in the Bay of Bengal and Arabian Sea (from Niyas et al., [2009])

Month	Bay of Bengal		Arabian Sea	
	Cyclones	Severe Cyclones	Cyclones	Severe Cyclones
January	7	2	1	0
February	2	1	0	0
March	25	2	0	0
April	22	13	6	4
May	58	38	23	16
June	40	5	24	14
July	41	7	3	0
August	30	3	2	0
September	41	15	11	4
October	84	36	29	13
November	108	57	27	24
December	47	23	7	3
Total	**505**	**202**	**133**	**78**

Table 1.5 List of major storm surges that caused massive destruction and loss of life at different places along the coast of Arabian Sea during 1782-1996 [Dube et al., 1997].

Year	Month	Area of landfall	Area of major storms surges
1782	April	South Saurashtra coast	Gulf of Cambay
1851	May	32 km west of Karachi	Karachi
1920	June	Veraval	Gulf of Cambay
1964	June	Naliya	Gulf of Kutch
1975	October	Porbandar	Saurashtra
1977	November	Karwar	Karwar
1982	November	Veraval	Gulf of Cambay
1996	June	South Saurashtra coast	Gulf of Cambay

Table 1.6 List of storm surges that caused high death toll at different places along the coast of Bay of Bengal during 1737-1985 (selected from Murty et al. [1986]).

Year	Area of landfall	Area of major storms surges	Casualties
1737	Hooghly river	Sunderbans	300,000
1822	Bangladesh		40,000
1833	India		50,000
1864	West Bengal		50,000
1876	Bangladesh		200,000
1897	Bangladesh		175,000
1962	Bangladesh	Chittagong	50,000
1963	Bangladesh	Chittagong	50,000
1965	Chittagong	Comapaniganj	19,279
1970	Hatia, Bangladesh	Comapaniganj	300,000
1971	Paradip	Paradip	10,000
1977	Nizampatnam	Divi	10,000
1984	Karaikal, India	Karaikal	35,000
1985	Orissa	Balasore	11,069

1.3 Area of study – Bay of Bengal

Material destruction and loss of life is found to be very high due to storm surges at the coastal areas bordering the Bay of Bengal (Table 1.6), therefore, the present thesis deals with the analysis of characteristics of storm surges in the Bay of Bengal. The Bay of Bengal, including the Andaman Sea and Malacca Strait, lies roughly between latitudes 5°N and 23°N and longitudes 79.8°E and 102°E. It is bordered by eastern coast of Sri Lanka and India on the west, Bangladesh coast to the north, western coast of Myanmar (formerly known as Burma) and north western part of Malay Peninsula to the east. According to the limits defined by International Hydrographic Bureau (IHB), the Andaman and Nicobar Island separates the water eastward of it from the Bay of Bengal to form the Andaman Sea. The boundary of the Andaman Sea is considered to be a line running from Cape Negrais (16°03’N) through Andaman Islands to a point (10°48’N, 92°24’E)

in Little Andaman Island. In addition, the southern boundary of the Bay of Bengal is defined to extend from Dondra Head at the southern end of Sri Lanka in the west to a point (5°44'N, 95°04'E) at the northern tip of the Indonesian Island while the Adam's bridge between India and Sri Lanka represent the south eastern boundary. The bay is triangular in shape with the width decreasing from approximately 1600 km at the southern boundary to as narrow as 500 km at the northern end, which is commonly known as head bay. On the eastern side, along the coast of Myanmar, the bay narrows to Gulf of Martaban and on the south eastern end, the width of the bay is constrained by the coast of Malaysia and Indonesia to form the Malacca Strait. The Malacca Strait is connected to the South China Sea on its southern end. The Bay of Bengal and the major stations along the coastline of Bay of Bengal are shown in Figure 1.1.

The width of continental shelf varies considerably along the coastline bordering the Bay of Bengal. The continental shelf is very narrow off the east coast of India and north-western coast of Myanmar. However, the shelf becomes extensively wide at the head bay and along the south-western coast of Myanmar. The Gulf of Martaban and Malacca Strait represent shallow regions with average depths of 40 and 80 m, respectively.

In order to get an idea of the tidal amplitudes in the Bay of Bengal, we used the hourly tide gauge data at Chennai, Visakhapatnam and Paradip provided by the Survey of India and the GLOSS sea level data at stations along the coast of Myanmar (Akyab) and Indonesia (Sabang and Sibolga). The GLOSS/CLIVAR data is an online database (http://ilikai.soest.hawaii.edu/uhslc/ woce.html) distributed by UHSLC (University of Hawaii Sea Level Centre). We derived the tidal constituents at these stations using TASK2000, tidal analysis software. Among different semi-diurnal constituents that we had estimated for stations along the coastline of Bay of Bengal (Figure 1.2), the amplitudes of M_2, S_2 and N_2 are found to be relatively significant while among the diurnal constituents, K_1 and O_1 are significant. The variation in the tidal amplitudes along the coast of Bay of Bengal can be inferred from Figure 1.2. The M_2 amplitude is relatively higher at Akyab, located along the coast of Myanmar. The comparison of tidal amplitudes

at stations along the east coast of India (Figure 1.2a, b, and c), whose locations are shown in Figure 1.1, suggests that amplitudes of semi-diurnal and diurnal tides increase towards north. These large tidal heights, when combine with storm surges, can produce very high water level that have a potential of causing widespread destruction to life and property.

1.4 Storm surges in the Bay of Bengal

Rao [1968] classified the coastline bordering Bay of Bengal (mainly Indian coast) into three categories - A, B and C based on the amplitudes of maximum water levels attained at different coasts due to a hypothetical storm with wind speed of 40 m/s. The least dangerous zone with water level less than 2 m is classified as Zone A. The major portion of Tamil Nadu coast from 10°N to 14°N and that of Andhra Pradesh from 16°N to 20°N are assigned as Zone A. The east coast of India from 14°N to 16.5°N and the regions near the southern tip of Tamil Nadu (Coromandel Coast) are Zone B. The most dangerous zone is represented by Zone C (water level higher than 5 m) which extends to three locations along the east coast of India – north of 16°N covering the entire head bay, south Coromandel coast around Palk Bay, and a small area near Nizampatnam Bay. The high disastrous surges produced at these coastal areas can be attributed to the shallow bathymetry, geometrical configuration of the coastline, wide continental shelf, funnelling effect of the bay and favourable cyclone track. The high death toll can also be attributed to the high population, approximately 63 and 62 million, residing in the low-lying coastal areas of India and Bangladesh, respectively which are at high risks of flooding during cyclonic events [McGranahan et al., 2007]. The extent of damage at different places along the coast of Bay of Bengal was documented in earlier studies [Murty et al., 1986; Dube et al., 2000 a, b]. The most disastrous destruction often results when an extreme storm surge event occurs in conjunction with high tide, for example, during Bangladesh cyclone in November 1970, the peak surge of 5.6 m at Chittagong coincided with a high tide (2.1 m) killing more than 300,000 people. Whereas a comparable surge (5.0 m) in

May 1963 occurred at a low tide (0.3 m) and hence was far less destructive (50,000 deaths) [Murty et al., 1986].

1.5 Motivation for the present study

The meteorological parameters and the physical characteristics, referred in Section 1.1 are assessed to be favourable in the Bay of Bengal to amplify the storm surges which causes innumerable loss of life and damages to property. Therefore, an ability to predict surges, its development in time and derive the estimates of extreme sea level using the information on cyclone track and the parameters associated with a cyclone is clearly of great practical importance.

During the last few decades, much effort has been directed to the modelling of storm surges in the Bay of Bengal. Das [1972] pioneered the study of numerical storm surge modelling in India. Subsequently several successful attempts were made to simulate storm surges in the Bay of Bengal [Ghosh, 1977; Johns and Ali, 1980; Johns et al., 1981; Dube et al., 1985; Johns et al., 1985; Dube et al. 1994; Dube and Gaur, 1995], which have been extensively reviewed by Murty et al. [1986]. Flather [1994] applied a model with 1D equations for narrow channels and 2D equations for the open sea, i.e. the northern Bay of Bengal including the coast of Bangladesh to simulate the surge due to April 1991 cyclone. A few region-specific real time numerical surge models have been developed to study the impact of cyclonic events along the coast of different countries in the Bay of Bengal such as Sri Lanka [Chittibabu et al., 2002], Bangladesh [Jakobsen et al., 2006], and Myanmar [Jain et al., 2006]. A large number of location specific high resolution models have been developed and successfully applied to the regions covering maritime states along the east coast of India - Chittibabu et al. [2002] (Tamil Nadu) and Dube et al. [2000b] (Andhra Pradesh), Dube et al. [2000a, b] and Sinha et al. [2008] (Orissa), Dube et al. [2004] (head bay). Dube et al. [2009, 2013] carried out simulation of storm surges caused due to some recent severe cyclonic events such as Male (2006), Gonu (2007), Sudr (2007), Nargis (2008), and Aila (2009), Laila (2010), Giri (2010) and Thane (2011) that hit different coast bordering the Bay of Bengal.

Figure 1.1 Map of the Indian Ocean (top) and Bay of Bengal (bottom). The limits of Bay of Bengal, Andaman Sea and Malacca Strait, as defined by IHB, are demarcated (dotted blue line). The Bay of Bengal, including Andaman Sea and Malacca Strait, is the area of study. The major countries bordering the Bay of Bengal, the eastern maritime states of India and the major stations along the coastline of Bay of Bengal are also shown. The 200 m isobath is also demarcated (blue line).

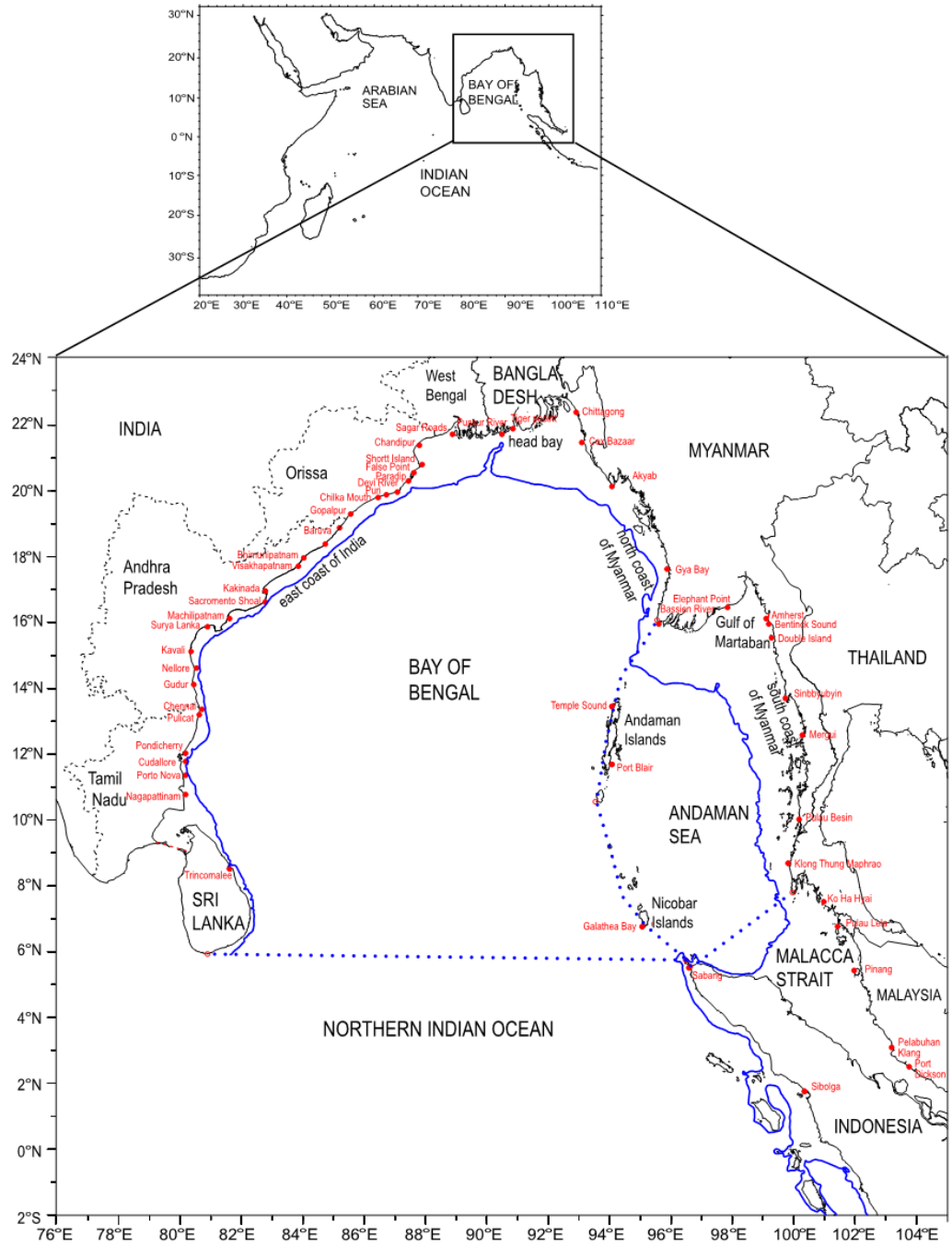

Figure 1.2 The amplitudes of semi-diurnal and diurnal constituents as obtained from harmonic analysis of observed sea level data available at a) Chennai, b) Visakhapatnam, c) Paradip, located along the east coast of India, d) Akyab, located along the northern coast of Myanmar, e) Sabang, and f) Sibolga located along the western coast of Indonesia. The location of these stations is shown in Figure 1.1.

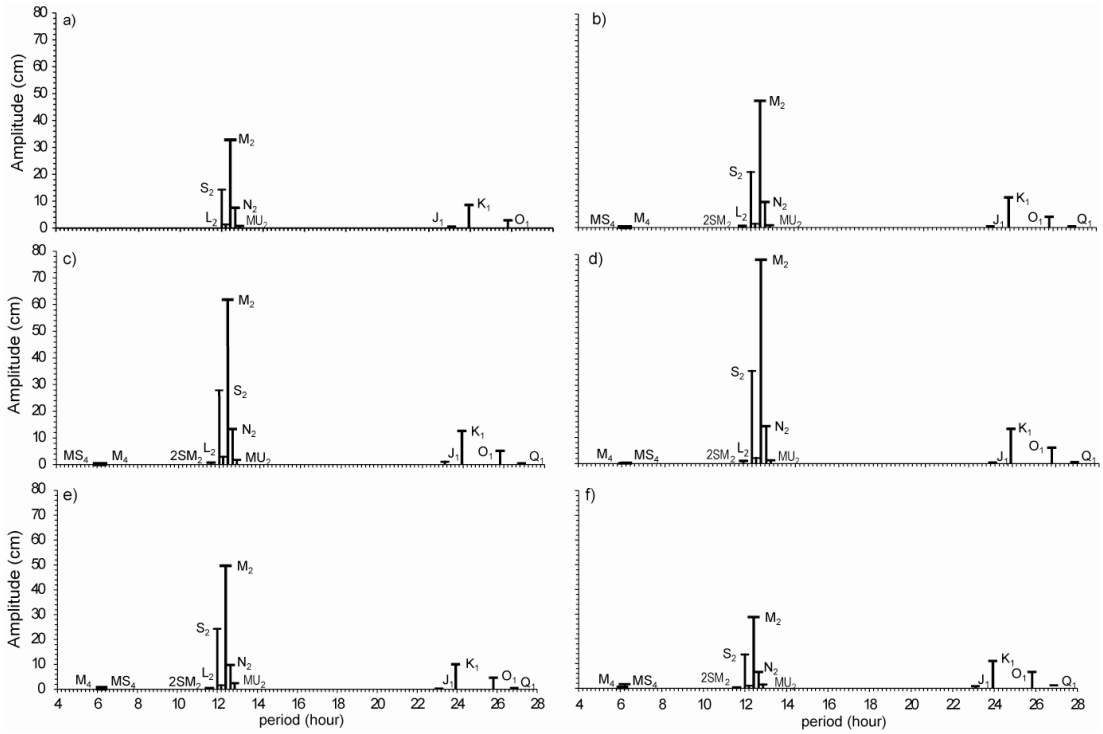

The domains of the above mentioned localized models are confined to the vicinity of the coastal areas. Therefore, it is noted that major effort, in the last decade, had been to develop location specific models except for a few attempts that have been done [for instance, Dube et al., 2006; Jain et al., 2007] to develop large scale storm surge models for the Bay of Bengal. Blain et al. [1994] showed that localized domain with boundaries at or near continental shelf appear to underestimate the surges at the adjacent coast. Moreover, most of the storm surge models have been developed to simulate individual storm surge events.

In addition, there have been a few attempts to make quantitative estimates of the return periods of storm surges along the east coast of India by analysing large number of cyclone events. Rao et al. [2010, 2012] simulated storm surges using synthesized cyclones with intensity equivalent to 50 yr RP and estimated the induced water level and extent of inundation in the Kalpakkam region and along the coast of Tamil. Jain et al. [2010] estimated the probale maximum total water level along the coast of Nellore district in Andhra Pradesh by simulating the surges associated with 1972, 1977, 1979, 1982, 1984, 1985, 1987, 1989 and 1990 cyclones affecting the Nellore coast.

Chittibabu et al. [2004] estimated return periods of storm surges along the coast of Orissa based on model results. Unnikrishnan et al. [2004] analyzed the hourly tide gauge data at three stations, Paradip, Visakhapatnam, and Chennai, for a period of 15 years (1974-1988) and estimated return levels for these stations.

The availability of tide gauge data only at 4-5 locations along the east coast of India and the rare occurrence of cyclone at a given tide gauge location, however, make the direct analysis of observational data very difficult. Moreover, during some of the intense cyclonic events, tide-gauges became non-functional. Consequently, there arises the necessity to use the numerically simulated storm surges for the analysis of the extreme events in the regions where tide gauge data are not available.

Since the surge height attained at a location is significantly affected by the state of tide, accurate information on tidal elevations at that location at the time when cyclones crosses the coast is very essential. Moreover, the detailed analysis

and understanding of the behaviour and characteristic features of tides in the Bay of Bengal is essential and beneficial to interpret the variations in the return periods of extreme events at different coastal stations bordering the Bay of Bengal. It has been found that a very few studies have been made regarding tides in the region. Murty and Henry [1983] developed co-tidal charts of tidal constituents M_2, S_2, K_1, and O_1 in the Bay of Bengal with the aid of numerical model. At that time, however, accurate information on open ocean tides was not available.

One of the major inputs for a numerical model is bathymetry which can influence the accuracy of the simulated tides. In addition, realistic representation of the bathymetry of the bay is very essential to simulate surge elevations accurately as most of the coastal region bordering the Bay of Bengal, especially the northern bay, are very shallow and characterized by sudden change in depth contours which can affect the surge heights considerably. The widely used bathymetric dataset ETOPO5 is assessed to be unreliable in regions where the depth values are less than 200 m.

1.6 Objectives

Objectives of the present study are as follows:

- Generate improved reliable bathymetric dataset for the continental shelf of the Indian Ocean.
- Simulation of tides and generation of co-range and co-tidal charts of the major semi-diurnal and diurnal constituents for the Bay of Bengal.
- Develop a storm surge model to simulate total water levels and surges caused by low pressure systems identified during the past 27 years (1974-2000) in the Bay of Bengal.
- Estimation of return levels of extreme events at major coastal stations along the east coast of India.

The thesis is organized as follows: The equation of continuity and the momentum equation and the numerical techniques used to solve these equations are described in Chapter 2. Chapter 3 is devoted to describe the generation of improved bathymetric datasets, which forms one of the major inputs for the tidal

model and the storm surge model. Chapter 4 documents the simulation of tides in the Bay of Bengal. The generation and detailed analysis of co-range and co-tidal charts for semi-diurnal and diurnal tidal constituents are also described in Chapter 4. The simulation of storm surges due to different LPS that crossed the coast of the Bay of Bengal and the estimation of return periods at different coastal stations along the east coast of India are described in Chapter 5. Finally, Chapter 6 summarizes and concludes the thesis.

Chapter 2

Model Description

2.1 Introduction

A two-dimensional (2D) vertically integrated model using a finite difference scheme was developed by Unnikrishnan et al. [1999] to simulate tides and tidal circulation on the shelf regions off the central west coast of India including the Gulf of Khambhat. We have used this 2D tidal model in the present study to simulate tides in the Bay of Bengal (as described in Chapter 4). After the validation of tidal model, we modified the model to simulate storm surges caused by cyclones (as described in Chapter 5).

The equation of continuity and momentum equations that describe the tide driven motion in shallow seas and the numerical techniques applied to solve these equations are presented in this chapter. The initial and boundary conditions are also discussed. In order to modify the tidal model to stimulate storm surges, the terms related to wind stress and the pressure field is included in the governing equations. This is described in Chapter 5.

2.2 Governing equations

The vertically integrated equation of continuity and momentum equations that govern the tidal model are as follows:

$$\frac{\partial \eta}{\partial t} + \frac{\partial U}{\partial x} + \frac{\partial V}{\partial y} = 0 \tag{2.1}$$

$$\frac{\partial U}{\partial t}+\frac{\partial}{\partial x}(uU)+\frac{\partial}{\partial y}(vU)-fV\ =-gH\frac{\partial \eta}{\partial x}\ -\frac{C_d U\sqrt{U^2+V^2}}{H^2}+A_H\left(\frac{\partial^2 U}{\partial x^2}+\frac{\partial^2 U}{\partial y^2}\right)$$

(2.2)

$$\frac{\partial V}{\partial t}+\frac{\partial}{\partial x}(uV)+\frac{\partial}{\partial y}(vV)+fU=-gH\frac{\partial \eta}{\partial y}\ -\frac{C_d V\sqrt{U^2+V^2}}{H^2}+A_H\left(\frac{\partial^2 V}{\partial x^2}+\frac{\partial^2 V}{\partial y^2}\right)$$

(2.3)

The symbols used in the above equations have the following meanings:

t	time (s), measured relative to the commencement of simulation,
x, y	rectangular Cartesian co-ordinates (m),
$\eta\ (x, y, t)$	free surface elevation (m) above Mean Sea Level (MSL),
$h\ (x, y)$	depth of sea bed below MSL (m),
$H\ (x, y, t)$	total depth of the sea bed (m), i.e, $H = h + \eta$,
$u\ (x, y, t)$	zonal component of vertically averaged velocity (ms^{-1}) over a depth H,
$v\ (x, y, t)$	meridional component of the vertically averaged velocity (ms^{-1}),
$U\ (x, y, t)$	x- directed vertically integrated transport (m^2s^{-1}), $U = \int_{-h}^{\eta} udz$,
$V\ (x, y, t)$	y - directed depth integrated transport (m^2s^{-1}), $V = \int_{-h}^{\eta} vdz$,
f	Coriolis parameter (s^{-1}), $f = 2\Omega sin\phi$,
Ω	Earth's angular velocity of rotation (s^{-1}) $\Omega \approx 2\pi/(3600 \times 23.9333)$,
$\phi\ (x, y)$	latitude north (°) ($\phi < 0$ in the Southern Hemisphere),
ρ	density of sea water, assumed constant at $\rho \approx 1027 kgm^{-3}$,
C_d	coefficient of bottom friction,
A_H	coefficient of horizontal eddy viscosity (m^2s^{-1}).

The variables η, h and $H$are illustrated in Figure 2.1. The above equations in terms of vertically integrated transport have been employed in the tidal models developed by Sinha and Mitra [1988], Moe et al. [2002], Le Provost and Fornerino [1985].

2.3 Finite difference formulation

This section describes the numerical techniques used to solve Equations (2.1), (2.2) and (2.3). The first step towards numerical modelling is discretization, a process of converting the differential equations to a set of algebraic equations that can be computed using a computer. In the present study, we have used the method

of finite differences to discretize the above partial differential hydrodynamic equations.

Figure 2.1 Schematic representation of η, h and H for a water column in Cartesian coordinate system.

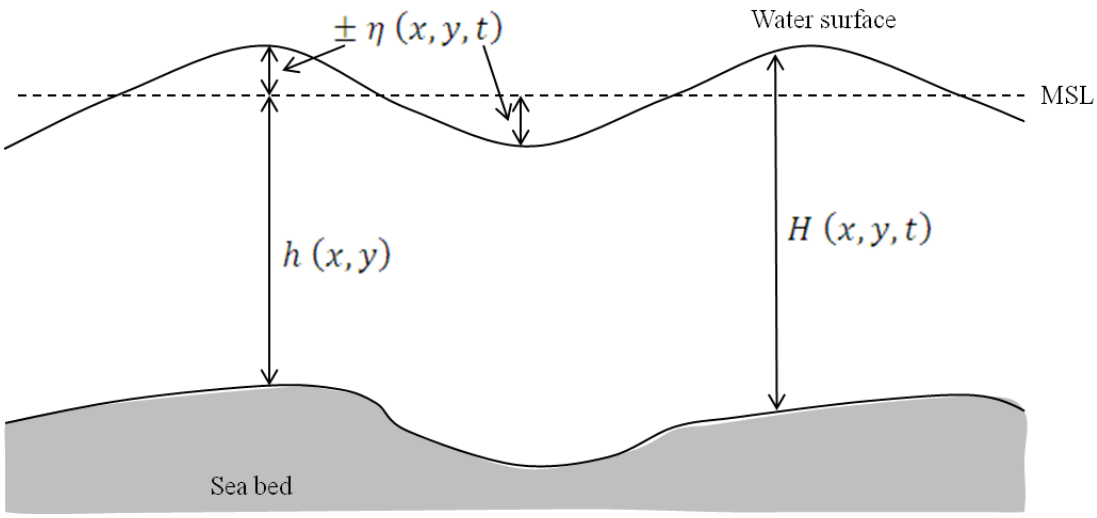

2.3.1 Finite differencing of spatial derivative

In the 2D model, the model domain is divided into uniform rectangular grids of fixed sizes in both x and y axes. The discretization procedure is elaborated as follows:

The horizontal x and y axes are divided into grids of uniform spacing Δx and Δy respectively, which results in a total of $M \times N$ grid elements. The position of any grid element inside the model domain is represented as (x_i, y_j), where

$$x_i = i\Delta x \qquad for \quad 1 \le i \le M \tag{2.4}$$

$$y_j = j\Delta y \qquad for \quad 1 \le j \le N \tag{2.5}$$

The variables, namely η, u and v in the depth integrated equations are spatially staggered on these grids such that the sea surface elevation η is defined at the centre of the grid element and the velocity components are defined on the

corresponding faces of the grid. This grid arrangement is known as Arakawa C grid, as shown in Figure 2.2. The vertically integrated transport variables U and V are defined at the respective positions of u and v. Among the various Arakawa grids B, D and E, Arakawa C is the most commonly used staggered grid. Mesinger and Arakawa [1976] assessed that Arakawa C grid provides a more accurate representation of differential operator than the non-staggered Arakawa A grid.

The partial difference equations defined in Section 2.2 are numerically solved by converting the equations into finite difference form for each discrete grid elements. In general, the spatial derivatives of free surface elevation η in the hydrodynamic equation at a grid (i,j) can be represented in finite difference form in the following three ways:

$$\frac{\partial \eta}{\partial x} \cong \frac{\eta_{i+1} - \eta_i}{\Delta x} \tag{2.6}$$

$$\frac{d\eta}{dx} \cong \frac{\eta_{i+1} - \eta_{i-1}}{2\Delta x} \tag{2.7}$$

$$\frac{d\eta}{dx} \cong \frac{\eta_i - \eta_{i-1}}{\Delta x} \tag{2.8}$$

The approximations shown in Equations (2.6), (2.7) and (2.8) are known as forward, central and backward difference scheme, respectively.

2.3.2 Finite differencing of time derivative

The continuity Equation (2.1) consists of time derivative of the η and the momentum Equations (2.2) and (2.3) consists of time derivatives of U and V, respectively. The time derivative terms are approximated using a centered differencing scheme known as leap-frog method. This scheme also known as midpoint rule is defined by three time levels (*k-1*, *k* and *k+1*).

$$\frac{\partial \eta}{\partial t} = \frac{\eta_i^{k+1} - \eta_i^{k-1}}{2\Delta t} \tag{2.9}$$

Though leap-frog method is a neutrally stable efficient scheme with second order accuracy, the main drawback is generation of two solution - the real solution defined by the physical properties of the model and the unphysical solution known as computational mode produced due to the three time level numerical scheme. The computational mode is eliminated in the model by applying a two-level scheme at every 10 or 20 time step as the two level schemes do not generate computational mode [Kowalik and Murty, 1993].

Figure 2.2 General layout of the Arakawa C grid showing the distribution of variables η, u and v within a grid element with ● representing η point, ✖ representing the u, U point and ■ representing the v, V point.

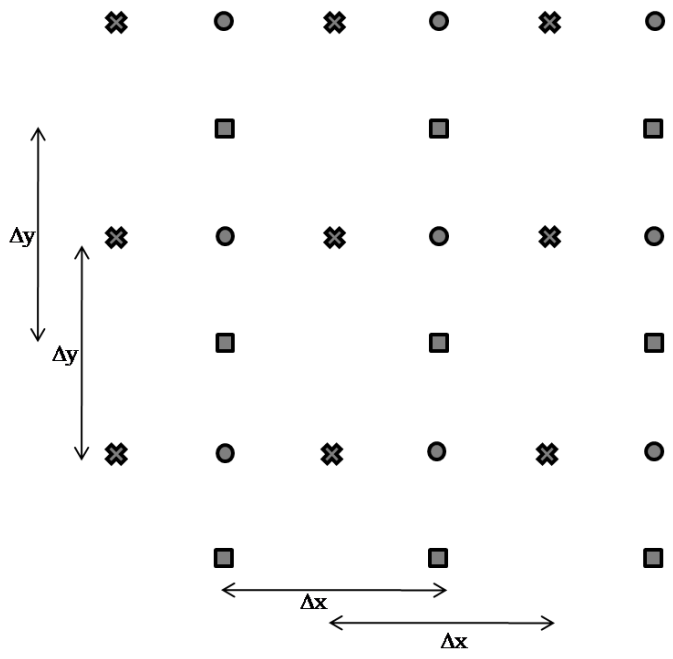

2.3.3 Relation between grid spacing and time step

The selection of grid spacing, Δx and Δy, depends on the size of the model domain and the resolution of the available bathymetric dataset. Though it is known that smaller grid sizes give more accurate results, the size of the grid spacing is limited by the time required for the simulation and availability of computational resources, such as computer memory capacity.

The temporal grid spacing, Δt, is determined based on the computational resources and the numerical stability criterion, which is related to the spatial grid spacing, Δx and Δy, selected for the model domain. The time step for the numerical model is selected so as to fulfil the Courant-Friedrichs-Levy (CFL) stability criteria, given as follows:

$$c\frac{\Delta t}{\sqrt{\Delta x^2 + \Delta y^2}} \leq 1 \tag{2.10}$$

which can be re-written using the expression for wave celerity $c = \sqrt{gh}$ as

$$\Delta t \leq \frac{\sqrt{\Delta x^2 + \Delta y^2}}{\sqrt{gh}} \tag{2.11}$$

2.4 Finite difference form of governing equations

The numerical techniques described in Section 2.3 are employed in the tidal model to transfer the governing equations into finite difference form, which is described in the following section. The discretization of the terms constituting the Equations (2.1), (2.2) and (2.3) is different as the locations at which the discrete variables are specified differ within a grid element defined in the Cartesian coordinate system (North pointed upward along the y-axis).

- The variables $\boldsymbol{\eta}_{i,j}$ and $\boldsymbol{h}_{i,j}$ for grid (i,j) at a time level k, are specified at the centre of the grid (i,j) symbolically represented by position $\left(i-\frac{1}{2}, j-\frac{1}{2}\right)$ and defined as η point

$$\boldsymbol{\eta}_{i,j}^{k} = \eta_{i-\frac{1}{2},j-\frac{1}{2}}^{k} \tag{2.12}$$

$$\boldsymbol{h}_{i,j} = h_{i-\frac{1}{2},j-\frac{1}{2}} \tag{2.13}$$

- The velocity component $\boldsymbol{U}_{i,j}$ and $\boldsymbol{u}_{i,j}$ for a $(i,j)^{th}$ grid at a time level k are positioned to the east of η point at the midpoint of the side parallel to y-axis symbolically represented by position $\left(i-\frac{1}{2},j-\frac{1}{2}\right)$ and specified as U point

$$\boldsymbol{U}_{i,j}^{k} = U_{i,j-\frac{1}{2}}^{k} \tag{2.14}$$

- The velocity component $\boldsymbol{V}_{i,j}$ and $\boldsymbol{v}_{i,j}$, for a $(i,j)^{th}$ grid at a time level k are specified to the north of η point at the midpoint of the parallel to x-axis symbolically represented by position $\left(i-\frac{1}{2},j-\frac{1}{2}\right)$ and is called as V point.

$$\boldsymbol{V}_{i,j}^{n} = V_{i-\frac{1}{2},j}^{k} \tag{2.15}$$

where $i = 2,M; j = 2,N; k = 1,K$

The discretization of the variables for the grid (i,j) and the surrounding grid is shown in Figure 2.3.

2.4.1 Treatment of continuity equation

The derivatives in Equation (2.1) are approximated into finite difference formulae using leap-frog method to march in time and centred differencing about the location of η point for a $(i,j)^{th}$ grid, which yield the following:

$$\left(\frac{\partial \eta}{\partial t}\right)_{i-\frac{1}{2},j-\frac{1}{2}}^{k} = \frac{\eta_{i-\frac{1}{2},j-\frac{1}{2}}^{k+1} - \eta_{i-\frac{1}{2},j-\frac{1}{2}}^{k-1}}{2\Delta t} = \frac{\boldsymbol{\eta}_{i,j}^{k+1} - \boldsymbol{\eta}_{i,j}^{k-1}}{2\Delta t} \tag{2.16}$$

$$\left(\frac{\partial U}{\partial x}\right)_{i-\frac{1}{2},j-\frac{1}{2}}^{k} = \left(\frac{\mathrm{U}_{\mathrm{i,j}-\frac{1}{2}}^{\mathrm{k}} - \mathrm{U}_{\mathrm{i}-1,\mathrm{j}-\frac{1}{2}}^{\mathrm{k}}}{\Delta \mathrm{x}}\right) = \left(\frac{\mathbf{U}_{\mathrm{i,j}}^{\mathrm{k}} - \mathbf{U}_{\mathrm{i}-1,\mathrm{j}}^{\mathrm{k}}}{\Delta \mathrm{x}}\right) \tag{2.17}$$

$$\left(\frac{\partial V}{\partial y}\right)_{i-\frac{1}{2},j-\frac{1}{2}}^{k} = \left(\frac{\mathrm{V}_{\mathrm{i}-\frac{1}{2},\mathrm{j}}^{\mathrm{k}} - \mathrm{V}_{\mathrm{i}-\frac{1}{2},\mathrm{j}-1}^{\mathrm{k}}}{\Delta \mathrm{y}}\right) = \left(\frac{\mathbf{V}_{\mathrm{i,j}}^{\mathrm{k}} - \mathbf{V}_{\mathrm{i,j}-1}^{\mathrm{k}}}{\Delta \mathrm{y}}\right) \tag{2.18}$$

Figure 2.3 Definition of η, U and V point staggered on the computational grid $(\boldsymbol{i}, \boldsymbol{j})$and the grids surrounding it. The positions of these points in terms of i, j are indicated symbolically.

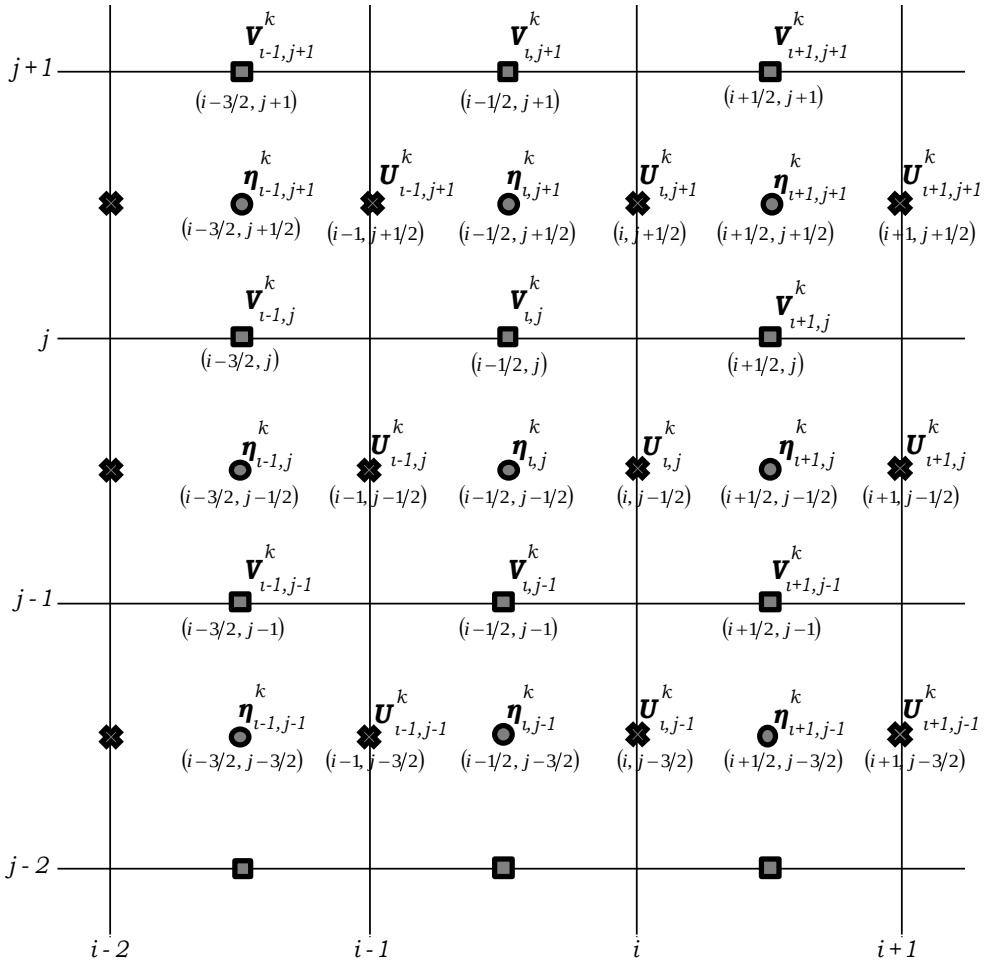

2.4.2 Treatment of advective term

The finite difference of the advective term in Equation (2.2) along x-direction is derived using centred differencing and averaging around the location of U point:

$$\left(\frac{\partial(uU)}{\partial x}\right)^{k}_{i,j-\frac{1}{2}} \approx \frac{1}{\Delta x}\left[(uU)^{k}_{i+\frac{1}{2},j-\frac{1}{2}} - (uU)^{k}_{i-\frac{1}{2},j-\frac{1}{2}}\right]$$

$$\approx \frac{1}{\Delta x}\left[u^{k}_{i+\frac{1}{2},j-\frac{1}{2}} U^{k}_{i+\frac{1}{2},j-\frac{1}{2}} - u^{k}_{i-\frac{1}{2},j-\frac{1}{2}} U^{k}_{i-\frac{1}{2},j-\frac{1}{2}}\right]$$

$$\approx \frac{1}{\Delta x}\left[\left(\frac{u^{k}_{i+1,j-\frac{1}{2}} + u^{k}_{i,j-\frac{1}{2}}}{2}\right)\left(\frac{\mathrm{U}^{k}_{i+1,j-\frac{1}{2}} + \mathrm{U}^{k}_{i,j-\frac{1}{2}}}{2}\right)\right.$$

$$\left. -\left(\frac{u^{k}_{i,j-\frac{1}{2}} + u^{k}_{i-1,j-\frac{1}{2}}}{2}\right)\left(\frac{\mathrm{U}^{k}_{i,j-\frac{1}{2}} + \mathrm{U}^{k}_{i-1,j-\frac{1}{2}}}{2}\right)\right]$$

$$= \frac{1}{\Delta x}\left[\frac{1}{4}\left(\boldsymbol{u}^{k}_{i+1,j} + \boldsymbol{u}^{k}_{i,j}\right)\left(\mathbf{U}^{k}_{i+1,j} + \mathbf{U}^{k}_{i,j}\right)\right.$$

$$\left. -\frac{1}{4}\left(\boldsymbol{u}^{k}_{i,j} + \boldsymbol{u}^{k}_{i-1,j}\right)\left(\mathbf{U}^{k}_{i,j} + \mathbf{U}^{k}_{i-1,j}\right)\right] \qquad (2.19)$$

$$\left(\frac{\partial(vU)}{\partial y}\right)^{k}_{i,j-\frac{1}{2}} \approx \frac{1}{\Delta y}\left[(vU)^{k}_{i,j} - (vU)^{k}_{i,j-1}\right]$$

$$\approx \frac{1}{\Delta y}\left[v^{k}_{i,j} U^{k}_{i,j} - v^{k}_{i,j-1} U^{k}_{i,j-1}\right]$$

$$\approx \frac{1}{\Delta y}\left[\left(\frac{v^{k}_{i+\frac{1}{2},j} + v^{k}_{i-\frac{1}{2},j}}{2}\right)\left(\frac{U^{k}_{i,j+\frac{1}{2}} + U^{k}_{i,j-\frac{1}{2}}}{2}\right)\right.$$

$$\left. -\left(\frac{v^{k}_{i+\frac{1}{2},j-1} + v^{k}_{i-\frac{1}{2},j-1}}{2}\right)\left(\frac{U^{k}_{i,j-\frac{1}{2}} + U^{k}_{i,j-\frac{3}{2}}}{2}\right)\right]$$

$$= \frac{1}{\Delta y}\left[\frac{1}{4}\left(\boldsymbol{v}^{k}_{i+1,j} + \boldsymbol{v}^{k}_{i,j}\right)\left(\boldsymbol{U}^{k}_{i,j+1} + \boldsymbol{U}^{k}_{i,j}\right)\right.$$

$$\left. -\frac{1}{4}\left(\boldsymbol{v}^{k}_{i+1,j-1} + \boldsymbol{v}^{k}_{i,j-1}\right)\left(\boldsymbol{U}^{k}_{i,j} + \boldsymbol{U}^{k}_{i,j-1}\right)\right] \qquad (2.20)$$

The finite difference of the advective term in y-directed momentum Equation (2.3) is derived following similar procedures using centred differencing and centred space averaging for the derivates, but around the location of *V* point.

2.4.3 Treatment of Coriolis term

The coriolis term in Equations (2.2) and (2.3) requires evaluation of V (y-directed depth integrated transport) at a *U* point and evaluation of U (x-directed depth integrated transport) at a V point respectively. This is achieved through centered averaging of V defined at the four *V* points surrounding the *U* point for Equation (2.2);

$$fV^k_{i,j-\frac{1}{2}} \approx f\left(\frac{V^k_{i+\frac{1}{2},j-\frac{1}{2}} + V^k_{i-\frac{1}{2},j-\frac{1}{2}}}{2}\right)$$

$$\approx \frac{f}{2}\left(\frac{V^k_{i+\frac{1}{2},j} + V^k_{i+\frac{1}{2},j-1}}{2} + \frac{V^k_{i-\frac{1}{2},j} + V^k_{i-\frac{1}{2},j-1}}{2}\right)$$

$$\approx \frac{f}{4}\left(\boldsymbol{V}^k_{i+1,j} + \boldsymbol{V}^k_{i+1,j-1} + \boldsymbol{V}^k_{i,j} + \boldsymbol{V}^k_{i,j-1}\right) \qquad (2.21)$$

A similar approach is taken to define *U* at *V* point for Equation (2.3).

2.4.4 Treatment of pressure gradient term

The pressure gradient term in Equations (2.2) and (2.3) is represented with total depth and space derivative of η. In the adopted Arakawa C grid, the total depth $H = (h + \eta)$, a function of both space and time, is prescribed at the η point. Therefore, depth at U point at a time level k for Equation (2.2) is defined by centred averaging:

$$\left(gH\frac{\partial \eta}{\partial x}\right)^k_{i,j-\frac{1}{2}} \approx g\left(\frac{H^k_{i+\frac{1}{2},j-\frac{1}{2}} + H^k_{i-\frac{1}{2},j-\frac{1}{2}}}{2}\right)\left(\frac{\eta^k_{i+\frac{1}{2},j-\frac{1}{2}} - \eta^k_{i-\frac{1}{2},j-\frac{1}{2}}}{\Delta x}\right)$$

$$= g\left(\frac{\boldsymbol{H}^k_{i+1,j} + \boldsymbol{H}^k_{i,j}}{2}\right)\left(\frac{\boldsymbol{\eta}^k_{i+1,j} - \boldsymbol{\eta}^k_{i,j}}{\Delta x}\right)$$

$$= g\left(\frac{\boldsymbol{h}_{i,j} + \boldsymbol{h}_{i+1,j} + \boldsymbol{\eta}^k_{i,j} + \boldsymbol{\eta}^k_{i+1,j}}{2}\right)\left(\frac{\boldsymbol{\eta}^k_{i+1,j} - \boldsymbol{\eta}^k_{i,j}}{\Delta x}\right) \qquad (2.22)$$

2.4.5 Treatment of viscosity term

The eddy viscosity terms in Equations (2.2) and (2.3) involve second order derivatives, which can be approximated using centred differencing about the position.

$$\left(\frac{\partial^2 U}{\partial x^2}\right)^k_{i,j-\frac{1}{2}} \approx \frac{\mathrm{U}^k_{i+1,j-\frac{1}{2}} - 2\mathrm{U}^k_{i,j-\frac{1}{2}} + \mathrm{U}^k_{i-1,j-\frac{1}{2}}}{(\Delta x)^2}$$

$$= \left(\frac{\mathbf{U}^k_{i+1,j} - 2\mathbf{U}^k_{i,j} + \mathbf{U}^k_{i-1,j}}{(\Delta x)^2}\right) \tag{2.23}$$

$$\left(\frac{\partial^2 U}{\partial y^2}\right)^k_{i,j-\frac{1}{2}} \approx \frac{\mathrm{U}^k_{i,j+\frac{1}{2}} - 2\mathrm{U}^k_{i,j-\frac{1}{2}} + \mathrm{U}^k_{i,j-\frac{3}{2}}}{(\Delta y)^2}$$

$$= \frac{\mathbf{U}^k_{i,j+1} - 2\mathbf{U}^k_{i,j} + \mathbf{U}^k_{i,j-1}}{(\Delta y)^2} \tag{2.24}$$

2.4.6 Continuity equation in finite difference form

The continuity equation in finite difference form is as follows

$$\boldsymbol{\eta}^{k+1}_{i,j} = \boldsymbol{\eta}^{\mathrm{k}-1}_{\mathrm{i,j}} - 2\Delta t\left(\frac{\mathbf{U}^{\mathrm{k}}_{\mathrm{i,j}} - \mathbf{U}^{\mathrm{k}}_{\mathrm{i}-1,\mathrm{j}}}{\Delta \mathrm{x}} + \frac{\mathbf{V}^{\mathrm{k}}_{\mathrm{i,j}} - \mathbf{V}^{\mathrm{k}}_{\mathrm{i,j}-1}}{\Delta \mathrm{y}}\right) \tag{2.25}$$

Equation (2.25) represents the explicit numerical method as the equation at any spatial grid location includes only one unknown variable $\eta^{k+1}_{i,j}$. The unknown variable $\eta_{i,j}$ at new time step *(k+1)* is computed from the 3 known value at previous time levels *k* and *k-1*. The variables used in Equation (2.25) to compute $\boldsymbol{\eta}^{k+1}_{i,j}$ and their distribution on the Arakawa C grid with respect to grid (i,j) are shown in Figure 2.4.

Figure 2.4 Schematic representation of the distribution of η, U and V points that are used in Equation (**2.1**) to compute $\boldsymbol{\eta}_{\mathbf{i,j}}^{\mathbf{k+1}}$

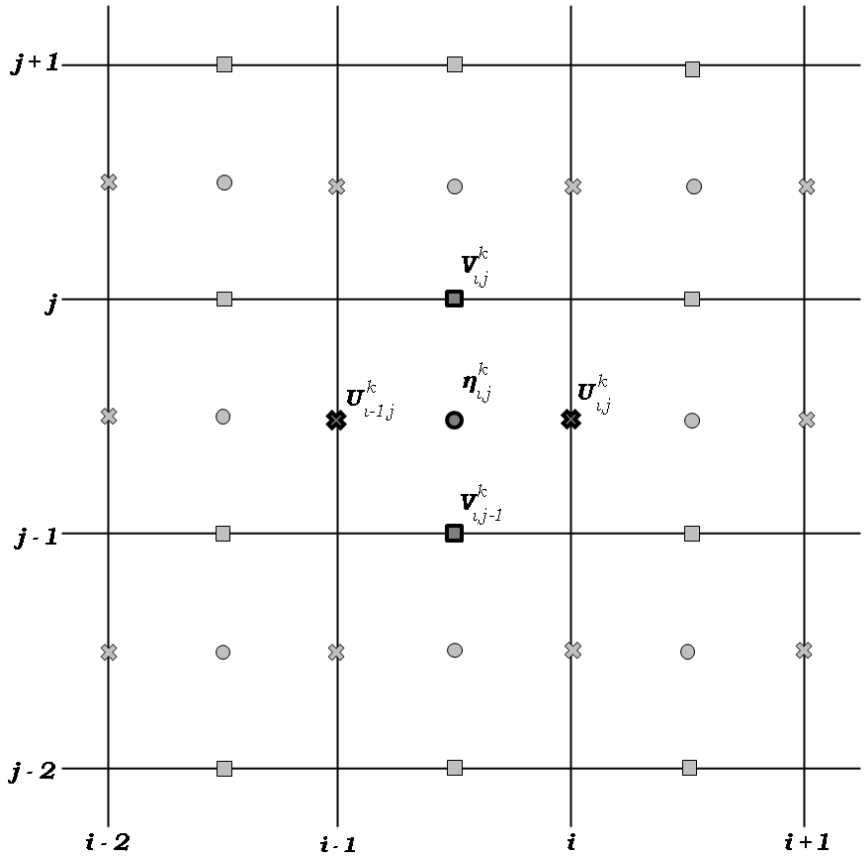

2.4.7 Momentum equations in finite difference form

The finite difference form of Equations (2.2) and (2.3) time level *k*, therefore, can be defined by approximating the time derivative using leap-frog method and combining the difference terms derived in Equations (2.19) to (2.25), as shown in Equations (2.26) and (2.27). The distribution of variables used in these equations to compute $\mathbf{U}_{i,j}^{k+1}$ and $\mathbf{V}_{i,j}^{k+1}$ is shown in Figures 2.5 and 2.6, respectively. Since the leap-frog technique is employed to march forward in time, we have applied a two level scheme at every 20 time step to remove the computational mode as suggested by Kowalik and Murty [1993].

$$\mathbf{U}_{i,j}^{k+1} = \mathbf{U}_{i,j}^{k-1} + 2\Delta t\Bigg[-\frac{1}{4\Delta x}\{(\boldsymbol{u}_{i+1,j}^{k} + \boldsymbol{u}_{i,j}^{k})(\boldsymbol{U}_{i+1,j}^{k} + \boldsymbol{U}_{i,j}^{k}) - (\boldsymbol{u}_{i,j}^{k} + \boldsymbol{u}_{i-1,j}^{k})(\boldsymbol{U}_{i,j}^{k} + \boldsymbol{U}_{i-1,j}^{k})\} - \frac{1}{4\Delta y}\{(\boldsymbol{v}_{i+1,j}^{k} + \boldsymbol{v}_{i,j}^{k})(\boldsymbol{U}_{i,j+1}^{k} + \boldsymbol{U}_{i,j}^{k}) - (\boldsymbol{v}_{i+1,j-1}^{k} + \boldsymbol{v}_{i,j-1}^{k})(\boldsymbol{U}_{i,j}^{k} + \boldsymbol{U}_{i,j-1}^{k})\} + \frac{f}{4}(\boldsymbol{V}_{i+1,j}^{k} + \boldsymbol{V}_{i+1,j-1}^{k} + \boldsymbol{V}_{i,j}^{k} + \boldsymbol{V}_{i,j-1}^{k}) - \frac{g}{2\Delta x}(\boldsymbol{h}_{i,j} + \boldsymbol{h}_{i+1,j} + \boldsymbol{\eta}_{i,j}^{k} + \boldsymbol{\eta}_{i+1,j}^{k})(\boldsymbol{\eta}_{i+1,j}^{k} - \boldsymbol{\eta}_{i,j}^{k}) + A_H\Big\{\frac{1}{(\Delta x)^2}(\mathbf{U}_{i+1,j}^{k-1} - 2\mathbf{U}_{i,j}^{k-1} + \mathbf{U}_{i-1,j}^{k-1}) + \frac{1}{(\Delta y)^2}(\mathbf{U}_{i,j+1}^{k-1} - 2\mathbf{U}_{i,j}^{k-1} + \mathbf{U}_{i,j-1}^{k-1})\Big\} + \frac{C_d\mathbf{U}_{i,j}^{k-1}\sqrt{(\mathbf{U}_{i,j}^{k-1} \times \mathbf{U}_{i,j}^{k-1}) + (\mathbf{V}_{i,j}^{k-1} \times \mathbf{V}_{i,j}^{k-1})}}{(\boldsymbol{h}_{i,j} + \boldsymbol{\eta}_{i,j}^{k-1})^2}\Bigg] \tag{2.26}$$

$$\mathbf{U}_{i,j}^{k+1} = \mathbf{U}_{i,j}^{k-1} + 2\Delta t\Bigg[-\frac{1}{4\Delta x}\{(\boldsymbol{u}_{i+1,j}^{k} + \boldsymbol{u}_{i,j}^{k})(\boldsymbol{U}_{i+1,j}^{k} + \boldsymbol{U}_{i,j}^{k}) - (\boldsymbol{u}_{i,j}^{k} + \boldsymbol{u}_{i-1,j}^{k})(\boldsymbol{U}_{i,j}^{k} + \boldsymbol{U}_{i-1,j}^{k})\} - \frac{1}{4\Delta y}\{(\boldsymbol{v}_{i+1,j}^{k} + \boldsymbol{v}_{i,j}^{k})(\boldsymbol{U}_{i,j+1}^{k} + \boldsymbol{U}_{i,j}^{k}) - (\boldsymbol{v}_{i+1,j-1}^{k} + \boldsymbol{v}_{i,j-1}^{k})(\boldsymbol{U}_{i,j}^{k} + \boldsymbol{U}_{i,j-1}^{k})\} + \frac{f}{4}(\boldsymbol{V}_{i+1,j}^{k} + \boldsymbol{V}_{i+1,j-1}^{k} + \boldsymbol{V}_{i,j}^{k} + \boldsymbol{V}_{i,j-1}^{k}) - \frac{g}{2\Delta x}(\boldsymbol{h}_{i,j} + \boldsymbol{h}_{i+1,j} + \boldsymbol{\eta}_{i,j}^{k} + \boldsymbol{\eta}_{i+1,j}^{k})(\boldsymbol{\eta}_{i+1,j}^{k} - \boldsymbol{\eta}_{i,j}^{k}) + A_H\Big\{\frac{1}{(\Delta x)^2}(\mathbf{U}_{i+1,j}^{k-1} - 2\mathbf{U}_{i,j}^{k-1} + \mathbf{U}_{i-1,j}^{k-1}) + \frac{1}{(\Delta y)^2}(\mathbf{U}_{i,j+1}^{k-1} - 2\mathbf{U}_{i,j}^{k-1} + \mathbf{U}_{i,j-1}^{k-1})\Big\} + \frac{C_d\mathbf{U}_{i,j}^{k-1}\sqrt{(\mathbf{U}_{i,j}^{k-1} \times \mathbf{U}_{i,j}^{k-1}) + (\mathbf{V}_{i,j}^{k-1} \times \mathbf{V}_{i,j}^{k-1})}}{(\boldsymbol{h}_{i,j} + \boldsymbol{\eta}_{i,j}^{k-1})^2}\Bigg] \tag{2.27}$$

Figure 2.5 Same as Figure 2.4, but showing the distribution of variable used in Equation (2.2) to compute $\mathbf{U_{i,j}^{k+1}}$.

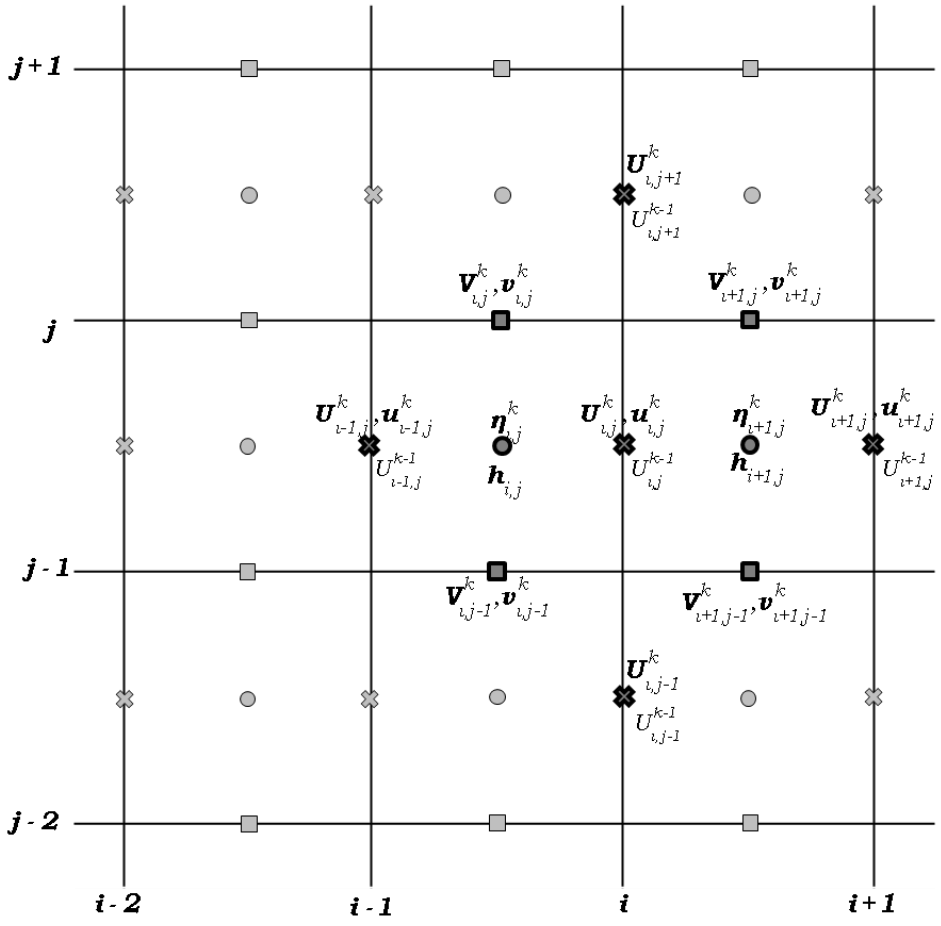

Figure 2.6 Same as Figure 2.4, but showing the distribution of variable used in Equation (**2.3**) to compute $\mathbf{V_{i,j}^{k+1}}$.

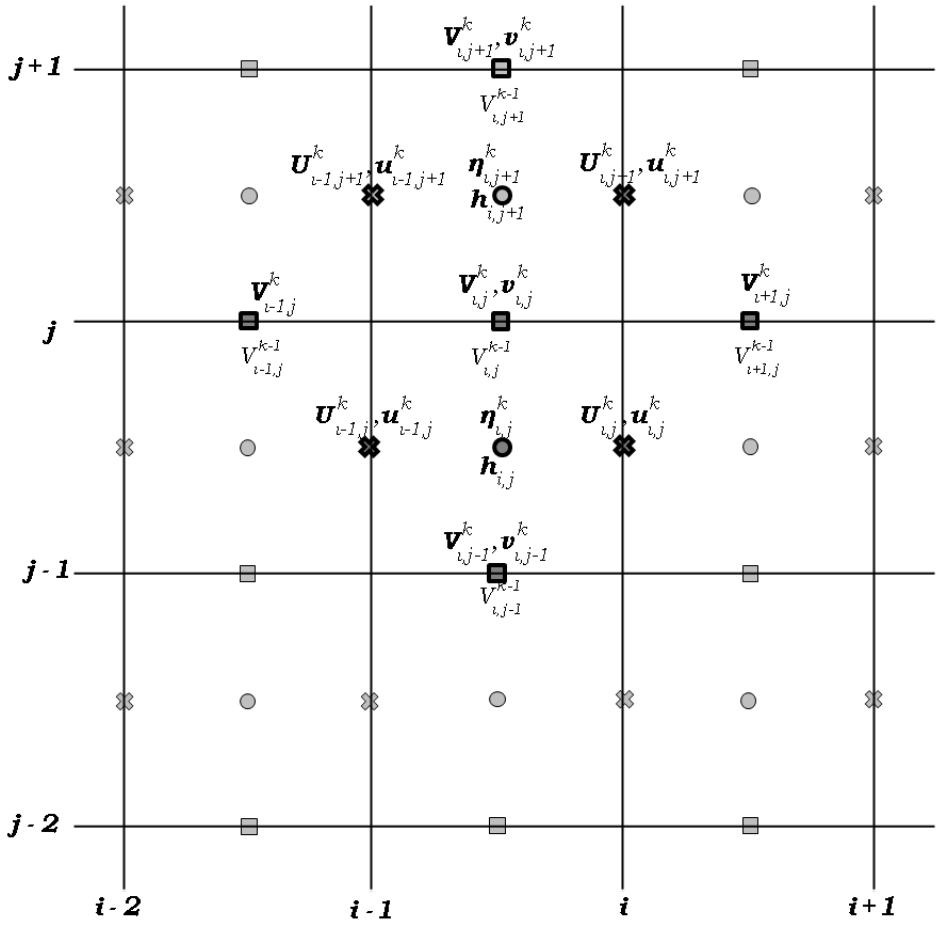

2.5 The initial and boundary conditions

It is essential to define the appropriate initial and boundary conditions for numerical solution of the equations.

2.5.1 Initial conditions

The initial conditions to be specified in the numerical model are defined as follows:

$$\eta(x, y, 0) = \eta_0(x, y),$$
$$U(x, y, 0) = U_0(x, y),$$
$$and \qquad V(x, y, 0) = V_0(x, y) \tag{2.28}$$

where η_0, U_0 and V_0 are the elevation and velocity fields at time $t = 0$. Since the actual values for initial elevations and velocities are not available, a 'cold start' is specified, which is a standard practise:

$$\eta(x, y, 0) = U(x, y, 0) = V(x, y, 0) = 0 \tag{2.29}$$

In order to remove any instability produced by this approximation, the numerical model is run for sufficient spin-up period so that any initial disturbance caused by this condition is assumed to disappear within this period.

2.5.2 Closed boundary conditions

The boundary between land and sea represents the closed boundaries in the tidal model.

Coastal boundary

The boundary between land and sea in the domain, i.e the physical coastline is approximated as impermeable walls parallel to either x-axis or y-axis as shown in Figure 2.7 representing a solid boundary with no flow across it. The thin curved line in Figure 2.7 shows the schematic physical coastline and thick straight lines define the approximated coastal boundary of the model. Along the coastal boundaries, zero normal flux and slip conditions were applied.

Figure 2.7 Schematic representation of actual coastal boundaries (thin solid line) into orthogonal vertical walls (thick solid line) representing the closed boundaries. The shaded area (grey) represents land and the dashed line represents the open boundaries. All boundaries are shown indicatively and out of scale for clarity.

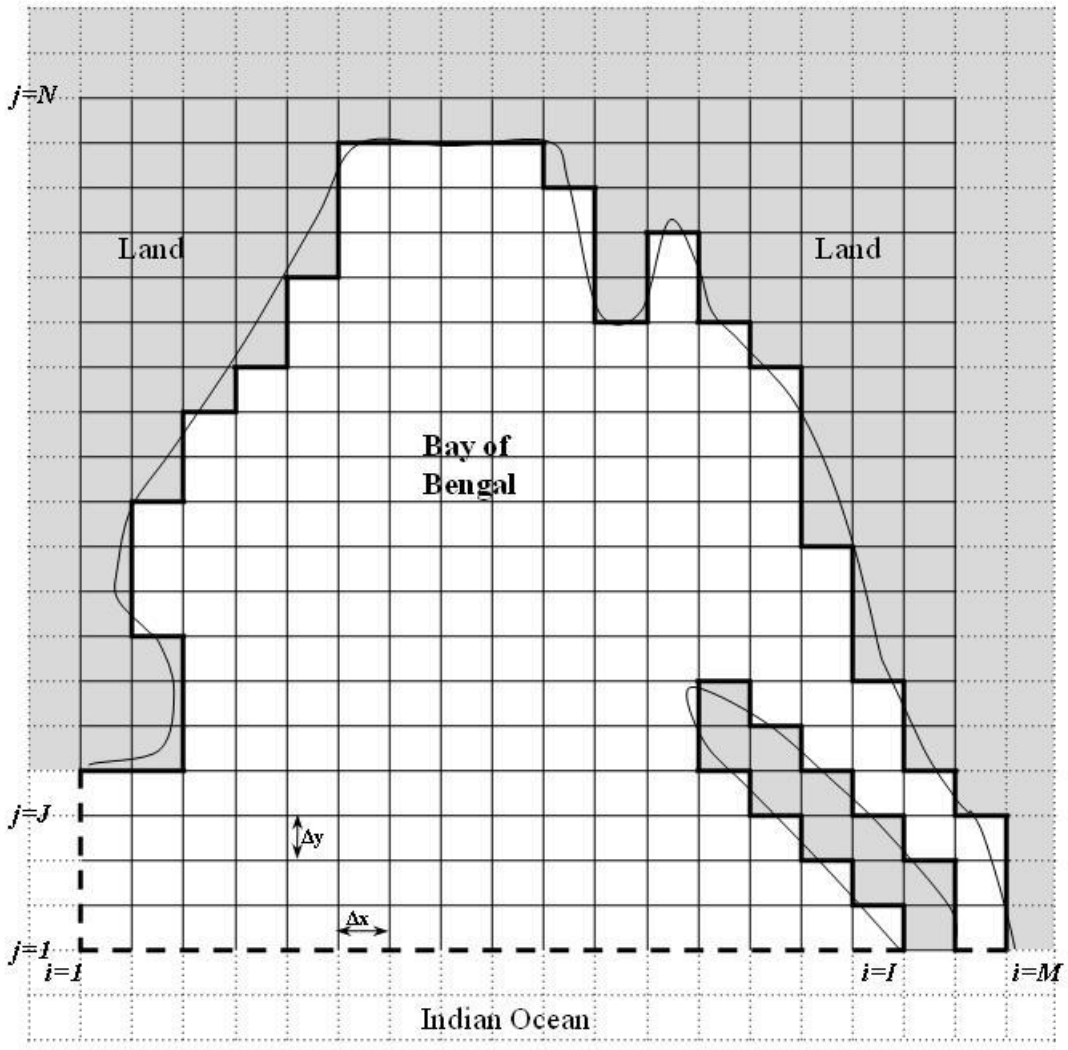

Surface boundary

The treatment of surface boundary plays an important role in storm surge model in which wind force is allowed to act on the sea surface and to move its surface tangentially through frictional forces. Since this chapter includes description of tidal model alone, the description of surface wind stresses $\tau_{sx}$and τ_{sy}, that will be included in momentum Equations (2.2) and (2.3) for the storm surge model, is presented in Chapter 5. As represented by Equations (2.2) and (2.3) if there is only tidal forcing (no wind),

$$\tau_{sx} = \tau_{sy} = 0 \tag{2.30}$$

Seabed

The sea bed is also a solid boundary which does not allow water to pass through. The closed boundary at seabed is also treated with a free slip condition, whereby the velocity at the sea bed is not set to zero but a value obtained from an appropriate quadratic friction law that relates frictional stress directly to the velocity at the bed. The bottom stress τ_b is defined as:

$$\tau_b = \rho C_D |u| u \tag{2.31}$$

where C_D is coefficient of bottom friction which usually lies between 1 x 10^{-3} and 3 x 10^{-3}.

2.5.3 Open boundary conditions

Open boundaries are not real physical boundaries but represent the artificial edge of the model domain that meet the open ocean. The driving force of tidal as well as storm surge model is provided at the open boundary, mainly in the form of tidal elevation. Since the storm surge model includes additional driving force in the form of wind applied at the surface, the open boundary conditions formulated for the tidal model and storm surge model are different.

The model domain consists of three open boundaries – one is on the western side and two are on the southern side, which are schematically shown as dashed lines in Figure 2.7. A height specified boundary condition is applied to the

tidal model, in which the tidal elevation $\eta_{i,j}$ is specified for all time at each η point of the grid element (i,j) along the open boundaries, where $i = 1, \mathrm{I}; j = 1$ for the southern boundaries and $i = 1; j = 1, \mathrm{J}$ for the western boundary. The values of *I* and *J* are selected such that the grid elements (I+1, 1) and (1, J+1) represent land. Since the open boundary connects the model domain to the open ocean, as shown in Figure 2.7, the tidal elevation at each grid element along the open boundary is obtained from Global Tidal Model. The tidal elevation ($\eta_{i,j}$), is then used to compute the velocity components at each grid element along the boundary using Equations (2.2) and (2.3). However, due to lack of some computational values, the numerical formulation of these equations along the open boundaries is different from the Equations (2.26) and (2.27).

In order to compute the velocity components along the southern open boundary, the finite difference Equations (2.26) and (2.27) are simplified by neglecting the terms that include undefined variables like $U_{i,j-1}$. The equations formulated for the grid elements at the two ends of the southern boundaries - *(1,1)* and *(I,1)* and at any grid element *(i,1)* are different due to the difference in the arrangement of the surrounding grids. The simplified finite difference form of Equations (2.2) and (2.3) for the three scenarios are presented below:

Grid element (*1, 1*)

$$\boldsymbol{U}_{i,j}^{k+1} = \boldsymbol{U}_{i,j}^{k-1} + 2\Delta t\left[+\frac{f}{2}\left(\boldsymbol{V}_{i+1,j}^{k} + \boldsymbol{V}_{i,j}^{k}\right) - \frac{g}{2\Delta x}\left(\boldsymbol{h}_{i,j} + \boldsymbol{h}_{i+1,j} + \boldsymbol{\eta}_{i,j}^{k} + \boldsymbol{\eta}_{i+1,j}^{k}\right)\left(\boldsymbol{\eta}_{i+1,j}^{k} - \boldsymbol{\eta}_{i,j}^{k}\right) + \frac{C_d \mathbf{U}_{i,j}^{k-1}\sqrt{\left(\mathbf{U}_{i,j}^{k-1} \times \mathbf{U}_{i,j}^{k-1}\right) + \left(\mathbf{V}_{i,j}^{k-1} \times \mathbf{V}_{i,j}^{k-1}\right)}}{\left(\boldsymbol{h}_{i,j} + \boldsymbol{\eta}_{i,j}^{k-1}\right)^2}\right] \quad (2.32)$$

$$\boldsymbol{V}_{i,j}^{k+1} = \boldsymbol{V}_{i,j}^{k-1} + 2\Delta t \left[\frac{f}{3}\left(\boldsymbol{U}_{i,j+1}^{k} + \boldsymbol{U}_{i-1,j+1}^{k} + \boldsymbol{U}_{i,j}^{k}\right) - \frac{g}{2\Delta y}\left(\boldsymbol{h}_{i,j} + \boldsymbol{h}_{i,j+1} + \boldsymbol{\eta}_{i,j}^{k} + \boldsymbol{\eta}_{i,j+1}^{k}\right)\left(\boldsymbol{\eta}_{i,j+1}^{k} - \boldsymbol{\eta}_{i,j}^{k}\right) + \frac{C_d \mathbf{V}_{i,j}^{k-1}\sqrt{\left(\mathbf{U}_{i,j}^{k-1} \times \mathbf{U}_{i,j}^{k-1}\right) + \left(\mathbf{V}_{i,j}^{k-1} \times \mathbf{V}_{i,j}^{k-1}\right)}}{\left(\boldsymbol{h}_{i,j} + \boldsymbol{\eta}_{i,j}^{k-1}\right)^2} \right] \tag{2.33}$$

Grid element (I, 1)

$$\boldsymbol{U}_{i,j}^{k+1} = 0.0 \tag{2.34}$$

$$\boldsymbol{V}_{i,j}^{k+1} = \boldsymbol{V}_{i,j}^{k-1} + 2\Delta t \left[+ \frac{f}{2}\left(\boldsymbol{U}_{i-1,j+1}^{k} + \boldsymbol{U}_{i-1,j}^{k}\right) - \frac{g}{2\Delta y}\left(\boldsymbol{h}_{i,j} + \boldsymbol{h}_{i,j+1} + \boldsymbol{\eta}_{i,j}^{k} + \boldsymbol{\eta}_{i,j+1}^{k}\right)\left(\boldsymbol{\eta}_{i,j+1}^{k} - \boldsymbol{\eta}_{i,j}^{k}\right) + \frac{C_d \mathbf{V}_{i,j}^{k-1}\sqrt{\left(\mathbf{U}_{i,j}^{k-1} \times \mathbf{U}_{i,j}^{k-1}\right) + \left(\mathbf{V}_{i,j}^{k-1} \times \mathbf{V}_{i,j}^{k-1}\right)}}{\left(\boldsymbol{h}_{i,j} + \boldsymbol{\eta}_{i,j}^{k-1}\right)^2} \right] \tag{2.35}$$

Grid element (*i, 1*)

$$\boldsymbol{U}_{i,j}^{k+1} = \boldsymbol{U}_{i,j}^{k-1} + 2\Delta t \left[\frac{f}{2}\left(\boldsymbol{V}_{i+1,j}^{k} + \boldsymbol{V}_{i,j}^{k}\right) - \frac{g}{2\Delta x}\left(\boldsymbol{h}_{i,j} + \boldsymbol{h}_{i+1,j} + \boldsymbol{\eta}_{i,j}^{k} + \boldsymbol{\eta}_{i+1,j}^{k}\right)\left(\boldsymbol{\eta}_{i+1,j}^{k} - \boldsymbol{\eta}_{i,j}^{k}\right) + A_H \left\{ \frac{1}{(\Delta x)^2}\left(\mathbf{U}_{i+1,j}^{k-1} - 2\mathbf{U}_{i,j}^{k-1} + \mathbf{U}_{i-1,j}^{k-1}\right) + \frac{1}{(\Delta y)^2}\left(\mathbf{U}_{i,j+2}^{k-1} - 2\mathbf{U}_{i,j+1}^{k-1} + \mathbf{U}_{i,j}^{k-1}\right) \right\} + \frac{C_d \mathbf{U}_{i,j}^{k-1}\sqrt{\left(\mathbf{U}_{i,j}^{k-1} \times \mathbf{U}_{i,j}^{k-1}\right) + \left(\mathbf{V}_{i,j}^{k-1} \times \mathbf{V}_{i,j}^{k-1}\right)}}{\left(\boldsymbol{h}_{i,j} + \boldsymbol{\eta}_{i,j}^{k-1}\right)^2} \right] \tag{2.36}$$

$$\boldsymbol{V}_{i,j}^{k+1} = \boldsymbol{V}_{i,j}^{k-1} + 2\Delta t\left[\frac{f}{4}\left(\boldsymbol{U}_{i,j+1}^{k} + \boldsymbol{U}_{i-1,j+1}^{k} + \boldsymbol{U}_{i,j}^{k} + \boldsymbol{U}_{i-1,j}^{k}\right)\right.$$
$$- \frac{g}{2\Delta y}\left(\boldsymbol{h}_{i,j} + \boldsymbol{h}_{i,j+1} + \boldsymbol{\eta}_{i,j}^{k} + \boldsymbol{\eta}_{i,j+1}^{k}\right)\left(\boldsymbol{\eta}_{i,j+1}^{k} - \boldsymbol{\eta}_{i,j}^{k}\right)$$
$$+ A_H\left\{\frac{1}{(\Delta x)^2}\left(\mathbf{V}_{i+1,j}^{k-1} - 2\mathbf{V}_{i,j}^{k-1} + \mathbf{V}_{i-1,j}^{k-1}\right) + \frac{1}{(\Delta y)^2}\left(\mathbf{V}_{i,j+2}^{k-1} - 2\mathbf{V}_{i,j+1}^{k-1} + \mathbf{V}_{i,j}^{k-1}\right)\right\}$$
$$\left. + \frac{C_d \mathbf{V}_{i,j}^{k-1}\sqrt{\left(\mathbf{U}_{i,j}^{k-1} \times \mathbf{U}_{i,j}^{k-1}\right) + \left(\mathbf{V}_{i,j}^{k-1} \times \mathbf{V}_{i,j}^{k-1}\right)}}{\left(\boldsymbol{h}_{i,j} + \boldsymbol{\eta}_{i,j}^{k-1}\right)^2}\right] \quad (2.37)$$

Similar equations are derived and applied for the western open boundary by neglecting terms that include un-defined variables such as $V_{i-1,j}$.

In the tidal model, a height specified boundary condition can be used as there are no internal flows produced by any wind forcing. However, in the storm surge model, which is driven by a combination of two forces: wind force applied at the surface and tidal elevation specified at the open boundary, a radiation type boundary condition is applied at the open boundaries. This will allow outward passage of the any internal waves generated within the model domain by wind action. The radiation type boundary condition is presented in Chapter 5.

2.6 Summary

The numerical techniques used to solve the vertically integrated hydrodynamic equations that govern the tidal model, are illustrated. The spatial and temporal discretization of the governing equations to represent them in finite difference form is investigated in detail and summarized in the chapter. The understanding of these techniques and formulations is essential to comprehend the basics of the tide and storm surge model, the application of which will be described in the following chapters. The most significant input data required for the numerical model is bathymetry. The generation of an accurate bathymetric dataset for the Bay of Bengal region is discussed in next chapter.

Chapter 3

Generation of bathymetric datasets for numerical model

3.1 Introduction

It is well known that the performance of a numerical model depends on accurate representation of sea bed levels. A variety of bathymetric datasets with different coverage, resolutions, and accuracies are currently available. Among these is the ETOPO5 [National Geophysical Data Centre (NGDC), 1988] bathymetric grids which are widely used.

ETOPO5 is a 5-arc minute bathymetry grid produced by combining the ocean depth values obtained from DBDB-5 [US National Geospatial-Intelligence Agency, 1994] with the land elevation data obtained from different sources. The DBDB-5 (Digital Bathymetric Data Base 5) dataset was generated by digitizing the depth contours above 200 m from hydrographic charts of nominally 1:4,000,000 scale. The digitized values were gridded to a 5 arc minute grid using a multi-stage minimum-curvature spline interpolation algorithm. Digitization was carried out only for depths greater than 200 m as DBDB-5 was designed to be used only as a deep-water data base [Goodwillie, 2003]. Subsequently, the ETOPO5 dataset is not accurate in regions where the depth values are less than 200 m.

The region of interest, in the present study, is the Bay of Bengal. The head bay, the Gulf of Martaban and Malacca Strait which form parts of the present study region, are characterised by very shallow depths, wide continental shelf and sudden changes in depth contours. These characteristics are not represented in a global dataset such as ETOPO5. We noted that there are no open source accurate shallow water bathymetric dataset available for the Bay of Bengal. Therefore, we

decided to generate bathymetric dataset for the shallow regions of Bay of Bengal. However, while undertaking the task, we observed that the shallow-water usage of bathymetric datasets for the entire Indian Ocean are often not as coordinated internationally and not as standardized as deep-water datasets leading to the use of different sources of bathymetric data by different ocean modellers. For example, Unnikrishnan et al. [1999], for their tidal model, digitized the hydrographic charts of the region to get a more accurate bathymetry to obtain improved model results. In order to avoid such inconsistencies in model results due to the use of bathymetric data from different sources, a common dataset for shallow waters in the entire Indian Ocean is very essential. This need has become urgent after the disastrous tsunami of 26 December 2004 that occurred in the Indian Ocean. Tsunami simulations are critically dependent on the bathymetry used, as are the source-region estimates based on backward ray tracing [Lay et al., 2005a, b; Neetu et al., 2005].

The task to generate reliable bathymetry on the continental shelves of the Bay of Bengal was, therefore, extended to cover the shallow regions of the Indian Ocean north of 38°S. To achieve this, we digitized the hydrographic charts listed in Table 3.1 (published by the National Hydrographic Office (NHO), Dehradun, India - formerly known as the Naval Hydrographic Office till 1998) for depths less than 200 m. Since ETOPO5 dataset is reliable in deep waters, the newly generated shelf bathymetry was blended with the deep water ETOPO5 bathymetry to develop a full bathymetric dataset. The generation and reliability of the modified bathymetric datasets has been documented in detail in Sindhu et al. [2007].

The methodology adopted to generate the shallow water bathymetry is elaborated in Section 3.2 and the improvements of the modified datasets over the original ETOPO5 dataset is demonstrated in Section 3.3. The modified ETOPO5 is foreseen to serve the ocean modellers as common datasets for the shallow regions in the Indian Ocean.

Table 3.1 List of hydrographic charts used for digitization, their natural scale, and year of publication for different regions in the Indian Ocean.

	Charts	**Scale**	**Year**
1	Walvis Bay to Lorenco Marques	1:3,500,000	1975
2	Lorenco Marques to Mogadiscio	1:3,500,000	1971
3	Indian Ocean: Western portion	1:10,000,000	1979
4	Gulf of Aden: Eastern portion including Socatra Island	1:750,000	1982
5	Gulf of Aden and Southern part of Red Sea	1:750,000	1978
6	Red Sea	1:2,250,000	1973
7	Arabian Sea	1:3,500,000	1974
8	Strait of Hormuz to Qatar	1:750,000	1982
9	Qatar to Shatt Al Arab	1:750,000	1982
10	Muscat to Mumbai (Bombay)	1:1,500,000	1980
11	Gwadar to Dwarka	1:750,000	1979
12	Mumbai (Bombay) to Cape Comorin	1:1,500,000	1980
13	Cochin to Vishakhapatnam	1:1,500,000	1974
14	Bay of Bengal: Northern Side (Krishnapatnam to Bassein river)	1:1,500,000	1976
15	Andaman Sea	1:1,500,000	1979
16	Maldive Islands to Sumatra	1:3,500,000	1973
17	South China Sea	1:3,500,000	1976
18	Cora Divh to Elikalpeni bank	1:500,000	1983
19	Central Lakshwadeep	1:300,000	1983
20	Ihavandiffulu atoll to Horsburgh atoll	1:300,000	1981
21	Horsburgh atoll to Haddummati atoll	1:300,000	1982
22	Haddummati atoll to Addu atoll	1:300,000	1981
23	Chagos Archipelago	1:375,000	1984
24	Chagos Archipelago to Malagasy	1:3,500,000	1974

3.2 Data and methodology

3.2.1 Generation of improved bathymetric grids

The extent of each of the hydrographic charts, used for digitization is shown in Figure 3.1. The nautical charts and the allied nautical publications produced by NHO have built the reputation of the organisation all over the world for their accuracies [Ahuja, 2000]. The database used in the preparation of these charts have been obtained from different sources of information like hydrographic survey, local survey, ocean soundings, earlier editions of nautical charts, coastal survey and tidal data [Vatsa et al., 2002]. Thus, the accuracy and the adequacy of the hydrographic charts depend on the quality of the data collected during the survey [Vatsa et al., 2002]. The International Hydrographic Organization (IHO) has defined minimum standards for hydrographic surveys such as positional accuracy, sounding accuracy, sounding density in its special publication 44 (S-44). These standards are to be applied to the hydrographic charts all over the world [Van Der Wal and Pye, 2003]. The first edition of S-44 was in 1968 with its subsequent editions in 1982 and 1987. These three editions were similar as they were meant for the surveys carried out for the preparations of nautical charts which were generally used for marine navigation [Mills, 1998]. These standards require that at least 95% of the positions for the soundings in the shallow water should lie within 1.5 mm of the true positions, at the scale of the survey [Van Der Wal and Pye, 2003], i.e., for a 1:10,000 scale of survey, soundings were to be located within 15 m of their true position with a confidence of 95% probability. According to the third edition of S-44 [IHO,1987], at least 90% of the total errors in measuring depths should not exceed 30 cm for depths less than 30 m or 1% of depths for depths greater than 30 m [Mills, 1998]. Also, the distance between each sounding line should not be more than 1 cm at the scale of survey and sounding interval should not exceed 4 to 6 mm at the survey scale. NHO follows these standards and publishes the charts and other publications in total compliance with the specifications of IHO. NHO also maintains constant interaction with other

NHO and the IHO in order to ensure strict standards in products and services (http://indiannavy.nic.in/methodology.htm).

The hydrographic charts used for digitization were published during 1971-1982. Prior to the installation of automated cartographic system in NHO during 1981 [Vatsa and Kumar, 2002], the conventional hand drawn method was used to draw the contours from the lines of soundings obtained using the echo sounder trace, the soundings log and the track chart.

Digitization of the charts

Digitization of the maps was carried out using the GRASS (Geographic Resources Analysis Support System) GIS (Geographic Information System) [GRASS Development Team, 2005] software. It is an open-source, free software, readily available on the web at http://grass.itc.it. While importing the non-georeferenced scanned maps into GRASS, they were assigned X-Y projection and the grid resolution was defined to be 1 pixel. The unreferenced map was then geo-coded by defining nine ground control points (GCPs). The accuracy of the GCPs could be checked as the software has in-built function to calculate the root mean square (RMS) error after setting at least three reference points. The RMS error is acceptable if it is less than half of the grid resolution [Neteler and Mitasova, 2002] (i.e. RMS should be less than 0.5). There is also an option to deactivate a control point if it is highly deviated from the other points. The software also allows quality control in which the geo-coded points can be checked against the actual points in the scanned maps. Thus the geo-coding was done with strict care and the RMS error obtained was less than 0.2. The results so obtained were highly accurate.

The contours digitized from the small scale charts (1:2,250,000 - 10,000,000) were 30 m and 200 m and those from the large scale charts (1:300,000 - 1,500,000) were 5, 10, 20, 30, 50, 100, 200 m. The digitization was carried out at very close intervals to capture the trends in the contours and to obtain sufficiently dense data so that the interpolation could be carried out accurately. All the sounding depths less than 200 m were also digitized.

Figure 3.1 The boxes in the map show the regions for which the hydrographic charts were digitized. The number in each box corresponds to the number given in Table 3.1. The digitized values are also plotted.

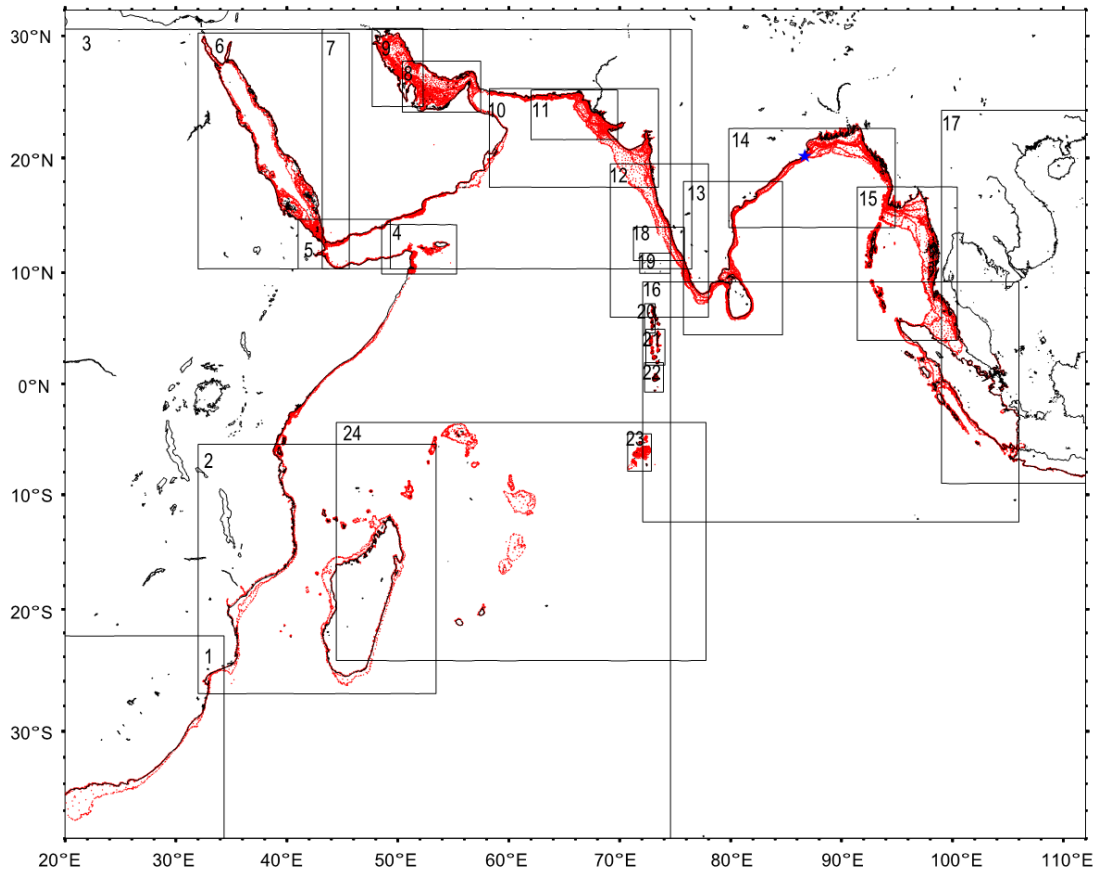

Gridding the digitized data

The digitized data thus obtained was averaged using a simple box averaging process called the blockmean available in the GMT (Generic Mapping Tools) [Wessel and Smith, 1998] package. The box size defined for averaging should be equal to target grid size. This averaged data was then gridded for every 5 arc minutes latitude-longitude grid using the surface program [Wessel and Smith, 1995] in the GMT package. The surface is a generalization of the minimum curvature algorithm. As mentioned earlier, DBDB5 (the major source of data for ETOPO5 dataset) is gridded using the minimum curvature spline algorithm, which is of the high-order class, and can cause undesired oscillations and false local maxima or minima [Smith and Wessel, 1990]. The "surface" program not only suppresses these effects but also prevents extrapolation by allowing the addition of a tension factor and bound constraints. The tension factor is chosen in such a way that the difference between the gridded data and the nearest digitized value is minimum in the least square sense and is fixed at 0.8. In the present work, the closed polygons with 200 m contour formed the bound constraints. We masked the values outside the polygons, so that the surface program did not produce any extrapolation. The values extrapolated on land were also masked using the options available in the GMT package.

Blending the original and the gridded dataset

We combined the gridded data derived with the same resolution as that of ETOPO5 with the original ETOPO5 dataset (masked for the land elevations and depths shallower than 200 m) to produce a better quality bathymetric dataset. But, the dataset obtained by simply merging the ETOPO5 with the digitized dataset showed some unrealistic features near the 200 m contour (Figure 3.2). Hence it was necessary to ensure a smooth transition between the two datasets. We experimented with a number of techniques to blend these two datasets, but none of them performed well, including the optimal interpolation method (Figure 3.2). The optimal interpolation method works best for a smoothly varying field and is dependent on the first-guess field. Since the bathymetric data have sharp gradients,

Figure 3.2 A section of the ocean bottom topography off Paradip (20.167°N) showing comparison between different blending techniques used: simple box averaging (red) and optimal interpolation (green). Also plotted is the original ETOPO5 (blue) and modified dataset before applying smoothing (black).

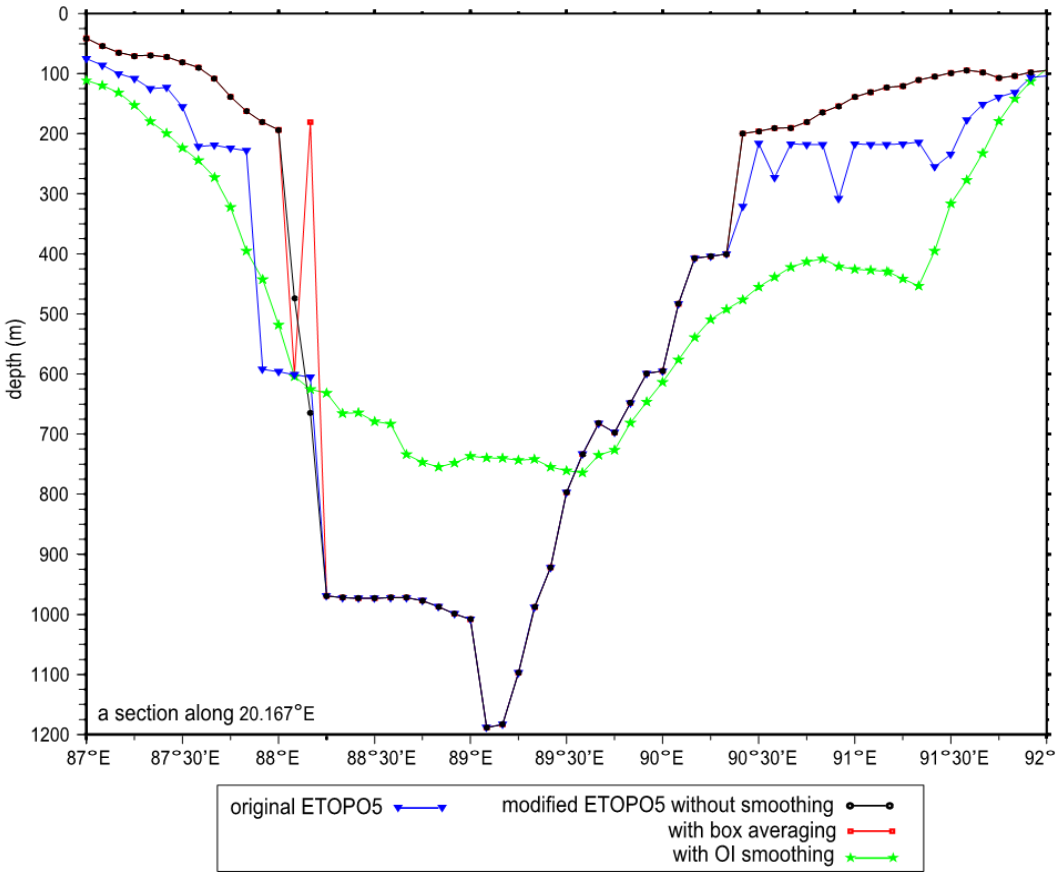

especially near the continental rise where the 200 m contour generally falls, optimal interpolation was found to be inappropriate in this case. Hence, we applied a simple box averaging process to blend these datasets. In this method, the grid points that showed spurious spikes (due to merging the datasets) were picked up and then the depth value at each of these points were replaced by the average of the depth values over a box of size 10 minutes around it. The average was computed only over the ocean points and did include the land points in the box. This method chopped off the unrealistic spikes in the dataset and kept the depths at other grid points unchanged (Figure 3.2). Thus a "modified ETOPO5" bathymetry was obtained, which is same as the original ETOPO5 in the deep ocean (greater than 200 m) but with more accurate depths derived from hydrographic charts for shallow waters (less than 200 m).

Though the region covered by the modified ETOPO5 dataset extended up to 112˚E, the major concern was the improvements only in the Indian Ocean region and hence, we masked the South China Sea region in the modified datasets. Thus, the modified dataset was obtained only for the Indian Ocean region.

3.2.2 Models used

Though the present thesis deals with simulations in the Bay of Bengal, we tested the improvements in the modified bathymetry by simulating the tides in the Gulf of Khambhat along the west coast of India (region indicated by dashed box in Figure 3.3) using the model developed by Unnikrishnan et al. [1999].

The model was run on 5 arc minutes spatial resolution for the same domain using the original ETOPO5 and the modified ETOPO5 bathymetric grids separately without changing any other model parameters. The accuracy of these bathymetric grids was evaluated by comparing the model results (sea surface elevation and vertically averaged current) with the tide-gauge recorded sea surface elevations at Veraval and Mumbai (Apollo Bandar) and current meter measurements in the Bombay High (19˚24.5′ N and 71˚2.5′E) region during 24 December 1981 – 03 January 1982, which were used by Unnikrishnan et al. [1999]. The vertically averaged cross-shore (u) and alongshore (v) components of

the currents were computed from the current meter measurements available at four depths (30, 45, 60 and 75 m). These vertically averaged components included the currents generated by other processes such as winds etc., in addition to tide driven currents, whereas the currents simulated using the tidal model were driven only by tides. Thus, in order to compare the observed currents with the simulated currents, the tidal currents were to be separated from the measured currents. Hence a high pass filter with cut off at 0.75 $day^{-1}$was applied to the vertically averaged current in order to remove the low frequency currents.

3.3 Results and Discussions

3.3.1 Improvements in the modified bathymetry

There is a significant improvement in the bathymetry in many shallow regions of Indian Ocean as seen from Figure 3.3 which shows the anomaly between the modified and original ETOPO5 bathymetric datasets. The anomaly was calculated by subtracting the original data from the modified data. The lower contour levels in the original ETOPO5 results in a positive anomaly of nearly 40-60 m in the gulfs such as Gulf of Khambhat and Gulf of Martaban. High negative anomalies of about 60-80 m are found along the west coast of India and around the Madagascar Island. The ETOPO5 dataset also have a problem in representing the bathymetry near the islands and atolls as these regions show large positive anomaly in depth.

We analyzed the improvements in detail in the Bay of Bengal region which forms the domain of the numerical model used in the present study to simulate tides and storm surges. The comparison between the two datasets in other areas, such as the Red Sea, Persian Gulf, and west coast of India are illustrated in Sindhu et al. [2007]. Figures 3.4 to 3.7 show the improvements in the modified ETOPO5 dataset for the head bay, Gulf of Martaban, Malacca Strait and the Andaman islands, the regions being indicated by the boxes in Figure 3.3.

Figure 3.3 The difference in depths (anomaly) between the modified ETOPO5 (ETOPO5 merged with the gridded digitized data) and the original ETOPO5 dataset for the Indian Ocean. The boxes mark the region shown in detail in Figures 3.4 to 3.7.

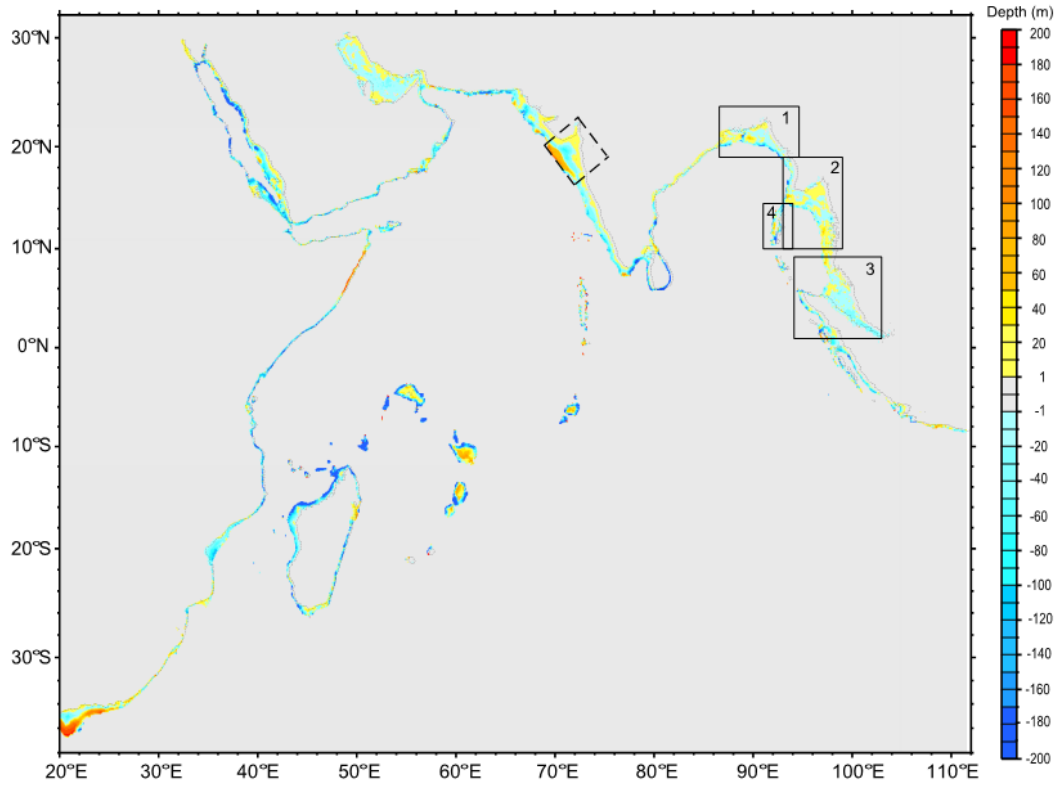

In the head bay, the original ETOPO5 dataset shows a shallow region of 40m around 90°E, 20.7°N (Figure 3.4a), thereby suggesting a sea mount like feature in the region. However, as evident from the hydrogrophic charts, no such feature is present in this region. The modified ETOPO5 thus yields a more realistic bathymetry for the head bay (Figure 3.4b) than the original ETOPO5 dataset. The modified bathymetry is similar to that obtained by Jakobsen et al. [2002], who derived the bathymetry for the head bay from British Admiralty Charts and BIWTA Depth Charts.

The modified ETOPO5 data set also represents the bathymetry of the Gulf of Martaban (Figure 3.5a) more accurately than the original ETOPO5 dataset (Figure 3.5b) and is similar to the bathymetry obtained by Ramaswamy et al. [2004] from a cruise of Ocean Research Vessel (ORV) Sagar Kanya.

In the Malacca Strait, the modified ETOPO5 (Figure 3.6b) dataset shows shallower depths than the original dataset in south eastern end (Figure 3.6a). This is found to be consistent with hydrographic charts of the region.

The original ETOPO5 dataset shows wide shallow regions of nearly 20 m depth around the Andaman islands (Figure 3.7a), whereas the modified dataset shows depth variations up to about 60 m in this region (Figure 3.7b). The depth of the sea in the region between the Andaman and the Little Andaman Islands is greater than 200 m in the original ETOPO5 (Figure 3.7a), but in the modified bathymetry, the depths in these regions do not exceed 50 m (Figure 3.7b). This results in a negative anomaly of greater than 200 m as shown in Figure 3.7c.

3.3.2 Evaluation of the modified bathymetric datasets

We demonstrate the improvements in the modified datasets by carrying out numerical experiments with the models mentioned in Section 3.2.2 using the original and the modified ETOPO5 dataset. As mentioned earlier, the domain of this tidal model covered the Gulf of Khambhat region, in which a sea-mount like feature is observed in the original ETOPO5 dataset indicated by the positive anomaly of 40-60 m in Figure 3.3.

Figure 3.4 The bathymetry obtained from the a) original ETOPO5, b) modified ETOPO5 and c) difference between them (anomaly) for the head bay.

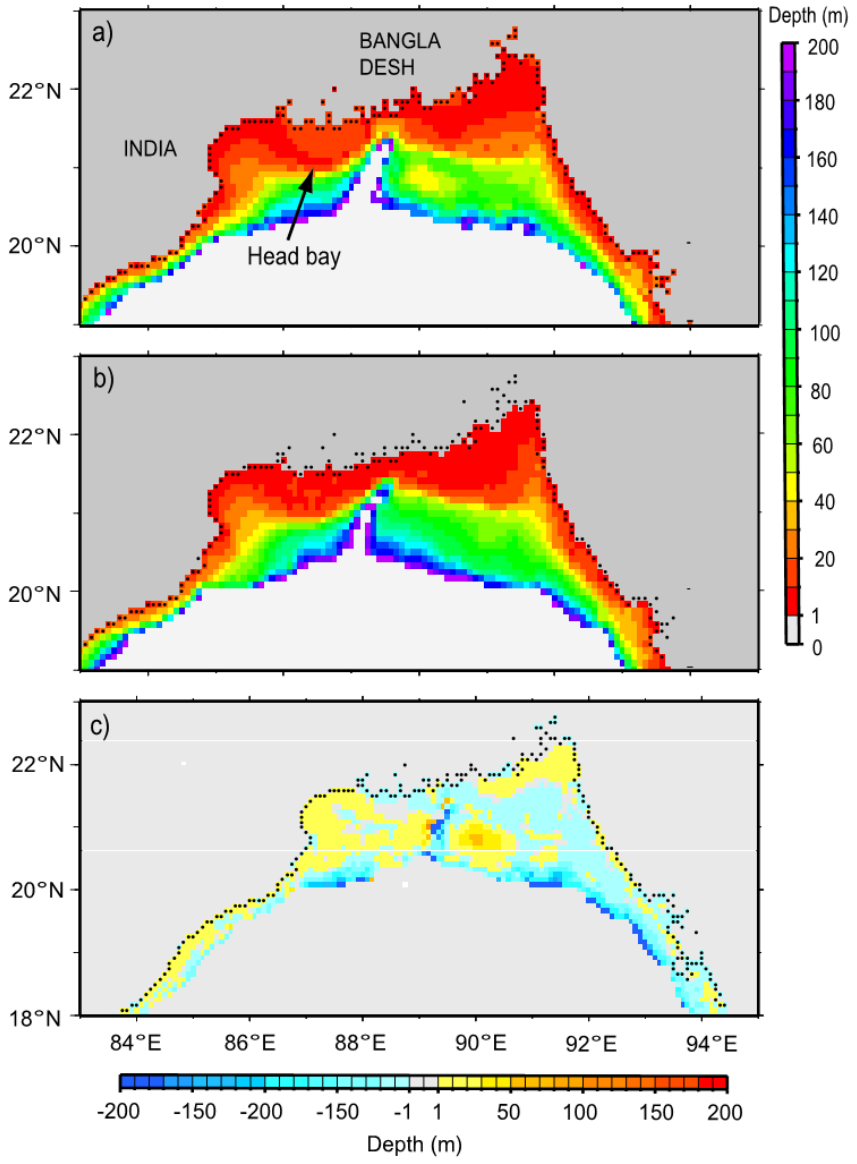

Figure 3.5 Same as Figure 3.4, but for the Gulf of Martaban.

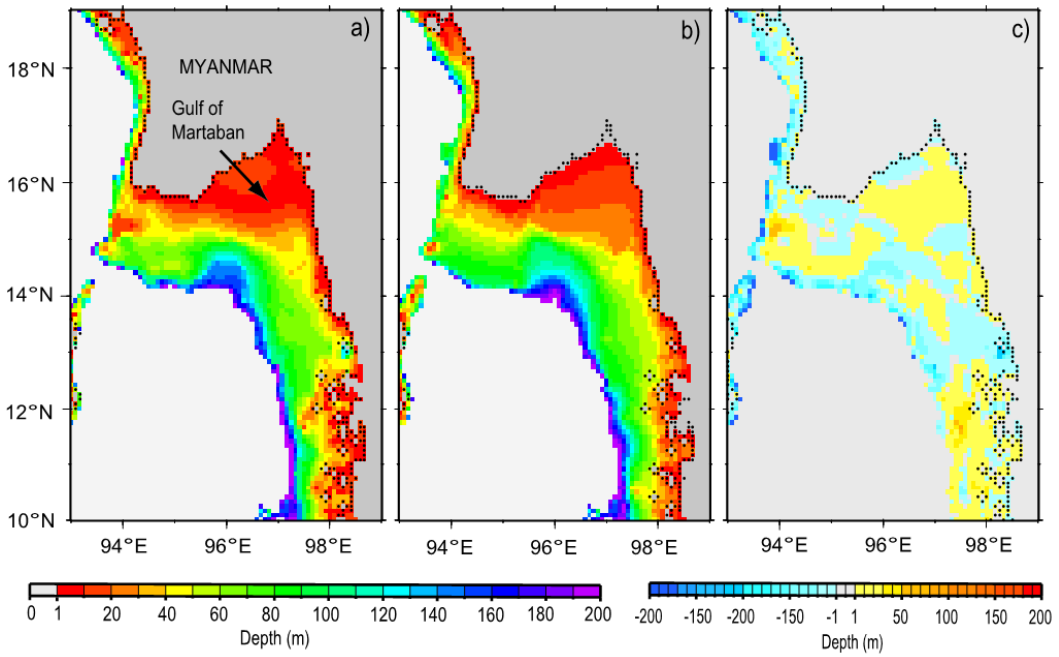

Figure 3.6 Same as Figure 3.4, but for the Malacca Strait.

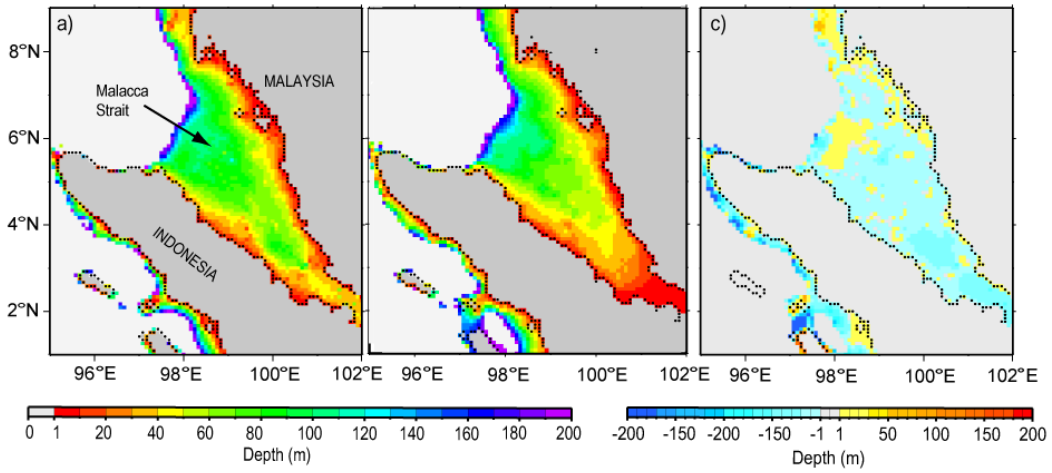

Figure 3.7 Same as Figure 3.4, but for the Andaman Islands.

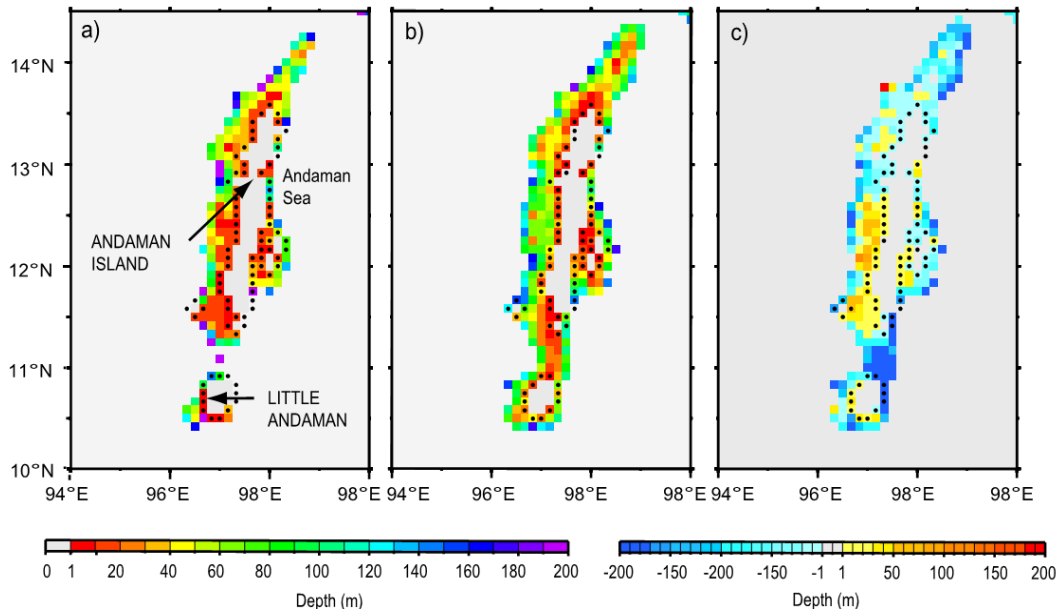

Tidal model

Figure 3.8 provides a comparison of the simulated sea surface elevations with the observations. At Mumbai, the comparison shows a poor agreement both in amplitude and phase when the original ETOPO5 bathymetry is used, but shows a good agreement in the case of modified ETOPO5 (Figure 3.8a). At Veraval, we can see only a slight improvement in the results when the modified ETOPO5 dataset is used (Figure 3.8b). The sea-mount-like feature in the original ETOPO5 has significantly affected the simulated sea surface elevations at Mumbai.

The comparison of the vertically averaged u and v components observed at Mumbai High with that obtained from the tidal model simulation (Figure 3.9a and b) clearly shows the improvement in the modified ETOPO5 bathymetric grid. The simulated u and v components obtained using the modified ETOPO5 are much closer to the observations than those obtained with the original ETOPO5.

From the discussions above, it is evident that the modified ETOPO5 dataset is an improvement over the original ETOPO5 dataset.

Figure 3.8 The sea surface elevation observed (red dots) at a) Mumbai (Apollo Bandar) and b) Veraval and that obtained from the simulation of the tidal model when original ETOPO5 dataset (blue line) and the modified dataset (black line) are used.

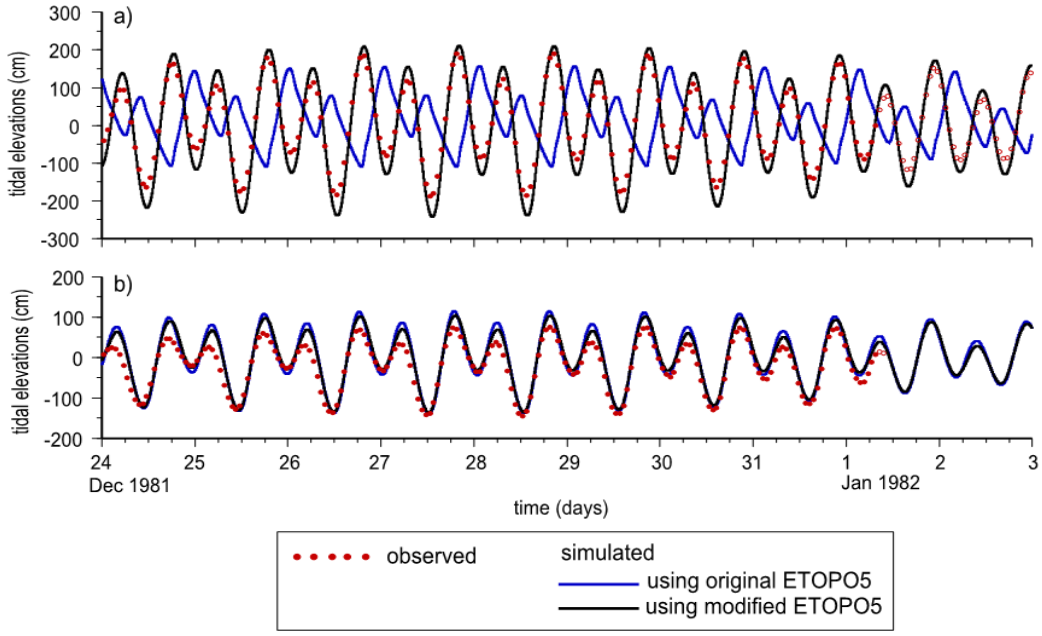

Figure 3.9 The vertically averaged a) cross-shore and b) along-shore component computed from the observed current (red dots) at Bombay High and that simulated by the tidal model during 24th December, 1981 - 3rd January, 1982 when the original (blue line) and the modified ETOPO5 (black line) is used

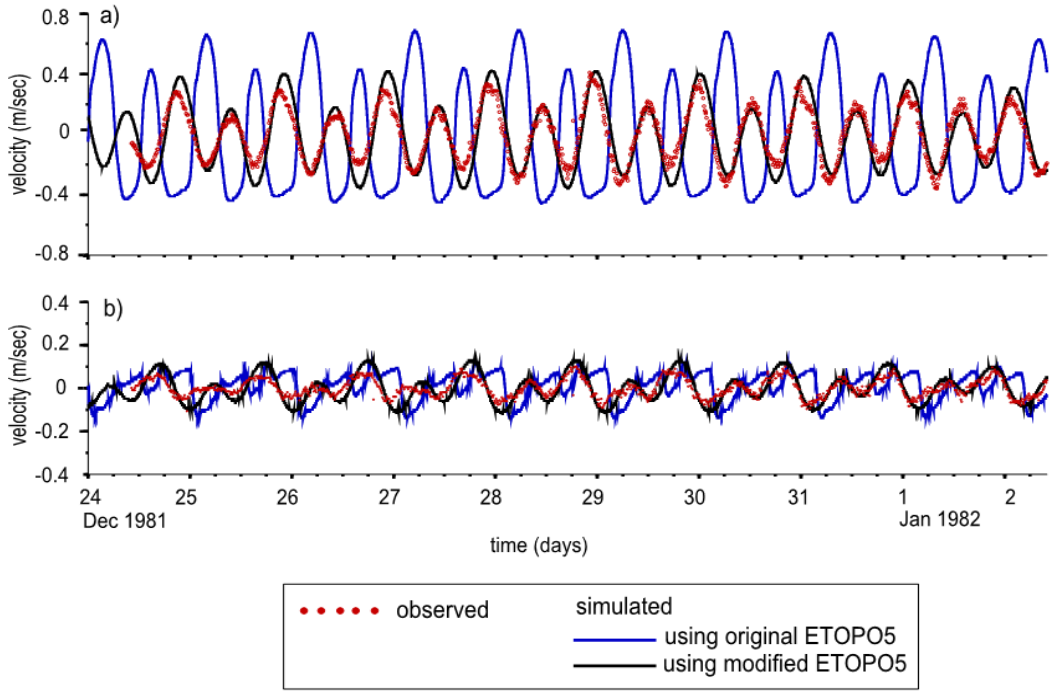

3.4 Conclusion

We have developed an improved 5 arc bathymetric dataset derived from digitized contours and sounding depths values for the entire Indian Ocean north of 38˚S and between 20˚E and 112˚E. The original ETOPO5 bathymetry data is shown to be inaccurate in shallow regions. In order to generate the modified dataset, the shallow depth values (less than 200 m) derived from the hydrographic charts were gridded and then blended with the deeper depth values (greater than 200m) from the original ETOPO5 dataset using appropriate merging technique to ensure smooth transition between the two dataset. We have demonstrated the improvements of the modified dataset over the original ETOPO5 dataset using a tidal circulation model. However, the drawback of the modified dataset is that the maps used for digitization are of different resolutions that lead to sparse data in some regions. The modified ETOPO5 bathymetric dataset are available at the site (http://www.nio.org/index/option/com_subcategory/task/show/title/Sea-floor%20Data/tid/2/sid/18/thid/113).

Chapter 4

Simulation of tides in the Bay of Bengal

4.1 Introduction

The magnitude and extent of severity of storm surges produced along a coast due to a tropical cyclone not only depends on the magnitude of meteorological forcing but also depends on the phase of tide at that location. The worst disasters occur when large surges coincide with high tide [Murty et al., 1986; Flather, 1994]. The real magnitude of storm surges can be predicted accurately only if the interaction between tides and surges are taken into account. Therefore, as a first step towards simulating the combined effect of tides and surges, it is useful to develop a model driven by tides alone [Jones and Davies, 2005], which can be efficiently validated with locally available tide gauge records. The tidal model can, then, be modified to incorporate meteorological forcing to simulate storm surges.

In addition, the tidal model can be used to extract the amplitudes and phase of tidal constituents, which are useful to predict high and low tides at a place. As mentioned in Section 1.5, the attempts made to understand the characteristics of tides a in the Bay of Bengal are very limited. Murty and Henry [1983] developed co-tidal charts of major tidal constituents M_2, S_2, K_1, and O_1 in the Bay with the aid of numerical model. The model was driven by tidal elevations prescribed along the southern open boundary of the model obtained by linear interpolation of widely separated tidal observations in Sri Lanka, the Nicobar Islands and Thailand, as there was lack of information on tidal elevations in the deep regions.

Fortunately with the advent of satellite altimeter since 1992, the present global tidal models, which assimilate altimetry data, can provide reliable information on tides in oceans, except very near the coast. The global tidal models

can be used to extract composite tidal elevations as well as the amplitudes and phases of the tidal constituents at relatively deep locations.

This chapter describes the simulation of tides in the Bay of Bengal and validation of tidal model. As evident from Figure 1.2, the major semi-diurnal and diurnal constituents that have relatively high amplitudes are M_2, S_2, N_2 and K_1, O_1, respectively. Separate simulations were carried out for each of these major tidal constituents in order to generate co-tidal and co-range charts for the Bay of Bengal, which is also described in this Chapter.

4.2 Data and methodology

4.2.1 Global Tidal Model - FES2004

The present global tidal models, developed by assimilating altimetric data obtained from TOPEX/Poseidon (T/P), are found to perform better than the earlier models of Schwiderski [1980] and Cartwright and Ray [1991] [Andersen et al., 1995], with significant improvement in deep ocean (ocean depth greater than 1000 m) where the accuracy approaches that of tidal analysis method [Shum et al., 1997]. Shum et al. [1997] compared ten global models developed prior to 1997 and showed that the models agreed within 2-3 cm in deep ocean (where ocean depth is greater than 800 m). Among the different T/P based models, Shum et al. [1997] recommended CSR3.0 [Eanes and Bettadpur, 1996] and FES95.2.1 [Le Provost et al., 1998] models to be superior to other global models.

The FES (Finite Element Solution) global tidal model series were developed by Christian Le Provost [Le Provost et al., 1994]. FES2004 [Lyard et al., 2006] is the latest version preceded by FES99 [Lefevre et al., 2002], FES98 [Lefevre et al., 2000], FES95.2.1, and FES94 [Le Provost et al., 1994]. Tide gauge data from several data banks and altimeter dataset from TOPEX/Poseidon and ERS-2 were assimilated into the FES2004 to improve the accuracy of the solutions. The other improvements of FES2004 solution over FES99 are refinement of element mesh up to 1/8° grid resolution, inclusion of S1 tide from Richard Ray and inclusion of four long hydrodynamic period waves [Lyard et al., 2006]. Additionally, FES2004

data package includes prediction code through which composite tidal elevations can be easily extracted at required grid points for any time period along the open boundary of regional model.

In the FES2004 datasets, though documented to be the most accurate among the FES series, ambiguity in the tidal solutions in coastal and shelf regions still persist [Lyard et al., 2006]. Subeesh [2010] evaluated the accuracy of tidal constituents obtained from two global tidal models FES2004 and OTPS [Egbert and Erofeeva, 2002] for the Indian Ocean. The author computed the root mean square error (RMSE) for the two global models between the predicted and observed tides at three island stations in the equatorial Indian Ocean and three coastal stations in the Arabian Sea. Subeesh [2010] concluded that the RMSE for the major tidal constituents obtained from FES2004 were less than that obtained from OTPS by 15% at most of the stations, except at two stations where the RMSE for FES was higher by 3%.

Figures 4.1 to 4.5 show the distribution of amplitude and phase of the major tidal constituents M_2, S_2, N_2, K_1 and O_1 in the Bay of Bengal obtained from the FES2004 datasets. The discrepancies in the FES solutions near the coastal areas are evident from the scatter plots (Figure 4.6) of the amplitudes of major tidal constituents from FES2004 dataset and the amplitudes obtained from the Admiralty Tide Table (ATT) at different stations along the coast of Bay of Bengal whose locations are tabulated in Table 4.1. The highly scattered values show that FES2004 is unable to provide accurate solutions at most of the coastal stations.

Lyard et al. [2006], in order to increase the accuracy of tidal prediction in shallow waters, emphasized on the development of high resolution regional tidal models which can accurately reproduce the tidal dynamics on shelves and shallow regions. In the last few decades, a few regional models have been developed which utilized the tidal elevations extracted from FES global model to prescribe the open boundary conditions. Jarosz et al. [2005], in order to describe the tidal characteristics of Bab el Mandeb Strait, developed a barotropic model which was driven by tidal elevations generated from tidal harmonic constituents extracted from FES95.2. Unnikrishnan et al. [1999] studied the propagation of tides in the

Gulf of Khambhat and Bombay High regions using tidal model driven by harmonic constituents extracted from FES94.

Figure 4.1 Distribution of amplitude and phase of M_2 tide in the Bay of Bengal obtained from FES2004 as a) co-range lines and b) co-tidal lines. Amplitudes are given in centimetres and phase G is given in degrees.

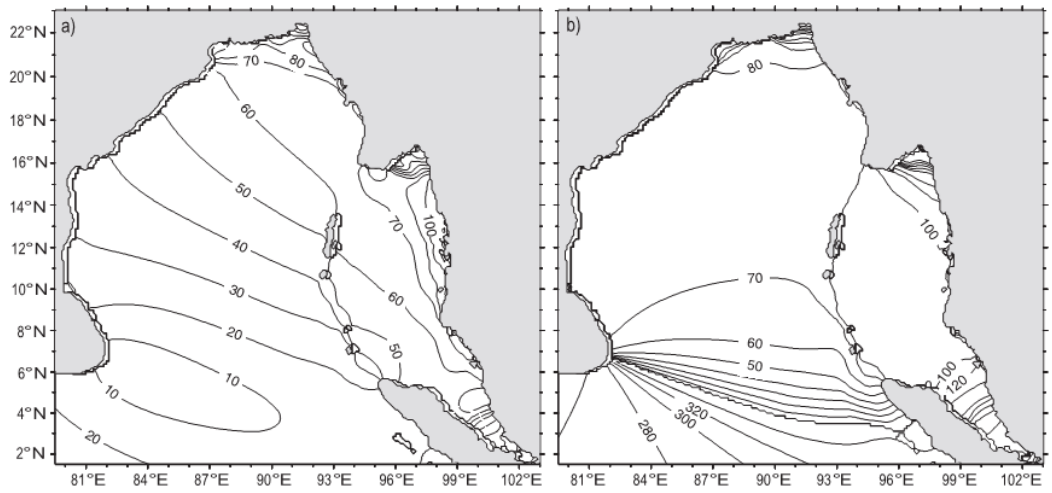

Figure 4.2 Distribution of amplitude and phase of S_2 tide in the Bay of Bengal obtained from FES2004 as a) co-range lines and b) co-tidal lines. Amplitudes are given in centimetres and phase G is given in degrees.

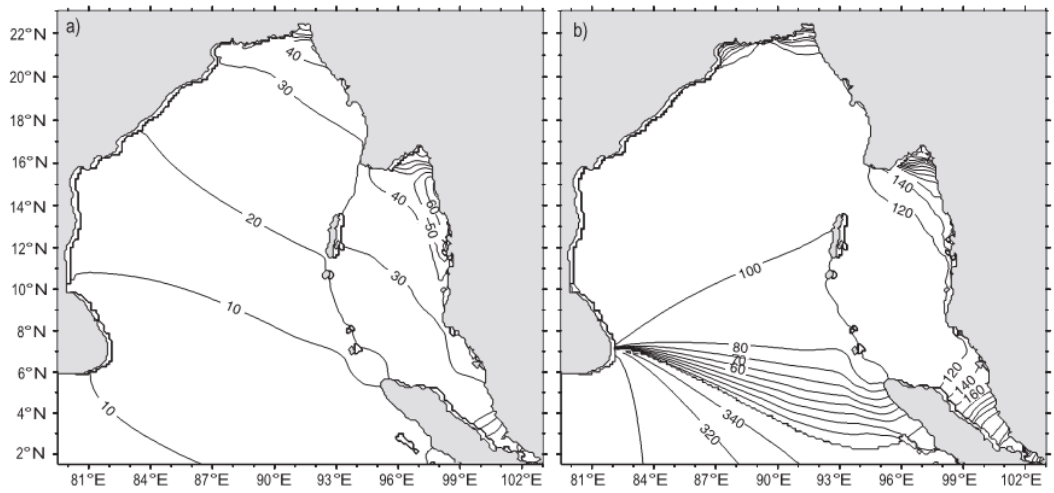

Figure 4.3 Distribution of amplitude and phase of N_2 tide in the Bay of Bengal obtained from FES2004 as a) co-range lines and b) co-tidal lines. Amplitudes are given in centimetres and phase G is given in degrees.

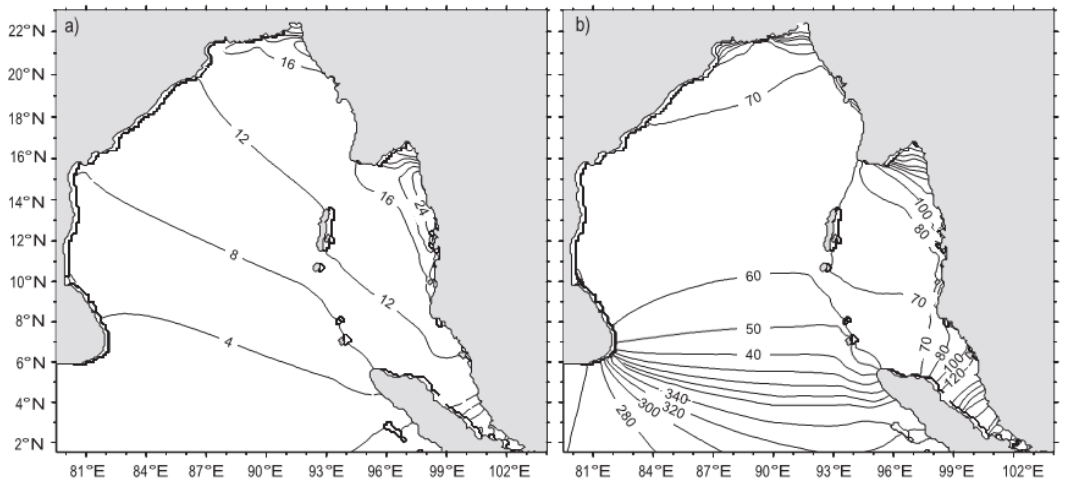

Figure 4.4 Distribution of amplitude and phase of K_1 tide in the Bay of Bengal obtained from FES2004 as a) co-range lines and b) co-tidal lines. Amplitudes are given in centimetres and phase G is given in degrees.

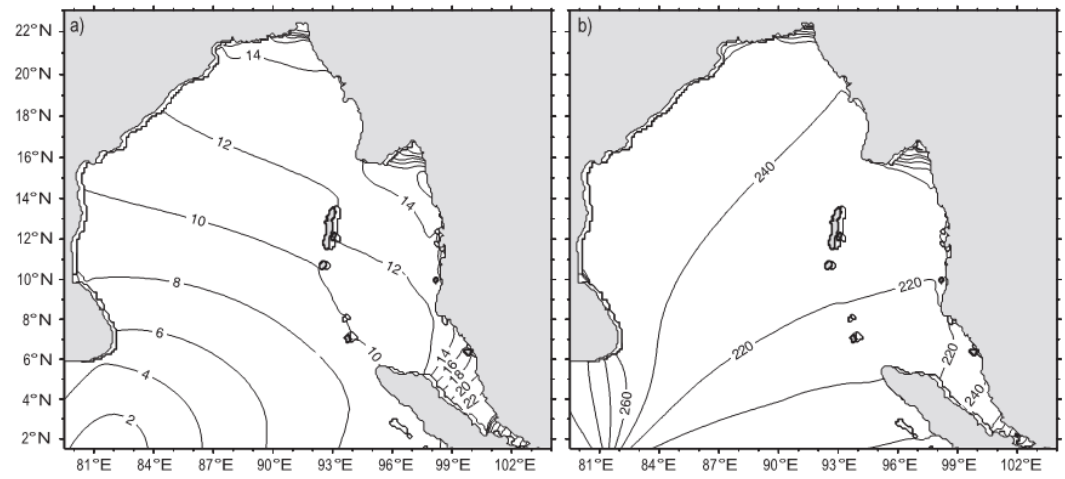

Figure 4.5 Distribution of amplitude and phase of O_1 tide in the Bay of Bengal obtained from FES2004 as a) co-range lines and b) co-tidal lines. Amplitudes are given in centimetres and phase G is given in degrees.

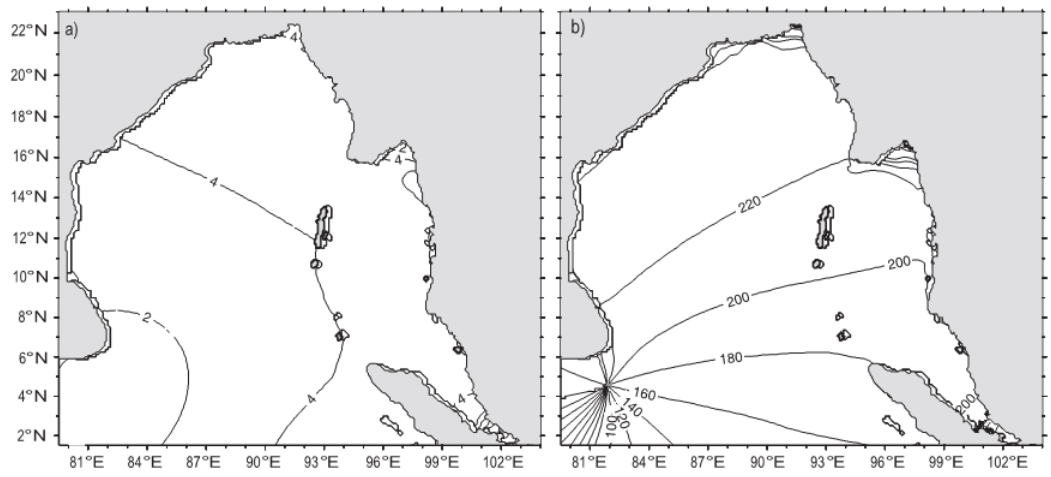

4.2.2 Tidal Model for the Bay of Bengal

In the present study, two different numerical experiments were carried out:

i. Simulation of composite tides
ii. Simulation of each of the five major tidal constituents M_2, S_2, N_2, K_1 and O_1.

The data and methodology adopted for these simulations are described in this section. The hydrodynamic equations and the numerical techniques used to solve the equations are presented in Section 2.2 and 2.4, respectively. The numerical solution of the equations is obtained by discretizing the equations in space using an explicit finite difference scheme over a uniformly staggered Arakawa-C grid and in time using leap-frog technique. The model domain covering the entire Bay of Bengal, including Andaman Sea and Malacca Strait, with north-south extension from 1.5°N to 23°N and east-west extension from 79.8°E to 103°E is shown in Figure 4.7.

Figure 4.6 Scatter plot of the amplitudes of tidal constituents a) M_2, b) S_2, c) K_1, and d) O_1 extracted from FES2004 dataset and that obtained from Admiralty Tide Table at different stations along the coast of Bay of Bengal (locations tabulated in Table 4.1 and shown in Figure 4.7). The stations located in different regions (regions categorized as per Table 4.1**)** are marked with different symbols.

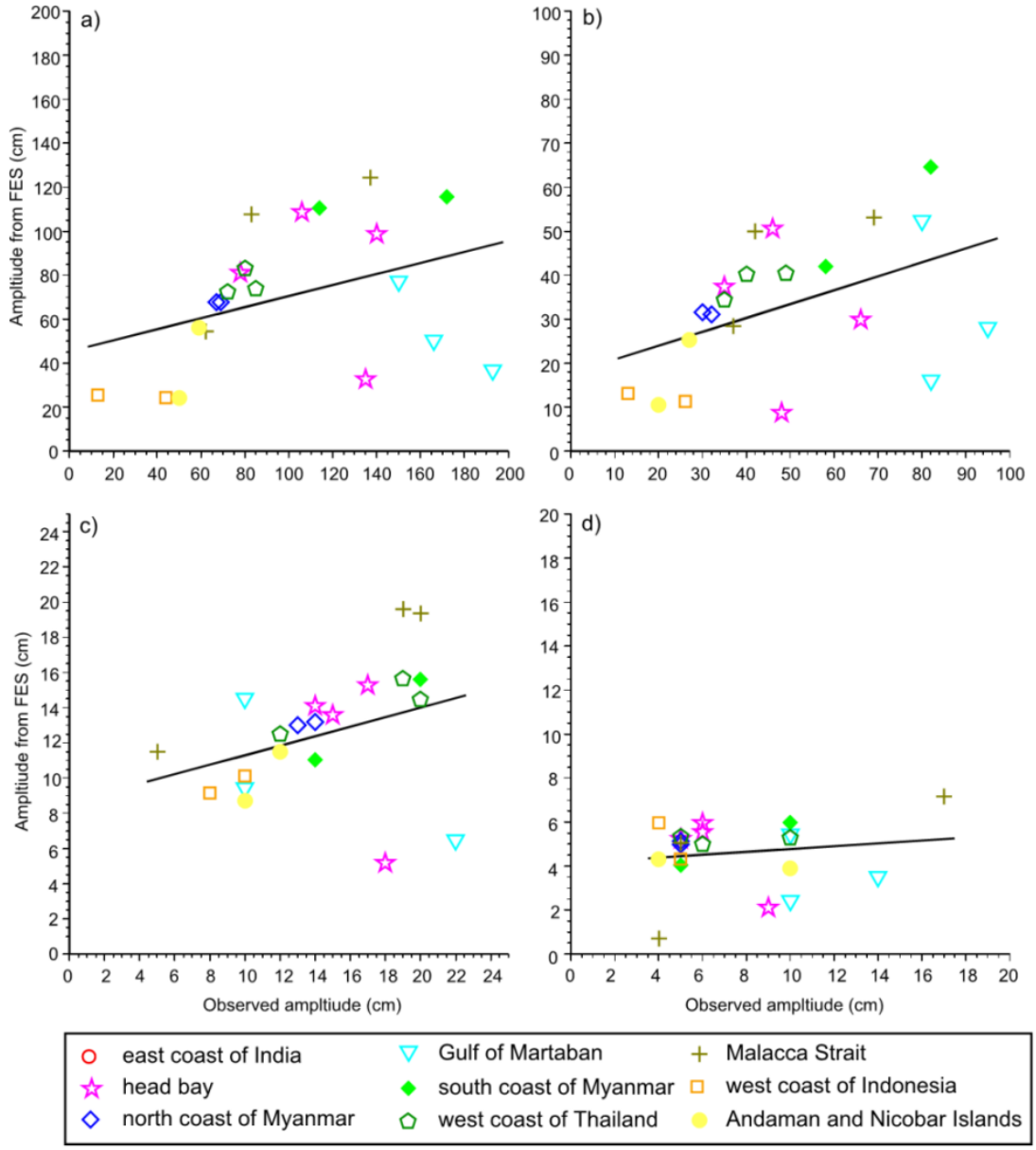

Figure 4.7 Model domain showing the 5 min (approximately 9.2 x 9.2 km) computational grid and the location of 114 stations at which the simulated tidal elevations were extracted. The stations include the 13 Standard Ports (circles) and 31 Secondary Ports (stars) at which the model derived tidal constituents are compared with the observed constituents. The names of the Standard and Secondary Ports are referred in Table 4.1**.** The dashed lines represent the two southern open boundaries along 1.5°N and the western open boundary along 79.8°E. The coastlines of the seven countries bordering the Bay of Bengal and the four maritime states along the east coast of India are highlighted with different colours.

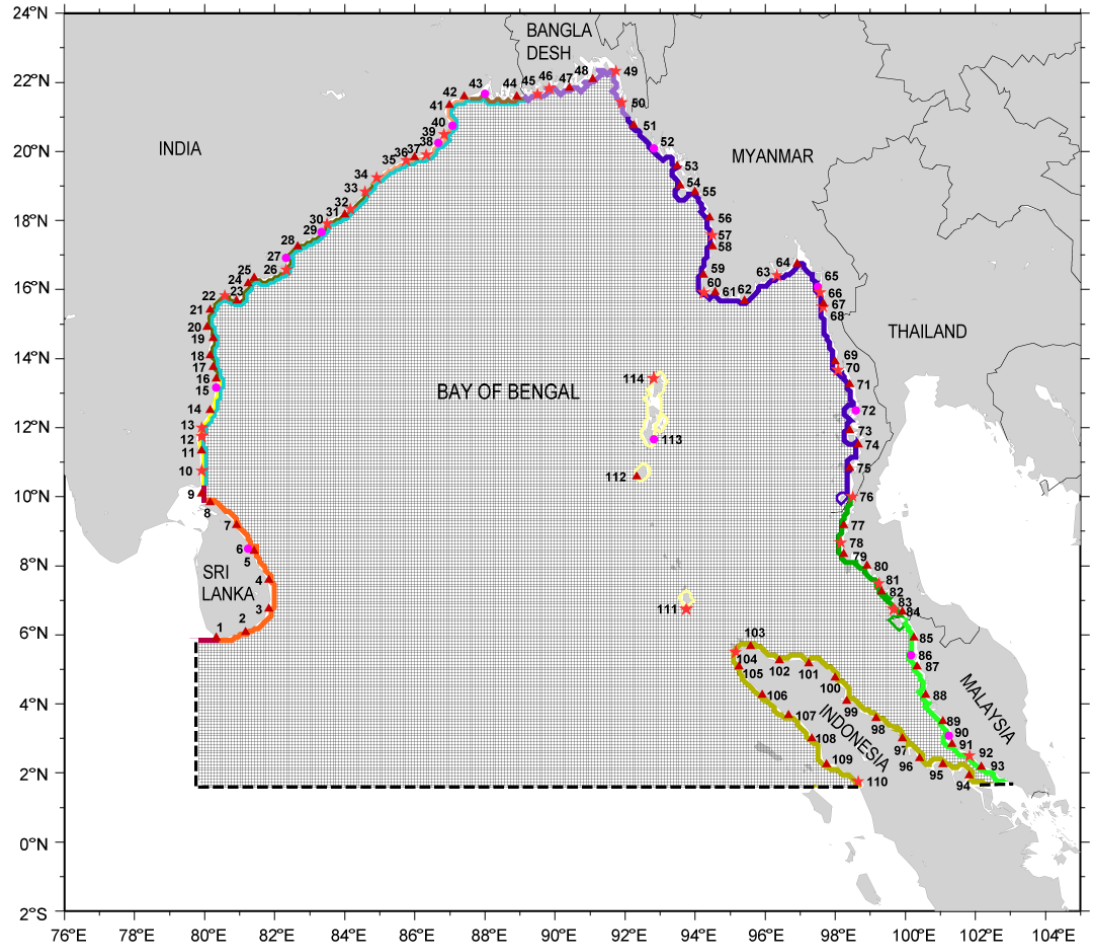

Table 4.1 The name and location of 13 Standard Ports (bold) and 31 Secondary Ports as documented in Indian Tide Table and Admiralty Tide Table, respectively. The Time Zone and the height of Mean Sea Level (MSL) with respect to Chart Datum (CD) at each Port are also tabulated. The longitude and latitude of the grid points closest to location of station and the depth at that point in the model domain is also shown.

Country	St No.	Station Name	Longitude (°E) /Latitude (°N)	Time Zone (hours)	MSL (m)	Corresponding Lon(°E) /Lat(°N) in model	Depth (m)
Sri Lanka	**6**	**TRINCOMALEE**	**81.217, 8.550**	**-5.30**	**0.39**	81.250, 8.500	24.268
East coast of India	10	Nagapattinam	79.850,10.767	-5.30	0.34	79.917, 10.750	11.026
	12	Cuddalore	79.783, 11.933			79.917, 11.750	16.200
	13	Pondicherry	79.833, 11.933			79.917, 12.000	18.076
	15	**CHENNAI**	**80.300, 13.100**	**-5.30**	**0.65**	80.333, 13.167	13.318
	22	Surya Lanka	80.533, 15.850			80.583, 15.833	4.932
	26	Sacromento Shoal	82.317, 16.600			82.333, 16.583	13.888
	27	**KAKINADA**	**82.250,16.933**	**-5.30**	**0.87**	82.333, 16.917	0.293
	29	**VISAKHAPATNAM**	**83.283, 17.683**	**-5.30**	**0.84**	83.333, 17.667	23.074
	30	Bhimunipatnam	83.450, 17.900			83.500, 17.917	6.650
	32	Kalingapatnam	84.133, 18.350			84.167, 18.333	14.246
	33	Baruva	84.600, 18.867			84.583, 18.833	13.045
	34	Gopalpur	84.917, 19.267			84.917, 19.250	10.158
	35	Chilka Mouth	85.767, 19.717			85.750, 19.750	12.289
	37	Devi River Entrance	86.367, 19.950			86.333, 19.917	17.260
	38	**PARADIP**	**86.683, 20.267**	**-5.30**	**1.66**	86.667, 20.250	5.791
head bay	39	False Point	86.783, 20.417			86.833, 20.500	9.047
	40	**SHORTT ISLAND**	**87.067, 20.783**	**-5.30**	**1.92**	87.083, 20.750	2.034
	43	**SAGAR ROADS**	**88.050, 21.650**	**-5.30**	**3.00**	88.000, 21.667	1.224
	45	Pussur River Entrance	89.467, 21.800	-6.00	1.70	89.500, 21.667	4.741
	46	Tiger Point	89.833, 21.850			89.833, 21.833	0.297
	49	Chittangong	91.833, 22.333			91.750, 22.333	2.282
	50	Cox's Bazar	91.983, 21.433			91.917, 21.417	5.561
north coast of Myanmar	**52**	**AKYAB**	**92.900, 21.133**	**-6.30**		92.833, 20.083	4.674
	57	Gwa Bay	94.567, 17.583			94.500, 17.583	15.222
	60	Bassein River Entrance	94.267, 15.867	-6.30		94.250, 15.917	3.417
Gulf of Martaban	63	Elephant Point	96.300, 16.500			93.333, 16.417	0.394
	65	**AMHERST**	**97.567, 16.083**			97.500, 16.083	5.475
	66	Double Island	97.583, 15.866			97.583, 15.917	10.304
	68	Bentinck Sound	97.683,15.533			97.667,15.500	-8.595

Table 4.1 Continued

south coast of Myanmar	70	Sinbyubyin	98.250,13.850			98.083,13.667	-5.13
	72	**MERGUI**	**98.600, 12.433**	**-6.30**	**2.79**	98.583, 12.500	1.545
	76	Pulau Besin	98.483, 9.983			98.500, 10.000	1.183
west coast of Thailand	78	Klong Thung Maphrao	98.250, 8.600			98.167, 8.667	13.134
	81	Ko Ha Hyai	98.900, 7.467			99.250, 7.500	4.719
	83	Pulau Lela	99.700, 6.333			99.667, 6.750	7.285
Malacca Strait	**86**	**PINANG**	**100.35, 5.417**	**-8.00**	**1.69**	100.167, 5.417	1.264
	90	**PELABUHAN KLANG**	**101.35, 3.033**	**-8.00**	**3.21**	101.250, 3.083	10.214
	92	Port Dickson	101.783, 2.517	-8.00	1.50	101.833, 2.500	2.254
west coast of Indonesia	104	Sabang	95.333, 5.833			95.167, 5.500	20.756
	110	Sibolga	98.767, 1.750			98.667, 1.750	13.080
Andaman & Nicobar Islands	111	Galathea Bay	93.850, 6.783			93.750, 6.750	166.000
	113	**PORT BLAIR**	**92.767, 11.683**	**-5.30**	**1.21**	92.833, 11.667	141.770
	114	Temple Sound	92.850,13.433			92.833, 13.417	3.855

Bathymetry

The efficiency of a model to simulate tides accurately depends on the extent to which the shallow depths are represented precisely. The role and importance of the real and accurate bathymetry dataset in numerical models to reproduce the observed tidal elevations and currents have been highlighted by Jarosz et al. [2005] and Sinha et al. [2000]. Therefore, the bathymetry for the domain of the tidal model (Bay of Bengal region) was extracted from the improved ETOPO5 dataset (the generation of the dataset and its improvements in shallow regions are described, in detail, in Chapter 3).

The bathymetric contours for the model domain are shown in Figure 4.8. The maximum depth is found to be 6000 m and the minimum depth is assigned as 5 m. The variation in the width of continental shelf is clearly evident from Figure 4.8, with a narrow shelf (30 km) along the east coast of India which widens towards the head bay and along the southern coast of Myanmar, the width being approximately 190 km and 230 km, respectively. The entire Gulf of Martaban is

very shallow with depth less than 50 m while the depth in the Malacca Strait varies from 150 m in the northern part to less than 10 m at the southern end.

Schematization

The model domain, covering the entire Bay of Bengal, was schematized on a rectangular mesh with uniform grid spacing of 5 min (approximately 9.2 km) resulting in 278 longitudinal grid points and 258 latitudinal grid points. The CFL criteria was used to determine the time step for a grid spacing of approximately 9.2 km and after some numerical experiments, a time step of 12 sec was chosen.

Open boundary conditions

There are two open boundaries on the southern end of model domain along 1.5°N latitude, separated by the land mass of Indonesia. Both the southern boundaries have east west orientation. The open boundary located to the west of Indonesia consists of 228 grid elements while open boundary to the east of Indonesia (i.e., the open boundary located in the Malacca Strait) consists of 10 grid elements. The western open boundary is located along 79.8°E longitude with north-south orientation consisting of 53 grid elements. The locations of the three open boundaries in the model domain are shown as dashed lines in Figure 4.7.

Along the open boundaries, composite tidal elevations were specified to drive the tidal model. With the aid of prediction code included in the FES2004 dataset, a time series of the composite tidal elevations were obtained at selected grid points, which were then linearly interpolated to obtain the tidal elevations at all grid points along the boundaries. In order to simulate each of the tidal constituents, the amplitude and phase of the respective constituent, extracted from the FES2004 dataset at selected grid points, was used to construct time series for each constituent. These elevations were also linearly interpolated to all grid points along the open boundaries.

Figure 4.8 Bathymetry for the model domain extracted from Sindhu et al. [2007]. The depths are in metres relative to MSL

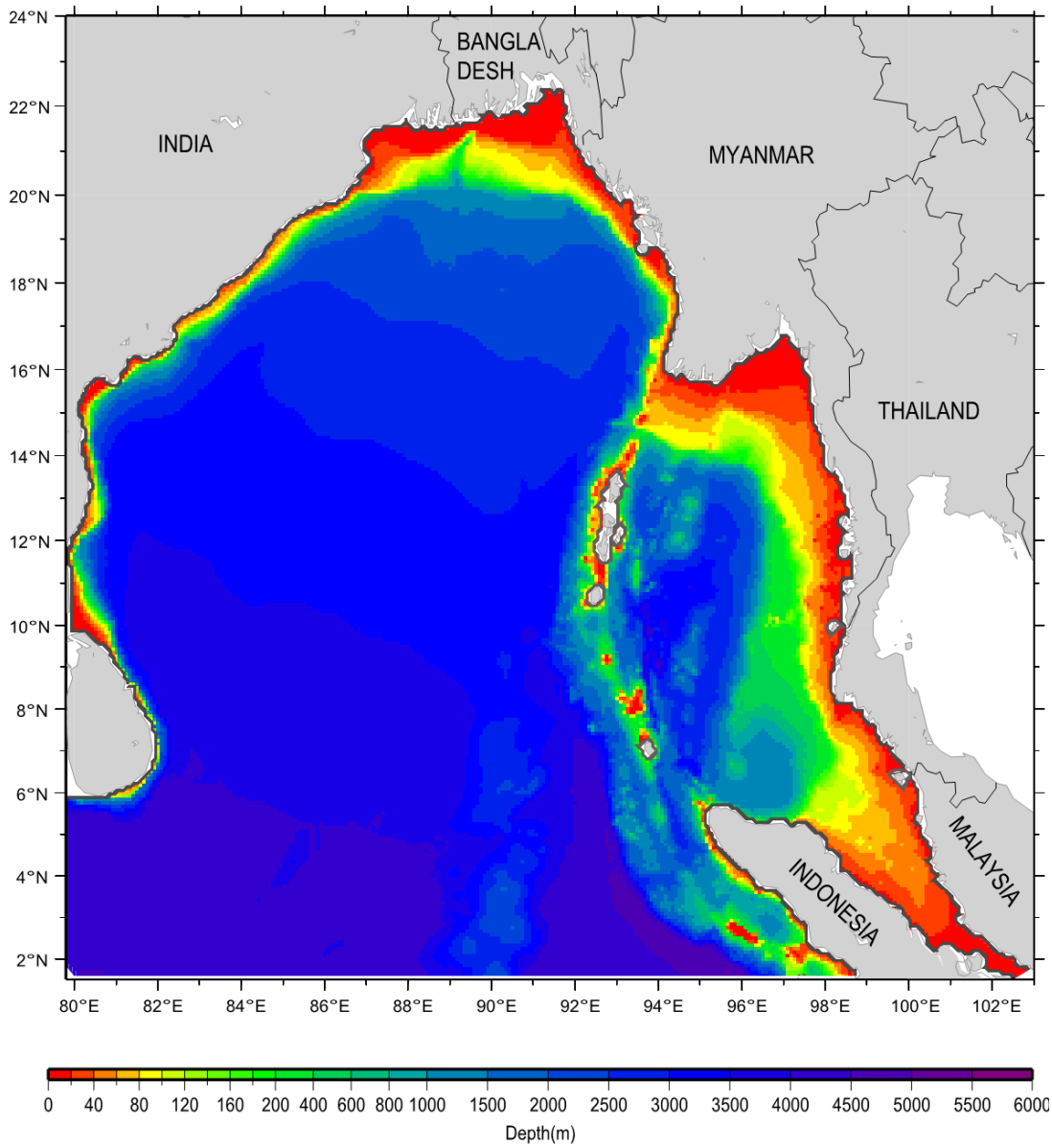

Closed boundary conditions

The coastline of Bay of Bengal and the coastline around small islands in the Bay, when schematized as stair steps for the tidal model, produced 832 and 108 coastal grid points, respectively. The coastal boundaries were treated as impermeable by imposing zero normal flux and slip conditions at the boundaries as discussed in Section 2.5.2.

Data used for model validation

The performance of the tidal model was assessed using the hourly data of observed sea level available from the tide gauges at Chennai, Visakhapatnam, and Paradip for the period 1974-1988.

The model results were also validated against the tidal constituents obtained from Admiralty Tide Table (ATT), Volume 3 published by United Kingdom Hydrographic Office [UKHO, 2000], which provides the amplitude and phase '*g*' of semi-diurnal constituents M_2, S_2 and the diurnal constituents K_1, O_1. Among the various ports documented in ATT, 44 ports are identified to be within the model domain in which 13 are Standard Ports and 31 are Secondary ports. The geographical locations of these ports are listed in Table 4.1 and displayed in Figure 4.7. The amplitudes and phases of the semi-diurnal constituent N_2 were obtained only at Standard and Secondary Ports along the east coast of India from the Special Publications of International Hydrographic Bureau (IHB), Monaco.

In addition to the observed hourly tidal gauge data, which we could get only at three stations, we used the predicted tidal elevations at 13 Standard Ports that were documented in the Indian Tide Tables (ITT) for comparison. The ITT provides predicted time and height of high and low waters based on continuous observation of tide over a period of one year at Standard Ports. The time associated with tidal prediction at a Standard Port is expressed in the official Local Time adopted at that place and all predicted heights are given in metres above Chart Datum (CD). ITT provides information about the Mean Sea Level (MSL) with respect to Chart Datum and Time Zone, which is the relation between Local Time and Greenwich Mean Time (GMT) for each tide gauge station. The

observed hourly time series obtained from the tide gauges at Paradip, Chennai and Visakhapatnam are also relative to Chart Datum and expressed in Local Time (IST).

The name and location of 44 stations along with the Time Zone and MSL adopted for the 13 Standard Ports covering the coast of India, Bangladesh, Myanmar, Thailand and Malaysia are listed in Table 4.1. Table 4.1 also documents the grid points (longitude and latitude) closest to the location of these 44 stations at which the simulated tidal elevations are stored.

4.3 Tuning of the tidal model

The simulation of tides in the Bay of Bengal was carried out for a period of 3 months so that the time series of simulated tidal elevations is long enough to enable accurate extraction of major semi-diurnal and diurnal constituents through harmonic analysis. Therefore, the tidal elevations were extracted from the FES2004 for a period of 103 days from June 20, 1981 to September 30, 1981 and prescribed along the open boundaries. Though it was experimentally evaluated that the model required 48 hours to spin-up and reach a stable state, the model output was stored from 11^{th} day onwards. The investigation carried out by Hall and Davies [2005] implied that the accuracy of the major tidal constituents M_2, S_2, N_2, K_1 and O_1 derived through harmonic analysis of short span data can be improved if the composite tidal elevations are generated from a combined effect of all constituents which includes the higher harmonics and shallow water constituents arising from non-linear interactions and the data are stored every 10 minutes. Therefore, though the time step used in the model was 12 seconds, the simulated composite tide elevations were stored at every 10 minutes for a period of 92 days at 114 grid points along the coast covering almost the entire model domain (Figure 4.7). The 114 stations included the 44 check stations, tabulated in Table 4.1, representing the locations of the Standard/Secondary Ports at which model output was compared with the observed data.

The model was calibrated through fine tuning of friction coefficient, C_d and eddy viscosity, A_H in order to achieve maximum agreement between the simulated

and observed tidal elevations. A detailed analysis of the model results obtained from a series of simulations with friction coefficient ranging from 0.001 to 0.003 suggested an improvement in the model results at shallow coastal areas with increasing C_d values while the tidal elevations in deeper waters (greater than 500 m) appeared to be insensitive to friction coefficient. Therefore, following values were used for C_d :

$$C_d = 0.0025 \text{ for } h \leq 100,$$

$$C_d = 0.002 \text{ for } 100 < h \leq 500,$$

$$C_d = 0.0015 \text{ for } h > 500.$$

In order to test the sensitivity of tidal model to horizontal eddy viscosity, A_H, several experiments were carried out for uniform value of A_H ranging from 1000 to 2000 m^2/sec. Though the simulated tidal elevations were not sensitive to the changes in A_H, relatively better agreement was achieved between observed and simulated elevations for A_H = 1500 m^2/sec.

4.4 Validation of the tidal model

This section describes the validation of tidal model which was carried out in two different ways, as described in Section 4.2.2:

- Comparison of simulated composite tidal elevations stored at grid points that correspond to locations of Chennai, Visakhapatnam and Paradip with the observed sea level data available at these ports.
- Comparison of the model derived amplitudes and phases of the major tidal constituents at 44 stations with those documented in ATT.

In addition, the composite tidal elevation time series were also compared with the predicted high and low water level data obtained from ITT at 13 Standard Ports.

4.4.1 Comparison with observed sea level data

The simulated composite tidal elevations were compared with the observed tide gauge data at Chennai, Visakhaptanam, and Paradip after shifting the datum from

MSL to CD and making necessary adjustment related to the Time Zone as per the relation listed in Table 4.1.

Figure 4.9 shows the time evolution of simulated and observed tidal elevations for the month of August 1981, covering a spring – neap cycle. It is evident that the mixed semi-diurnal tidal ranges and the spring-neap tidal cycles are well reproduced in the model at all the 3 stations - Chennai, Visakhapatnam and Paradip with a RMSE of 7.20, 6.74 and 7.24 cm, respectively.

4.4.2 Comparison with observed amplitudes and phases of tidal constituents

The composite tidal elevation time series, obtained from model simulation, was harmonically analyzed using TASK2000 software [Bell et al., 2000], derived from the TIRA tidal analysis program [Murray, 1964] to obtain the amplitude and phase *G* of the major semi-diurnal and diurnal constituents (hereafter referred to as model derived constituents). Since the span of the data analyzed was more than 90 days, the major semi-diurnal and diurnal constituents could be extracted accurately [Bell et al., 2000]. The phase '*G'* of each model derived constituent at all stations was converted to include the Local Time Zone effect and obtain phase '*g*' using the Equation (1.2) presented in Section 1.1.4.

Figures 4.10 to 4.13 show the amplitudes and phases of the model derived tidal constituents at 114 stations including the 44 check stations at which the observed data are available. The comparison of the amplitudes of model-derived constituent with the observed indicates that the solution fits quite well with the observations. The model derived constituents M_2 and S_2 show high variation in amplitude and the diurnal constituents K_1 and O_1 show relatively constant amplitudes along the coast of Bay of Bengal, which is in agreement with the observed amplitudes.

Figure 4.9 Comparison of simulated tidal elevations (cm with respect to CD) (black line) with the observed hourly tidal elevations (red circles) obtained from tide gauge records at a) Paradip, b) Visakhapatnam, and c) Chennai. The predicted high and low water levels obtained from ITT are also shown (blue circles) for comparison. The time 00 hours corresponds to 00 hours on August 01, 1981.

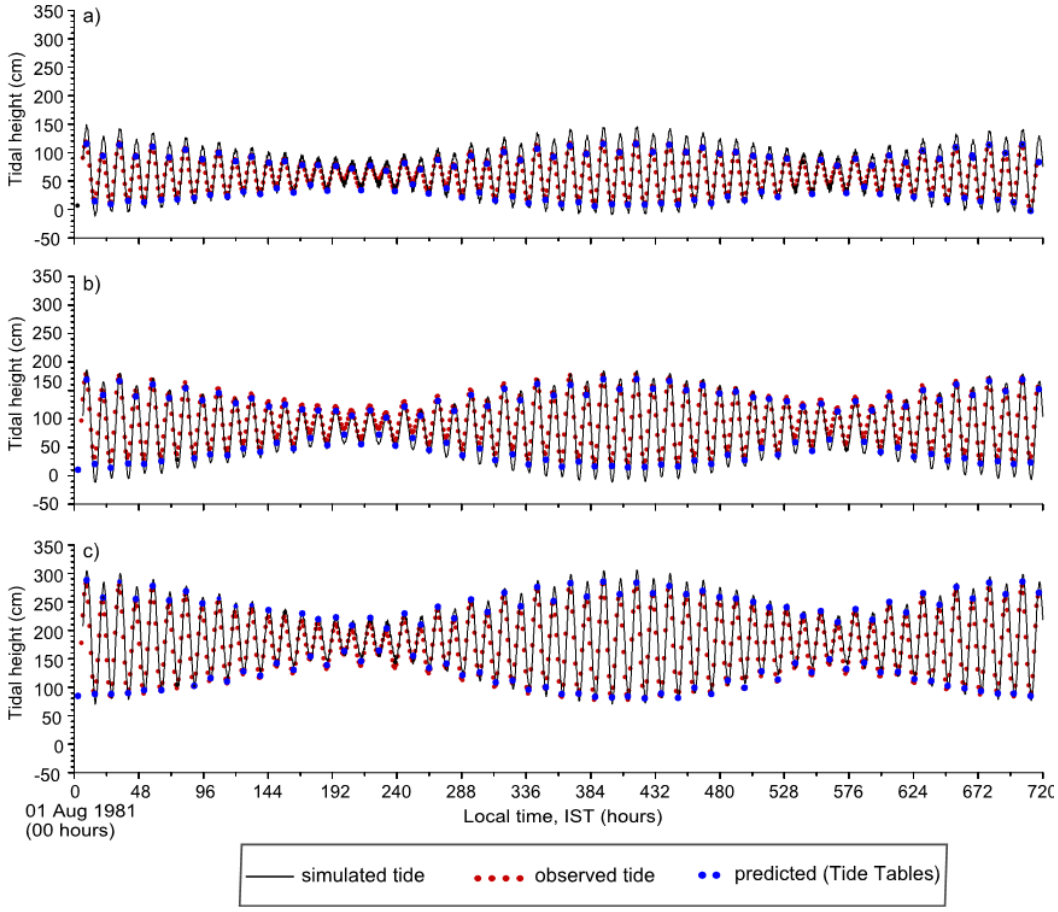

Figure 4.10 Comparison of the model derived and observed amplitudes of semi-diurnal constituents a) M_2, b) S_2, and c) N_2. The amplitudes of the simulated constituents extracted at 114 stations are shown as continuous line while the observed amplitudes of M_2 and S_2 extracted from ATT at 44 stations are indicated as circles. The observed amplitudes of N_2 tide is obtained only at stations along the east coast of India from IHB. The names of the 44 stations are tabulated in Table 4.1. The abscissa represents the station number assigned to the 114 stations, the locations of which are shown in Figure 4.7.

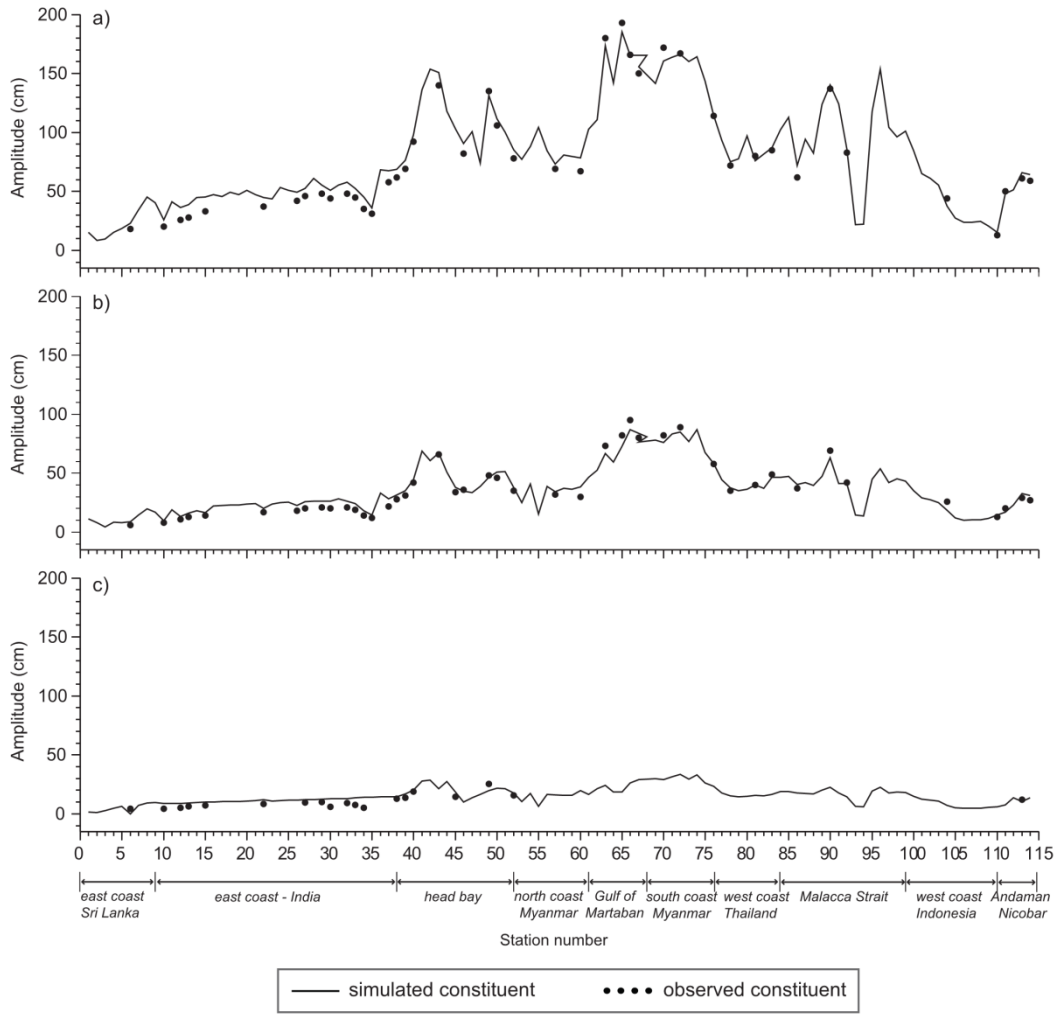

Figure 4.11 Same as Figure 4.10, but for amplitudes of diurnal constituents, a) K_1 and b) O_1.

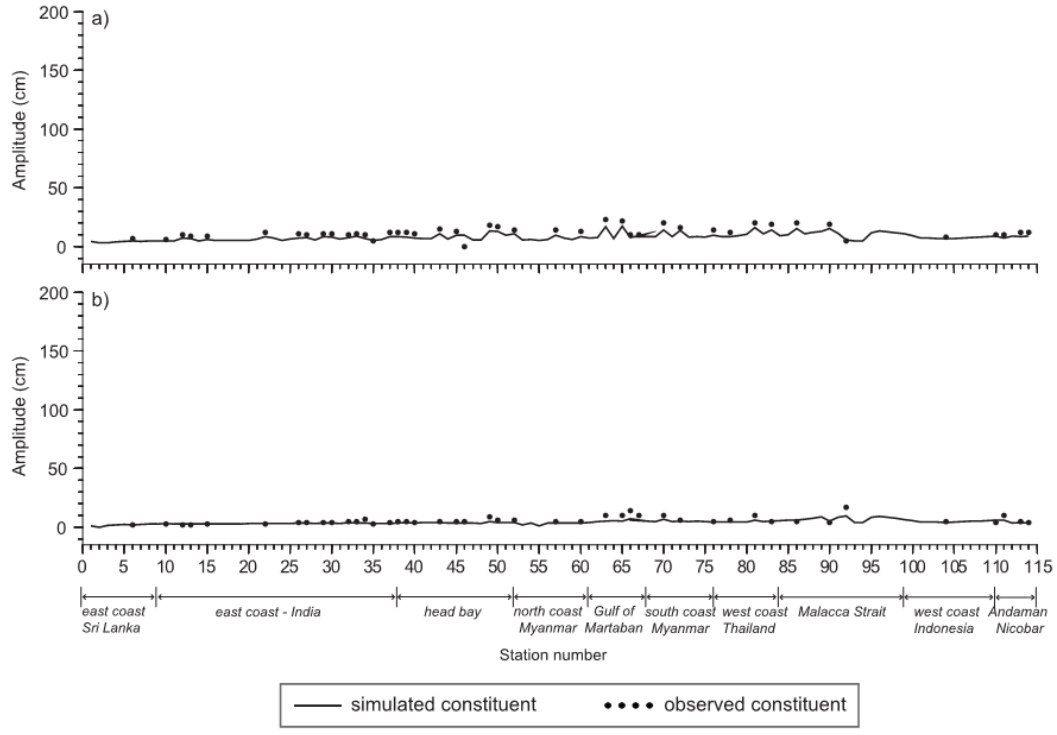

Figure 4.12 Same as Figure 4.10, but for the phases *g* of semi-diurnal constituents a) M_2, b) S_2, and c) N_2.

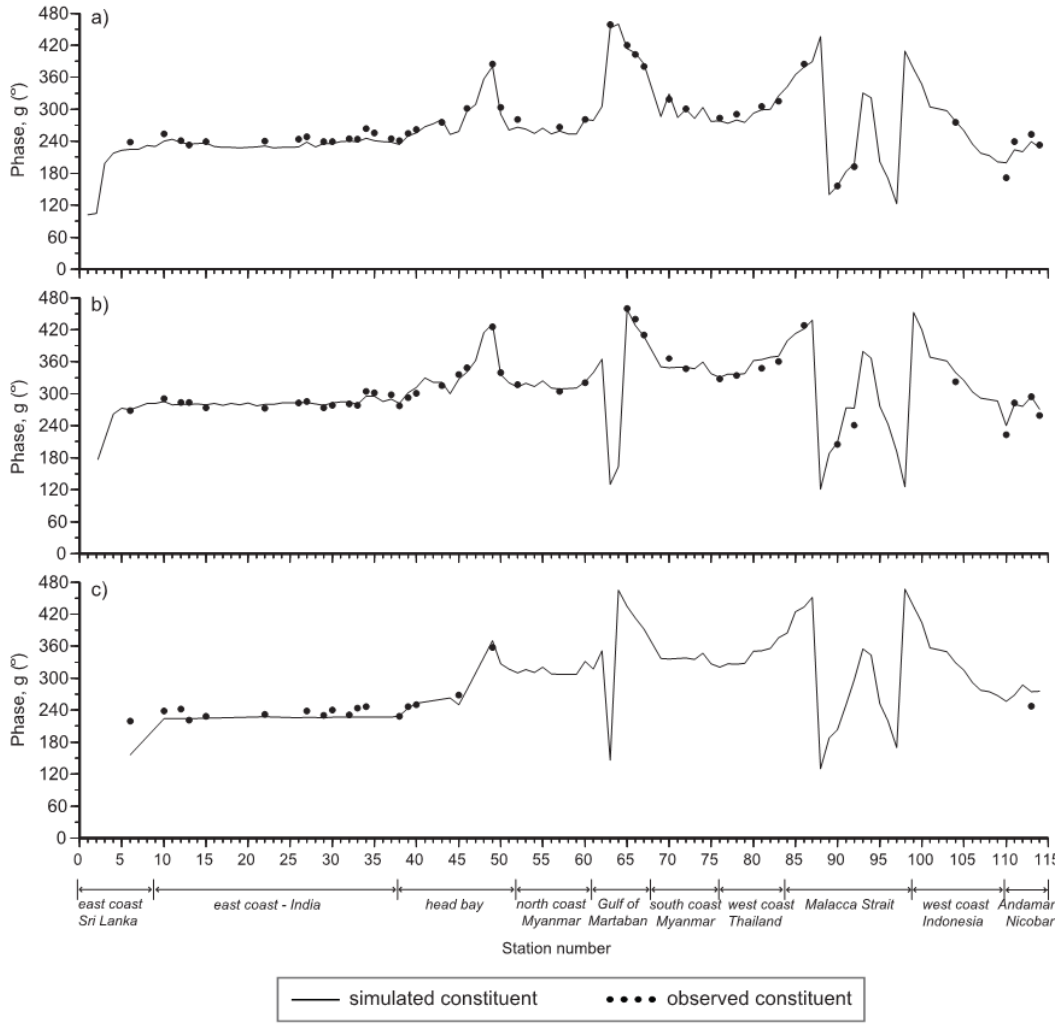

Figure 4.13 Same as Figure 4.10, but for the phases *g* of diurnal constituents, a) K_1 and b) O_1 .

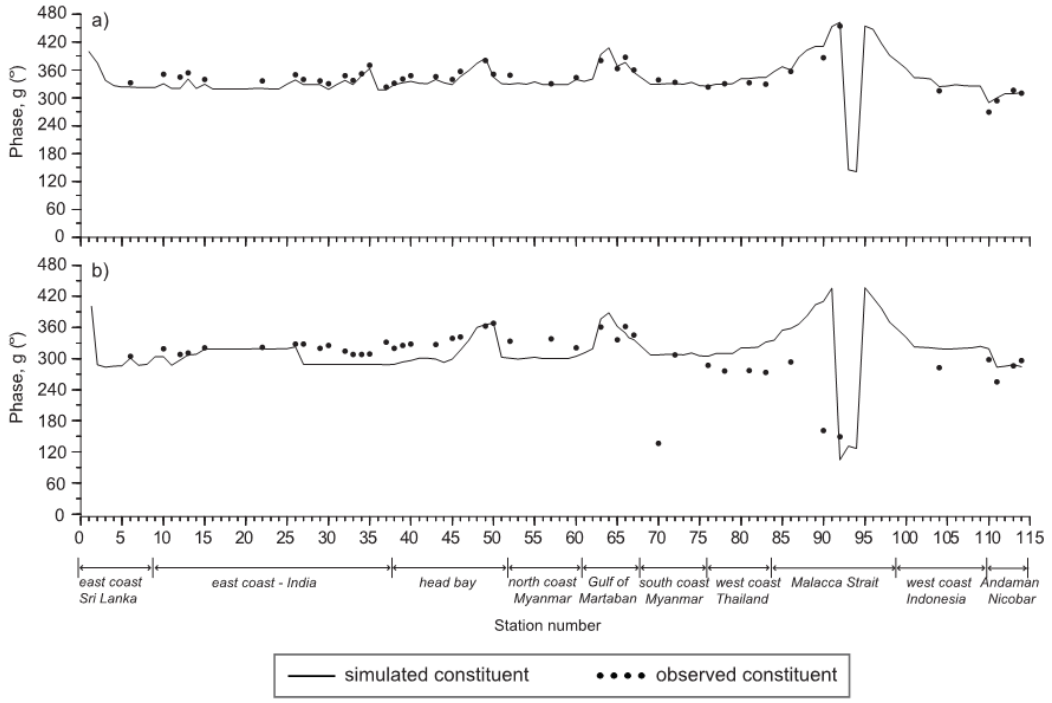

4.4.3 Statistical analysis to assess model performance

The performance of the model is demonstrated with scatter plots of model derived and observed amplitudes and phases of the tidal constituents (Figures 4.14 and 4.15, respectively). It is seen that the major semi-diurnal constituents M_2 and S_2 are simulated accurately and except for some outliers, the model derived and observed M_2 and S_2 amplitudes agree favourably with a correlation coefficient of 0.99 and 0.98, respectively. The model derived M_2 amplitudes show some discrepancies at Sagar Roads, Sabang, Galathea Bay and KoHoKya while S_2 amplitudes stand out as outliers at Sabang and Galathea Bay. However, at nearby locations of these stations, the model-derived amplitudes are found to be close to the observed amplitude suggesting the presence of some local phenomena that the model cannot resolve. The amplitudes of diurnal constituent O_1, being relatively lower than the semi-diurnal constituents, show larger scatter. The scatter plot for the phases of the tidal constituents indicates good agreement between the model derived and observed phases of all constituents (correlation coefficient close to 0.99) except for O_1 which show low correlation of 0.92.

The accuracy of the model results is quantified by estimating mean error (ME) and root mean square error (RMSE) as shown in Equations (4.1) and (4.2) respectively for amplitudes and phases of each of the model derived constituents [Robertson et al., 1998].

$$ME_i = \frac{1}{N}\sum_{N} e_i \tag{4.1}$$

$$RMSE_i = \left[\frac{1}{N}\sum_{N} {e_i}^2\right]^{\frac{1}{2}} \tag{4.2}$$

where $\bar{e}_i$ is the mean error.

In addition, the overall performance of the model is measured by computing the RMS misfit (ORM) as suggested by Matsumoto et al. [2000]:

$$ORM_i = \left[\frac{1}{N}\sum_{N}\frac{1}{2}(A_{s,i}^2 + A_{o,i}^2 - 2A_{o,i}A_{s,i}\cos(g_{s,i} - g_{o,i})\right]^{\frac{1}{2}} \quad (4.3)$$

where, $A_{s,i}, g_{s,i}$ are the model derived amplitude and phase and $A_{o,i}, g_{o,i}$ are the observed amplitude and phase, respectively of the i^{th} constituent.

At majority of stations, the tidal amplitudes of M_2, S_2, K_1 and O_1 derived from the model agree to within 10, 8, 8 and 5 cm respectively of the observed values. The model, on an average, slightly over-estimates the semi-diurnal amplitudes and under-predict the diurnal amplitudes. The largest discrepancies between model results and observations occur in the prediction of M_2 amplitude, as depicted by RMSE, probably due to the outliers seen in Figure 4.14.

The ME computed for the phases of the tidal constituents indicate a phase lag of 9 and 12 minutes for M_2 and K_1 tide, respectively, compared to the observed phases while S_2 and O_1 tides, on an average, appear to arrive earlier by 3 and 7 min, respectively than the observed tide (Table 4.2). The high RMSE for the O_1 phase is assessed to be due to sudden significant change in the phase observed at Sinbyubyin station (136°) compared to the neighbouring stations (approximately 315°) which cannot be resolved by the grid resolution considered in the model. If this station is neglected, the RMSE is found to be approximately 24.8° for O_1 phase.

On the whole, there is a reasonable agreement between the model derived and the observed amplitudes and phases of the semi-diurnal and diurnal constituents with RMSE less than 7 cm and 9.5°. It can be concluded from the RMS misfit (ORM), being less than 9 cm for all the model derived constituents, that despite of the discrepancies between the amplitudes and phases of the model derived and observed constituents at few stations, the model has the capability of reproducing the tides in the area and has sufficient fine grid to capture the near shore tidal variations.

Figure 4.14 Scatter plots of the model derived and observed amplitudes of the tidal constituents a) M_2, b) S_2, c) K_1, and d) O_1 extracted at 44 stations (locations tabulated in Table 4.1 and shown in Figure 4.7). The stations located in different regions (regions categorized as per Table 4.1**)** are marked with different symbols.

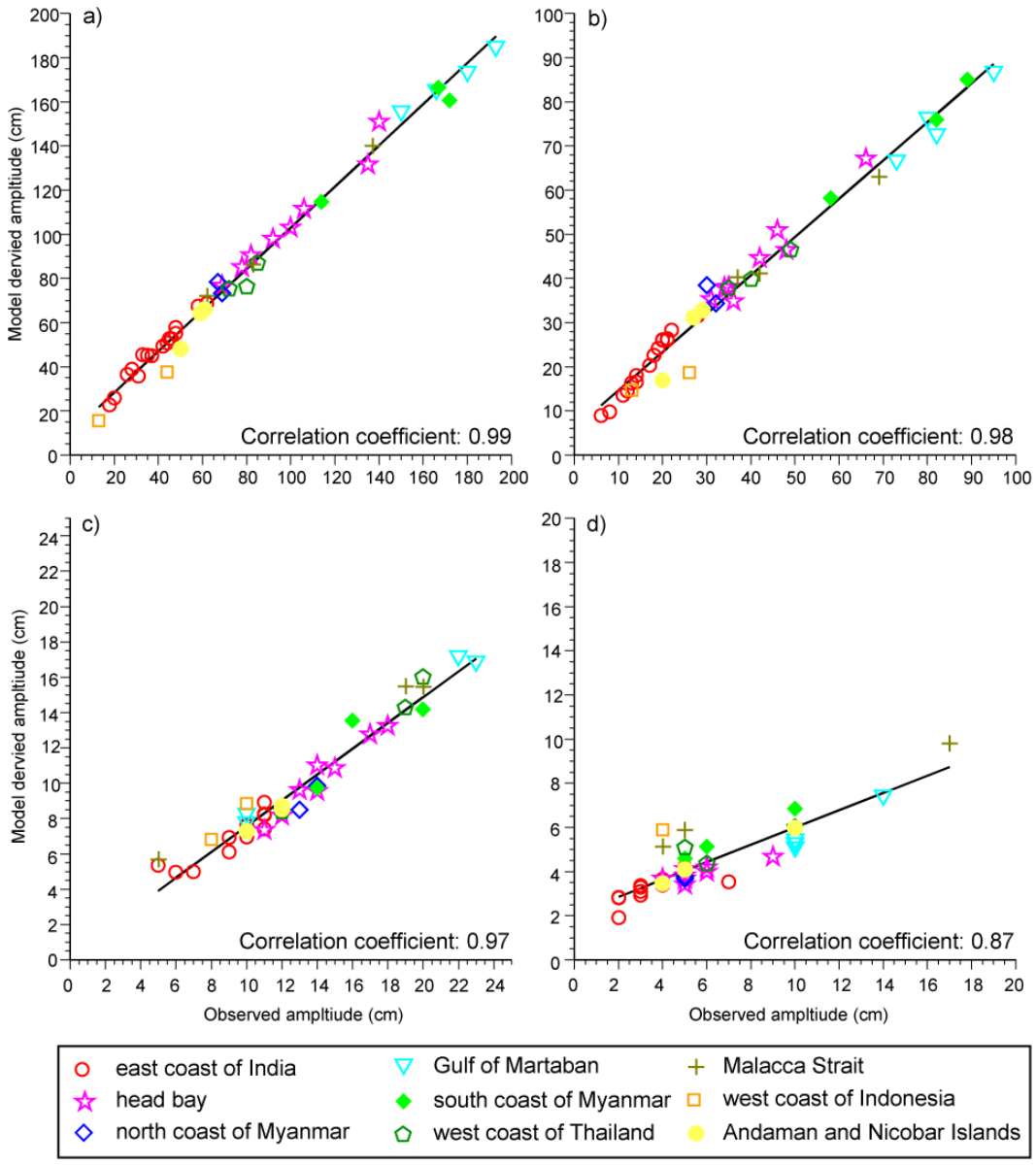

Figure 4.15 Same as Figure 4.14, but for the phases of the tidal constituents a) M_2, b) S_2, c) K_1, and d) O_1.

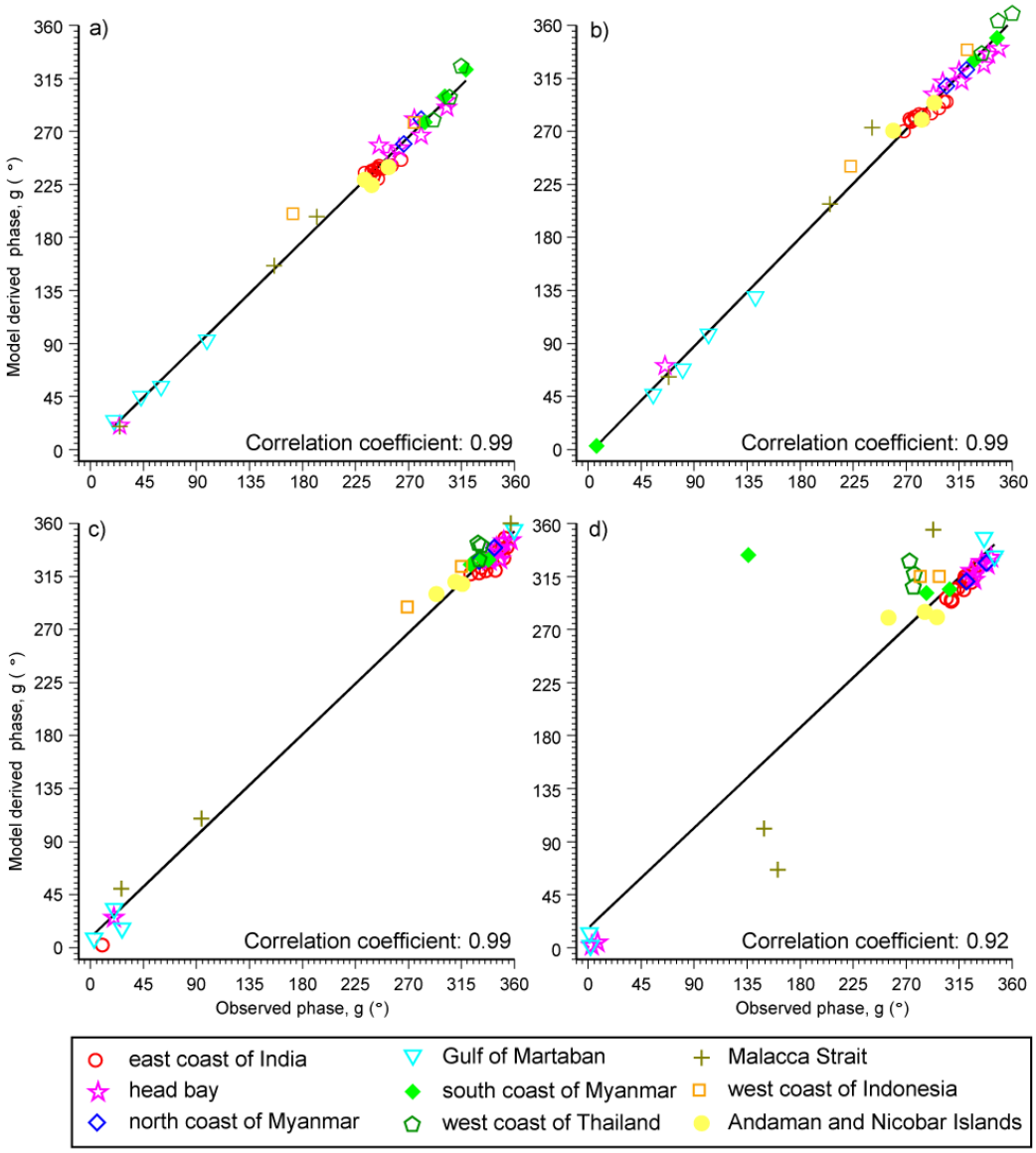

Table 4.2 Error statistics – Mean Error (ME) and Root Mean Square Error (RMSE) for the model derived amplitudes and phases of the major tidal constituents for the coastal stations. The Root Mean Square misfit (ORM) is also tabulated.

Constituent	ME		RMSE		ORM (cm)
	A (cm)	g (°)	A (cm)	g (°)	
M_2	4.38	-4.18	7.04	9.43	9.16
S_2	1.18	1.59	4.44	8.91	5.64
K_1	-3.16	-3.64	3.45	11.06	2.89
O_1	-1.45	1.48	2.47	38.53	3.05

4.4.4 Comparison between simulated and predicted tides extracted from Indian Tide Tables

The datum and time zone of tidal elevations extracted at grid points closest to the location of remaining 10 Standard Ports were also adjusted in time and space, as described in Section 4.4.1 and compared against the predicted high and low waters obtained from ITT for the month of August 1981, covering a spring – neap cycle, as shown in Figures 4.16 to 4.19.

The comparison ensures the efficiency of the model in reproducing the observed tidal range and pattern at all stations that could represent the entire modelled coastline. Therefore, the general characteristic of tides along the coast of Bay Bengal can be described using the model results.

Figure 4.16 Comparison of simulated tidal elevations (cm) (black line) with predicted high and low water levels (circles), obtained from Indian Tide Tables, at a) Trincomalee (along east coast of Sri Lanka), b) Kakinada (along the east coast of India) and c) Port Blair (along the coast of Andaman Islands). The time 00 hours corresponds to 00 hours on August 01, 1981.

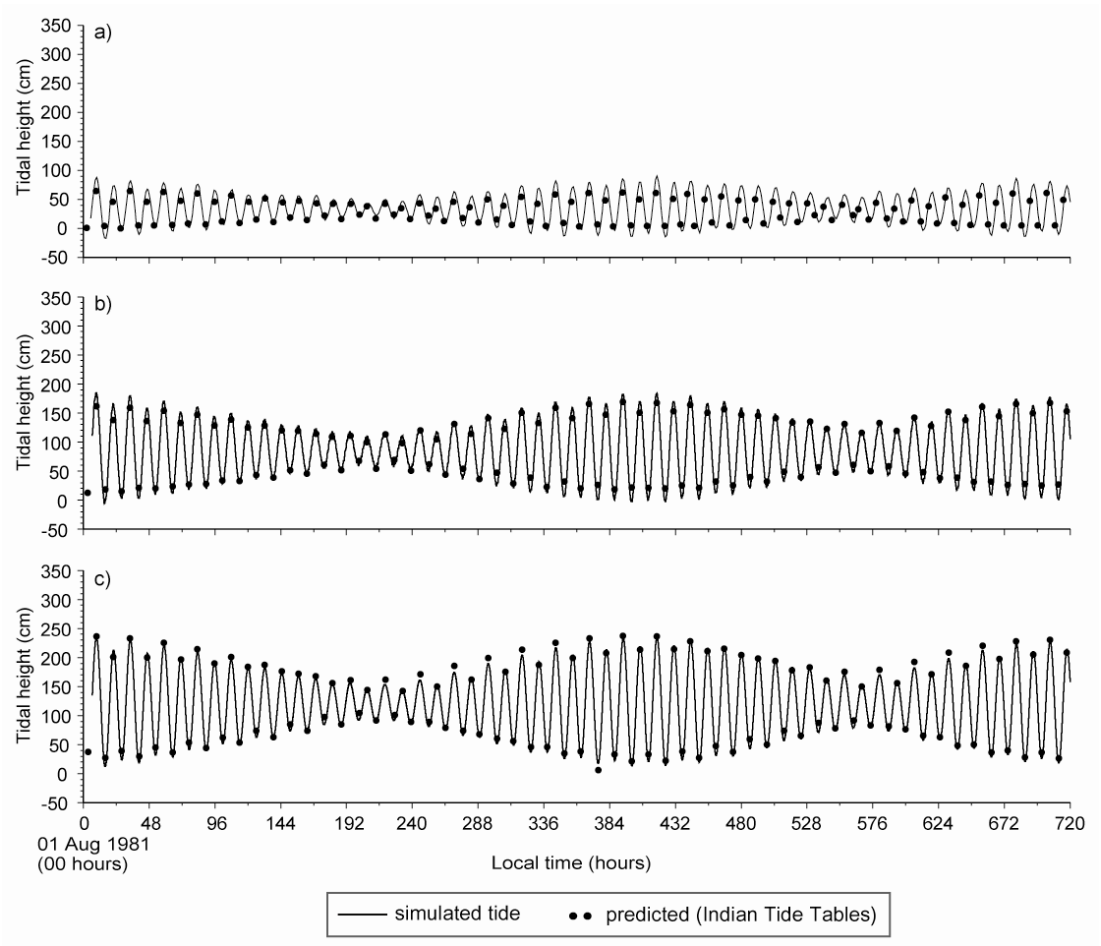

Figure 4.17 Same as Figure 4.16, but for stations in the head bay, a) Shortt Island and b) Sagar Roads.

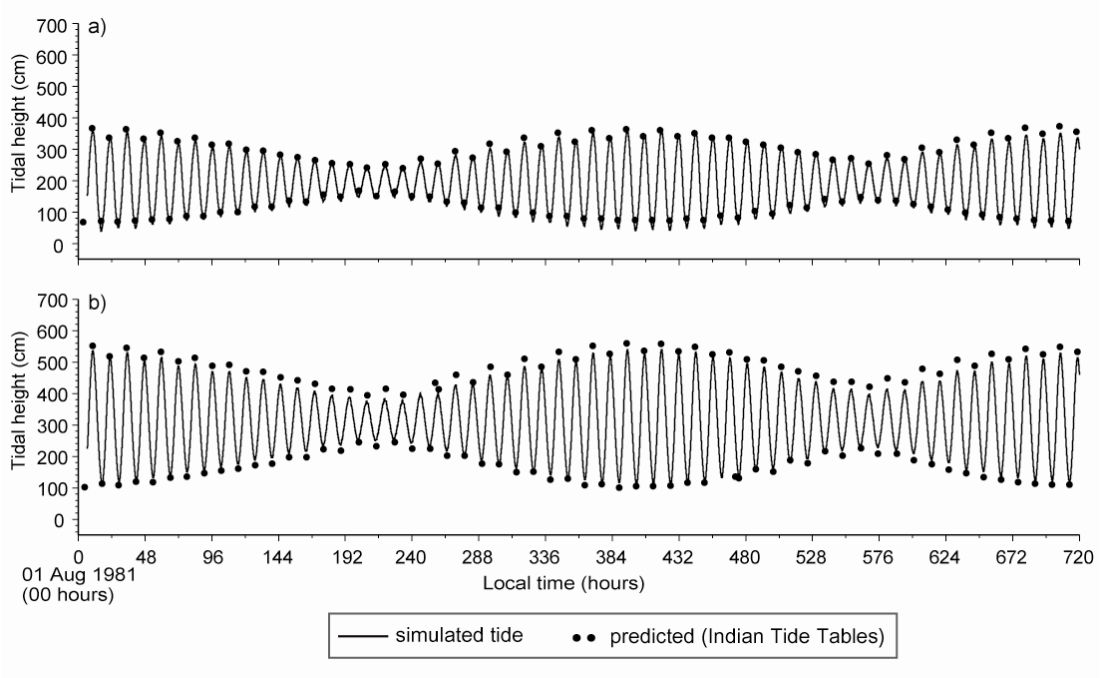

Figure 4.18 Same as Figure 4.16, but for stations along the northern coast of Myanmar at a) Akyab and for stations in the Gulf of Martaban, b) Amherst and c) Mergui.

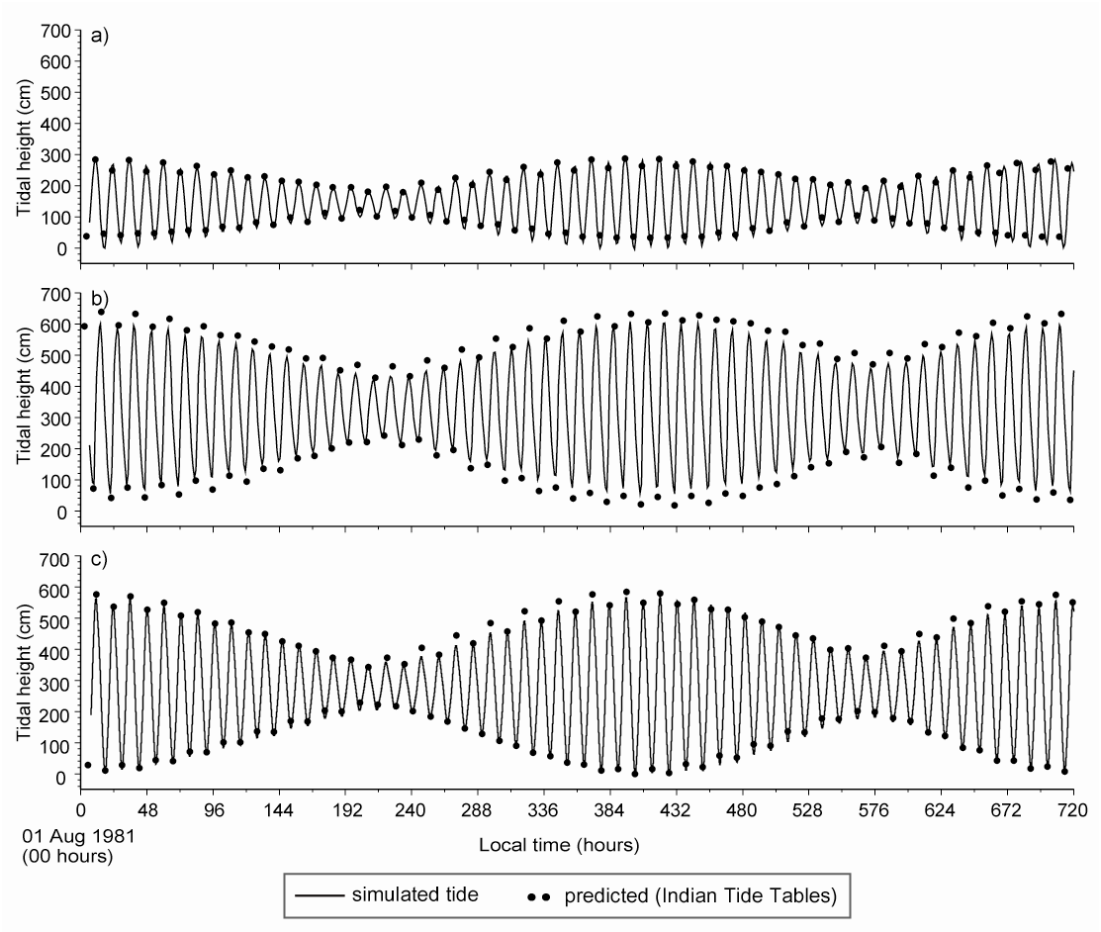

Figure 4.19 Same as Figure 4.16, but for stations along the west coast of Thailand at (a) Pinang, and b) Pelabuhan Klang.

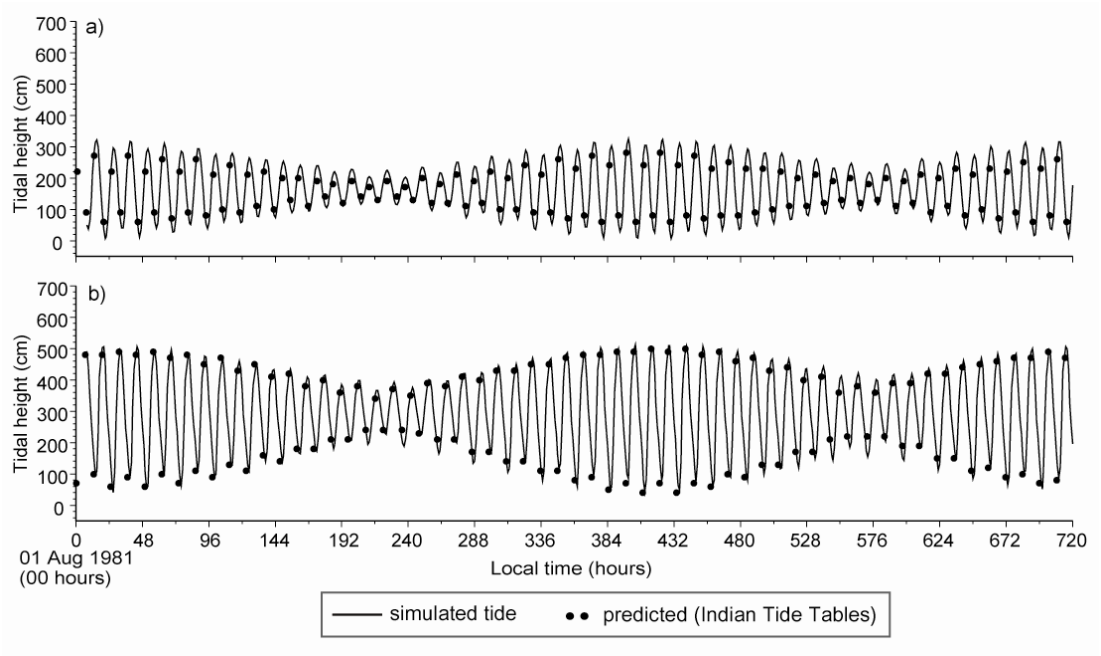

Approximate tidal ranges calculated from simulated tidal elevations during spring and neap tide at 13 stations are presented in Table 4.3. The tidal range is found to be lowest at Trincomalee in Sri Lanka. Along the coast of India, the tidal range vary significantly with relatively low range of 1.1 m at Chennai and reaching as high as 5.3 m at Sagar Roads, located in the head bay as seen from Table 4.3. It is noted that relatively higher tidal range is found at Mergui, located along the coast of Myanmar as compared to the tidal ranges at stations in the head bay. Table 4.3 shows that the highest tidal range (approximately 6.2 m) is observed at Amherst, which is located in the Gulf of Martaban.

Table 4.3 The spring and neap tidal range obtained from the simulated composite tidal elevation time series data extracted at the 13 Standard Ports (name and location tabulated in bold letters in Table 4.1 and shown as solid circles in Figure 4.7.

Station No	Station Name	Spring tidal range	Neap tidal range
6	Trincomalee	0.6	0.1
15	Chennai	1.1	0.2
27	Kakinada	1.5	0.3
29	Visakhapatnam	1.6	0.3
38	Paradip	2.0	0.4
40	Shortt Island	3.0	0.7
43	Sagar Roads	5.3	1.5
113	Port Blair	2.4	0.4
52	Akyab	2.5	0.6
65	Amherst	6.2	0.4
72	Mergui	5.8	1.1
86	Pinang	2.2	0.3
90	Pelabuhan Klang	4.7	1.0

4.5 Simulation of tidal constituents

The tidal elevations applied at the open boundaries of the tidal model was modified, as described in this section, to simulate separately each of the major semi-diurnal (M_2, S_2 and N_2) and diurnal (K_1 and O_1) tidal constituents.

A time series of tidal elevation was constructed for a period of 40 days by using the amplitude and phase of M_2 tide, extracted from FES2004 dataset at selected grid points. The M_2 tidal time series was interpolated to each grid point along the open boundaries of the tidal model. The simulated M_2 tidal elevation was stored at hourly intervals starting from the 10^{th} day at each grid point of the model domain. The amplitudes and phases, computed from the simulated elevations of M_2 tide at each grid point of the model domain, were used to generate co-range (contour maps showing lines of equal amplitudes) and co-tidal charts (contour maps showing lines of equal phases), respectively. Similar procedure was followed for the simulation of S_2, N_2, K_1 and O_1.

4.6 Co-range and co-tidal charts

This section describes the general characteristics of the tidal constituents in the Bay of Bengal and the characteristic features identified from the co-range and co-tidal charts in the shallow regions of the Bay of Bengal.

4.6.1 General features

The co-range and co-tidal charts for the semi-diurnal constituents M_2, S_2 and N_2 are presented in Figures 4.20, 4.21, and 4.22, respectively. The charts show a degenerate amphidromic system along the south eastern coast of Sri Lanka.

The M_2 amplitude tends to increase northward and north-eastward while entering the head bay and the Gulf of Martaban (Figure 4.20a). The distribution of M_2 tide in the Bay is affected by the presence of Andaman Island. In the central Bay, the M_2 tide propagates north-westward from the amphidromic point into the central bay and then attains a northward propagation in the head bay. In the

Andaman Sea, tide progresses north-eastward and enters into the Gulf of Martaban while in Malacca Strait, tide propagate southward (Figure 4.20b).

The amplitudes of the S_2 tide is about half of the M_2 tide and their variations in the Bay are similar to those of M_2 tide (Figure 4.21a). The S_2 tide propagates northward from the amphidromic point in the central Bay while in the Andaman Sea and Malacca Strait, similar to the M_2 tide, S_2 propagates north-eastward and southward, respectively (Figure 4.21b).

The amplitude of N_2 (Figure 4.22a) is low compared to the amplitudes of the other two semi-diurnal constituents. Though variations in N_2 amplitude in the central bay are less, local maxima occur in the head bay and in the Gulf of Martaban.

The co-range and co-tidal charts for K_1 (Figure 4.23) depict only small variations in the amplitude and phase across the Bay. The amphidromic system identified along the south eastern coast of Sri Lanka from the co-range and co-tidal charts of the semi-diurnal tides is found to be located along the open boundary for K_1 tide. The propagation of the K_1 tide, similar to M_2, is towards north-west and south-east in the central bay and Malacca Strait, respectively. The K_1 amplitude is found to be highest in the Malacca Strait unlike the semi-diurnal tides (M_2, S_2 and N_2), which have highest amplitudes in the Gulf of Martaban. These localized features are described in detail in the next section.

The co-range charts (Figure 4.24a) of O_1 show a gradual increase in amplitude towards the head bay, but the amplitudes are very small, the maximum amplitude being 10 cm in the Malacca Strait. The degenerate amphidromic system in the O_1 chart is located at the southern tip of Sri Lanka, around which tide progresses in the counter-clockwise direction. The O_1 tide propagates northward (Figure 4.24b) in the central western bay while in the Andaman Sea and inside the Malacca Strait, the propagation of the O_1 tide is similar to that of K_1 but the amplitudes are lower.

Figure 4.20 Distribution of amplitudes and phases of M_2 tide in the Bay of Bengal simulated using the tidal model showing a) co-range lines and b) co-tidal lines. Amplitudes are given in centimetres and phase '*G*' is given in degrees. The area marked as Detail 1, Detail 2 and Detail 3 are shown in Figure 4.26, Figure 4.28, and Figure 4.30, respectively.

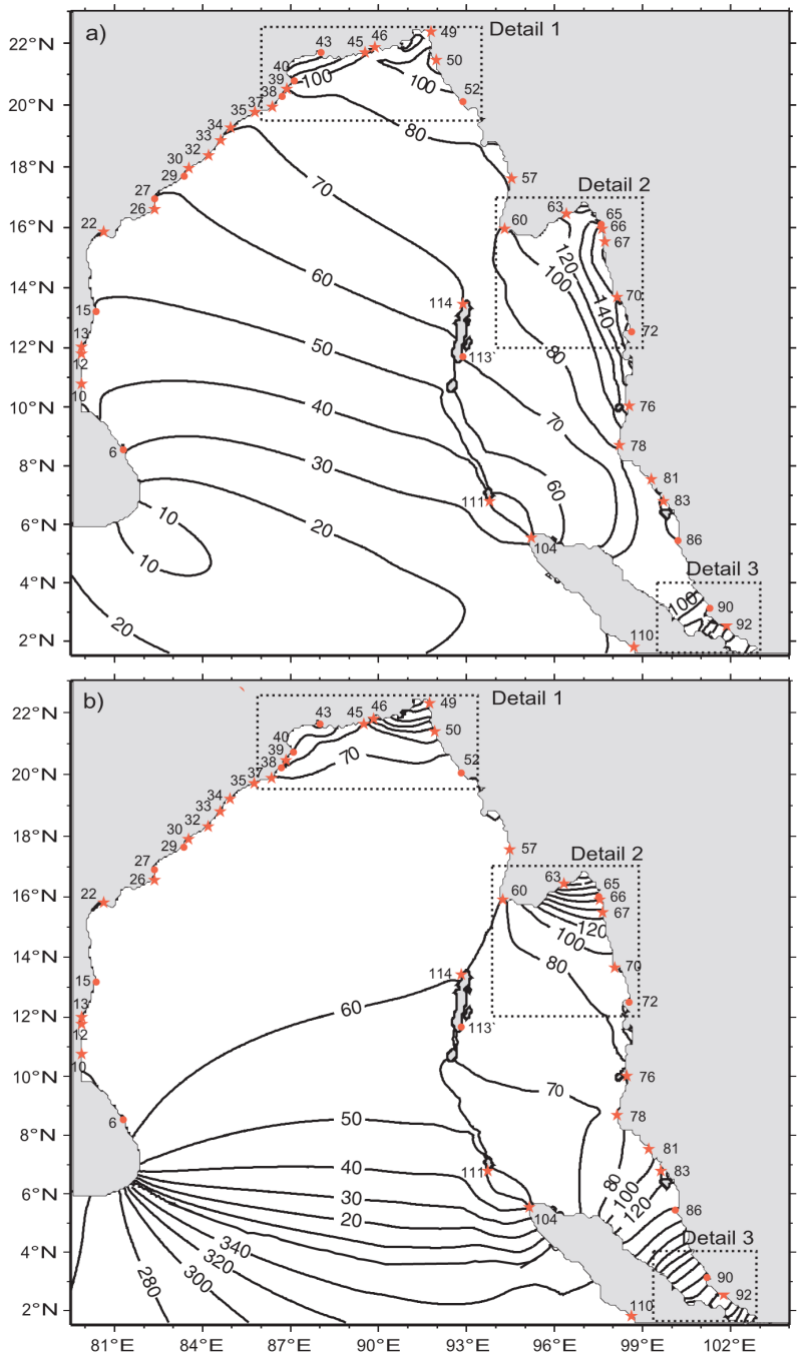

Figure 4.21 Same as Figure 4.20, but for S_2 tide. The area marked as Detail 1, Detail 2 and Detail 3 is shown in Figure 4.27, Figure 4.29, and Figure 4.31, respectively.

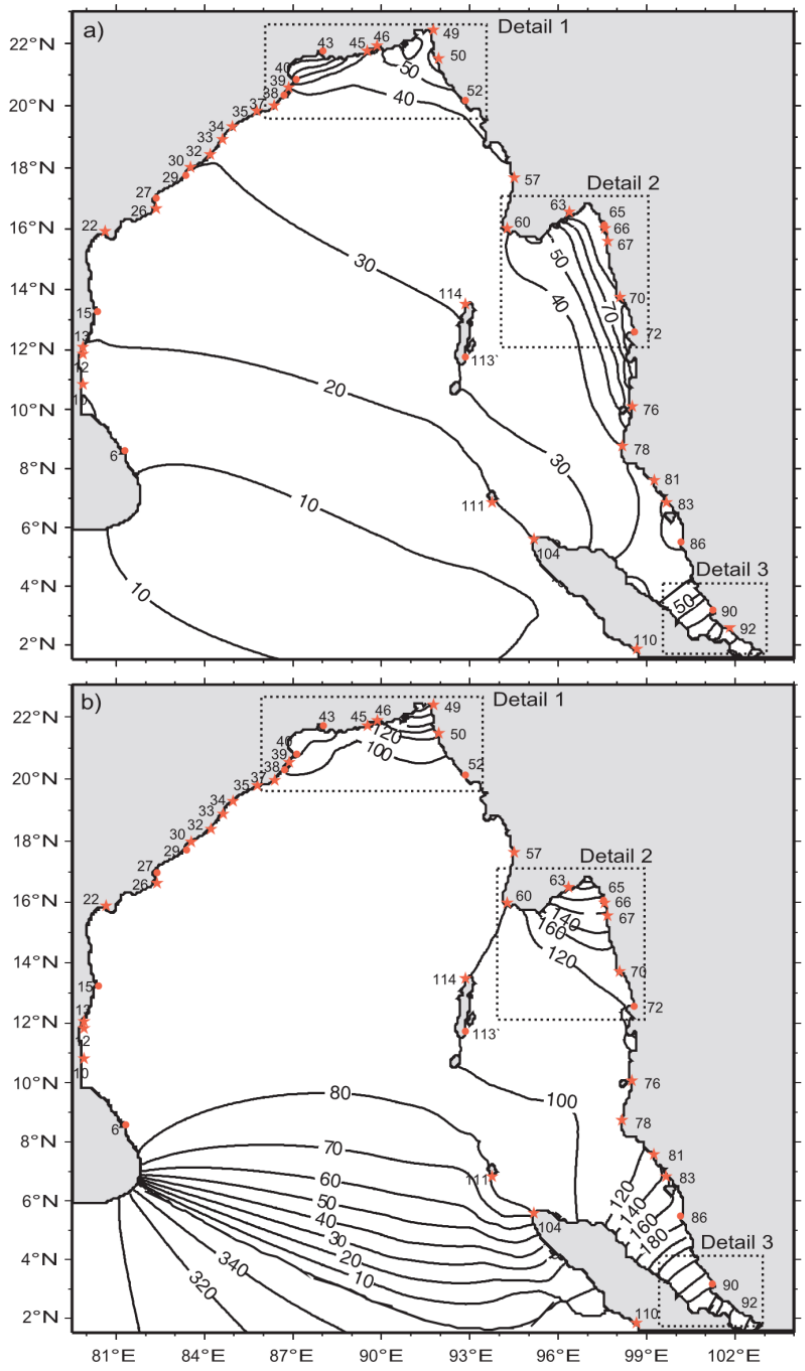

Figure 4.22 Same as Figure 4.20, but for N_2 tide.

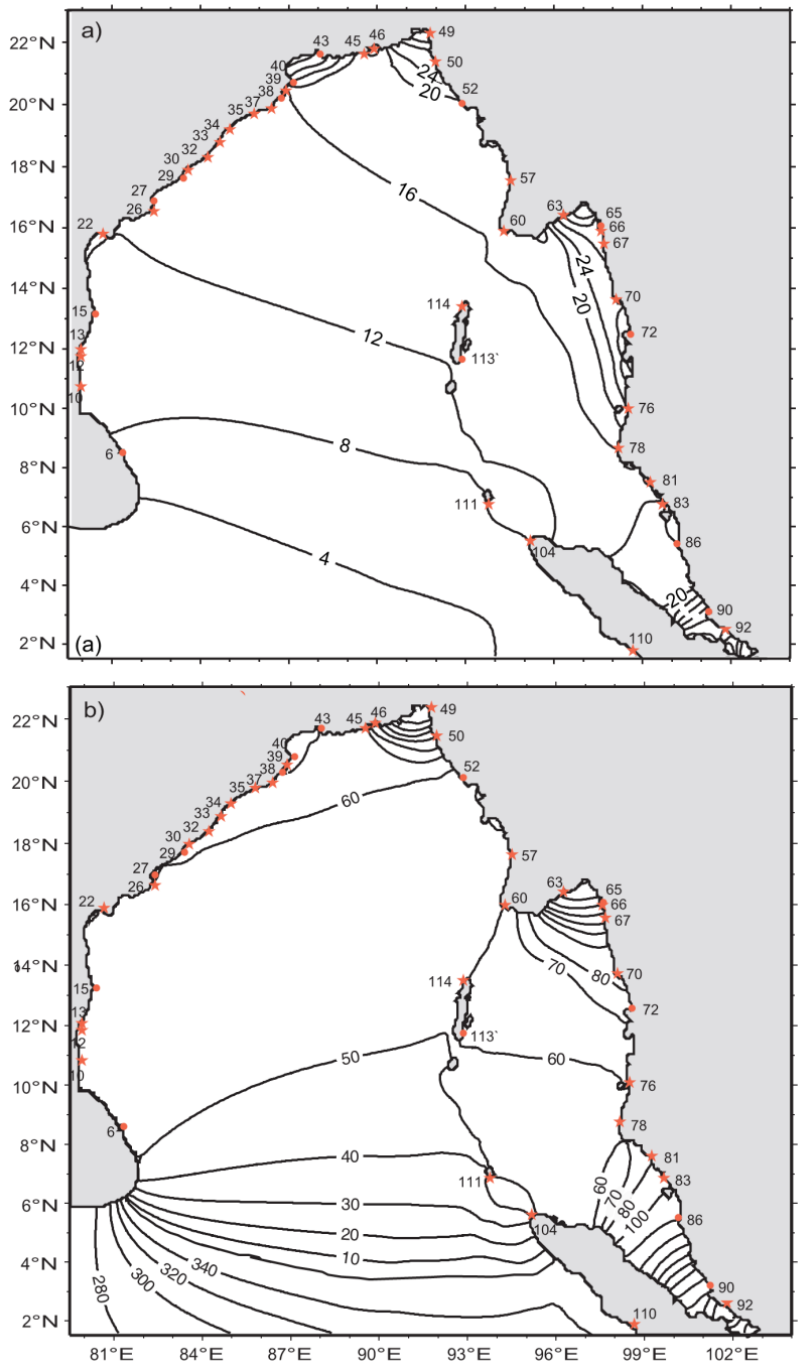

Figure 4.23 Same as Figure 4.20, but for K_1 tide. The area marked as Detail 3 is shown in Figure 4.32.

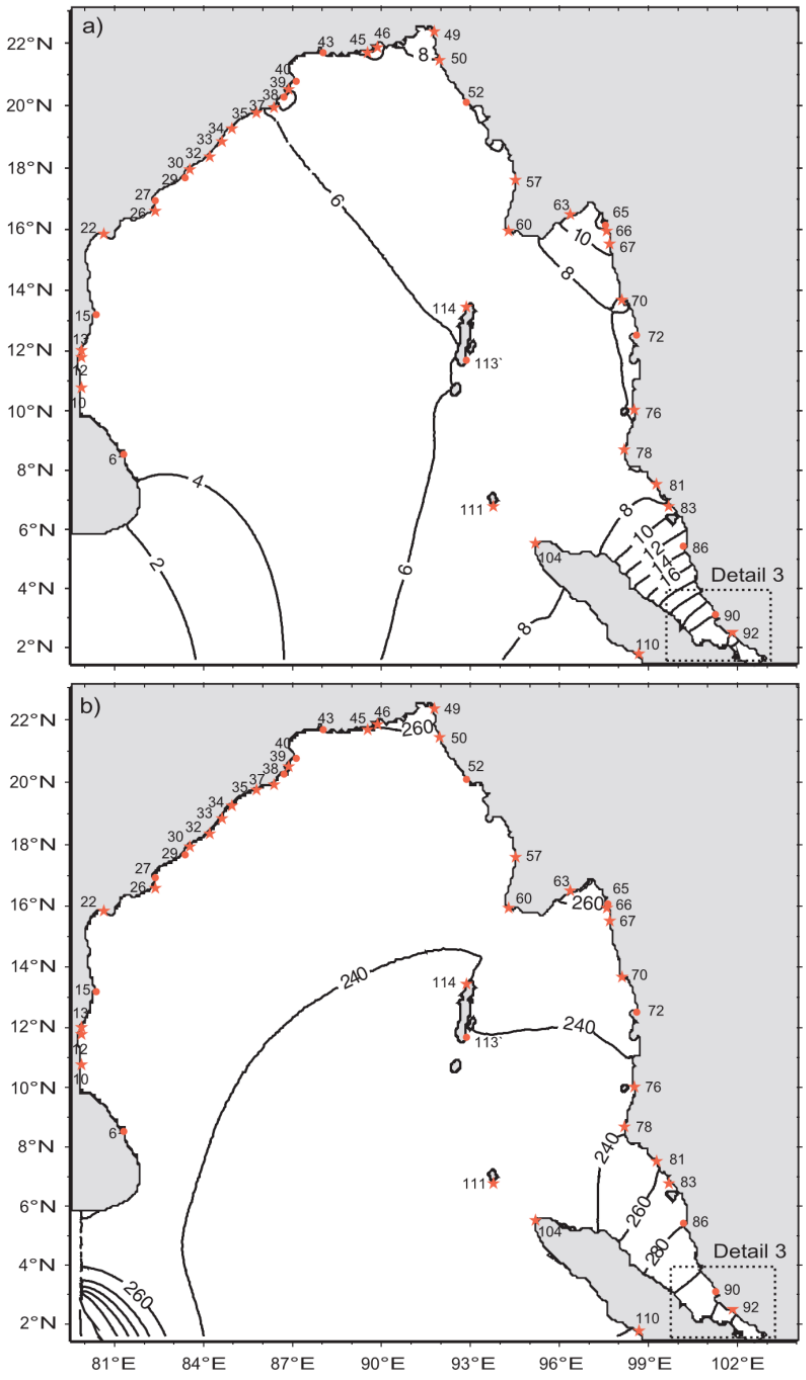

Figure 4.24 Same as Figure 4.20, but for O_1 tide.

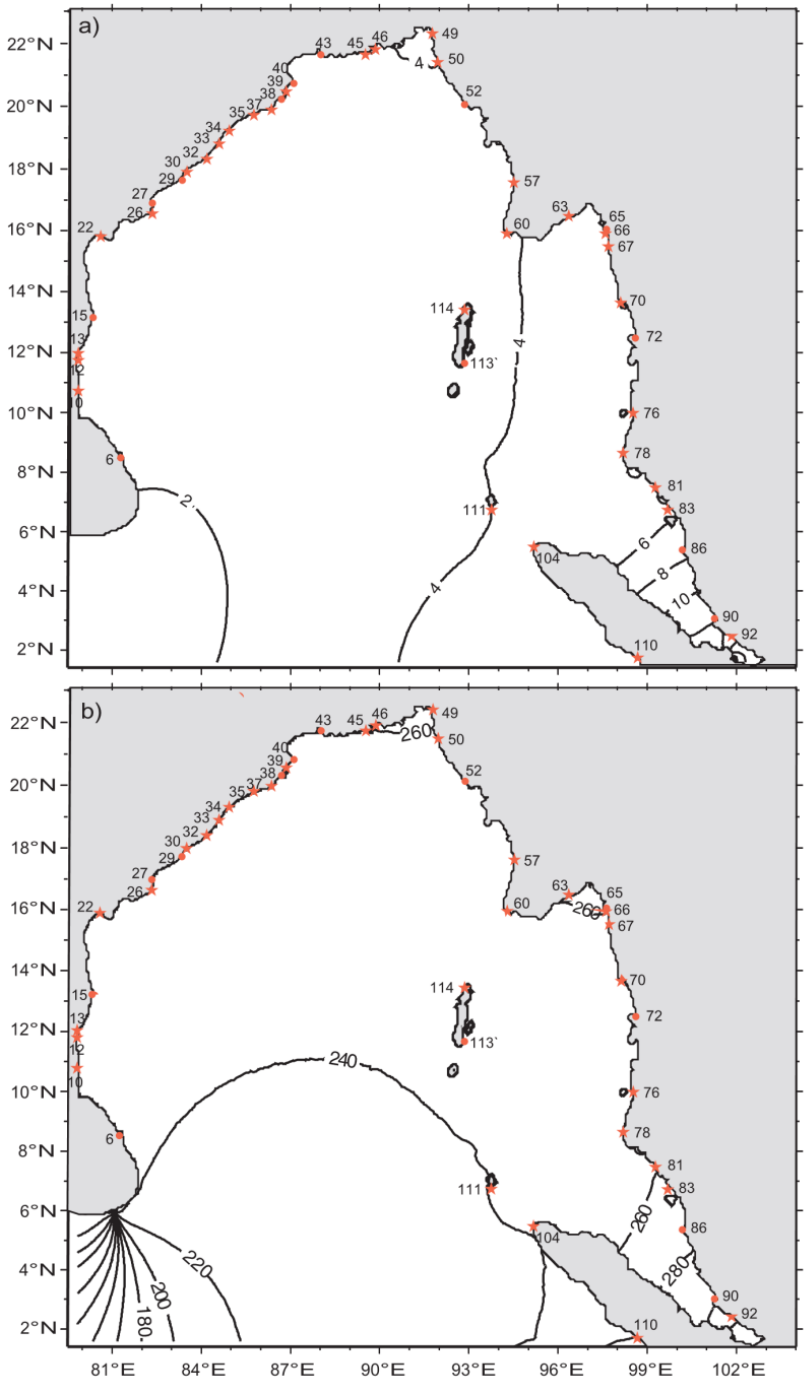

4.6.2 Characteristic features

Some characteristic features are observed in the distribution of the amplitudes and phases of tidal constituents in the shallow regions of Bay of Bengal such as the head bay, Gulf of Martaban and Malacca Strait. For semi-diurnal constituents, the detailed view of the co-tidal and co-range charts in these regions is shown in Figures 4.26 to 4.31 and for diurnal constituent, the detailed view is shown only for the Malacca Strait in Figure 4.32.

Head Bay

The amplitudes of the semi-diurnal tides in the head bay are found to be doubled in the head bay. The essential feature that could significantly contribute to the increase in the amplitudes of semi-diurnal tides in the head bay is its wide continental shelf, as analyzed in below section.

The effect of continental shelf is studied using the theory formulated by Clarke and Battisti [1981], referred to as CB theory in the text. They showed that semi-diurnal tides amplify on wide shelves in non-polar latitudes while the diurnal tides do not. They related the amplification of semi-diurnal tides to the proximity between shelf width and a parameter called shelf scale parameter (defined as $SP = \frac{g\alpha}{\omega^2 - f^2}$, where α is the bottom slope, f is the Coriolis parameter (described in Section 2.2) and ω is the angular frequency of the tidal constituent ($\omega = 2\pi/T$, T being the constituent period given in Table 1.1).

Murty and Henry [1983] also applied the CB theory at some stations in the head bay to study the effect of continental shelf width in the head bay. But, in the present study, we applied the theory to other regions along the western and eastern coast of Bay. We estimated the amplification factor (AF, the ratio of tidal amplitude at the coastal station to that at the shelf break) and the shelf scale parameter (SP) for M_2, S_2, N_2 and K_1 in order to investigate the effect of continental shelf width. Though SP and AF were extracted for all stations shown in Figure 4.7, except for the stations located far inside the head bay, Gulf of Martaban and Malacca Strait, Table 4.4 documents the values only for Standard

and Secondary Ports. Figure 4.25 shows the impact of the continental shelf width on the v ariability of AF of M_2, S_2, N_2 and K_1.

Amplification of semi-diurnal tides is not observed along the east coast of India; where the continental shelf is narrow (width less than 100 km). But in the head bay, continental shelf widens (approximately 200 km) and therefore semi-diurnal tides amplify in the region. For instance, the M_2, S_2 and N_2 tides attain an AF of 1.9, 2.5 and 1.9, respectively at Sagar Roads (Table 4.4), and an AF of 1.8, 2.3, and 1.7, respectively at Chandipur, which are located on western part of head bay. The continental shelf at Sagar Roads and Chandipur is as wide as 195 and 160 km, respectively which are relatively closer to the value of SP as seen from Table 4.4. The diurnal tide K_1 amplifies only marginally in the western part of the head bay (AF=1.1 at Sagar Roads). This is in agreement to CB theory. However at the locations of Pussur River and Tiger Point, the amplitudes of semi-diurnal tides are not relatively high (for M_2, AF = 1.2 at both stations), which could be due to relatively narrow shelf (approximately 100 km), as seen from Table 4.4.

In the eastern head bay, the amplification of semi-diurnal tides is relatively less (AF at Chittagong is 1.5, 1.6 and 1.9, respectively), but in this region the diurnal tide K_1 is observed to amplify equally as that of semi-diurnal tides as indicated by AF of 1.5 at Chittagong. Therefore, in addition to the wide continental shelf (as assessed from Figure 4.8), the geometrical configuration of the coastline in the north-eastern head bay could also be responsible for the amplification of both semi-diurnal and diurnal tides in the region.

The detailed examination of the M_2 and S_2 charts (Figures 4.26b and 4.27b, respectively) revealed the presence of a degenerate amphidromic point near to Pussur Station. Another degenerate amphidromic point is identified at the north eastern end of head bay (Figures 4.26c and 4.27c).

Gulf of Martaban

The co-range charts of semi-diurnal constituents (Figures 4.20, 4.21, and 4.22) the highest amplification of semi-diurnal tides (M_2, S_2, and N_2) is found to be in the Gulf of Martaban; the AF being 2.4, 2.8, and 2.6 at Amherst (Table 4.4). The

amplification of M_2 and S_2 are found to be higher (by 23% and 29%, respectively) along the eastern coast of Gulf of Martaban as compared to the western coast. The diurnal tide K_1 amplifies significantly (AF=1.7) in the Gulf of Martaban. The converging effect of the funnel shaped gulf, shallow bathymetry and the wide continental shelf could contribute to the amplification, consequently producing very high tidal amplitudes in the area.

Southern part of Myanmar coast

One of the interesting features observed in the distribution of semi-diurnal co-range and co-tidal charts is the amplification of M_2, S_2, and N_2 along the southern coast of Myanmar, with amplitudes increasing southward and attaining relatively higher values near Sinbyubyin (AF = 1.8, 1.9 and 1.4, respectively) and Mergui (AF = 2.0, 2.2 and 1.6, respectively) than those at Akyab and Gya Bay (AF = 1.1 and 1.0 at 2 stations, respectively for M_2, S_2, and N_2), which are located on the northern Myanmar coast. The coastline of Myanmar is characterized by a wide continental shelf, especially at the southern coast, where the shelf is as wide as 220 km. It is evident from Table 4.4 that the shelf scale parameter (SP), estimated for stations along southern Myanmar coast (Stations 68 to 72), is in close proximity to the shelf width, which signifies the amplification of semi-diurnal tides. The diurnal tide K_1 amplifies only marginally at these stations in compliance with the theory of CB theory. Figure 4.25 also depicts that the variations in the amplitudes of K_1 tide is very small with the variation in shelf width along the coast of Bay of Bengal.

Table 4.4 The shelf scale parameter (SP) and the amplification factor (AF - ratio of amplitude at the coastal station to that at the shelf break) estimated for the tidal constituents M_2, S_2, N_2 and K_1 at stations corresponding to the Standard and Secondary Ports. The shelf width estimated at each of the stations, excluding the stations located inside the Gulf of Martaban and Malacca Strait, is also listed.

St No	Station Name	Shelf width (km)	M_2		S_2		N_2		K_1	
			SP	AF	SP	AF	SP	AF	SP	AF
6	Trincomalee	32	1565	1.04	1458	1.04	1627	1.01	6222	1.04
10	Nagapattinam	84	1346	1.03	1253	1.03	1400	1.01	5584	1.03
11	Porto Nova	29	1500	0.99	1400	0.98	1500	0.99	6000	0.99
12	Cudallore	57	1394	1.00	1298	1.00	1451	1.00	5925	1.00
13	Pondicherry	71	1473	1.00	1371	1.00	1533	1.00	6300	1.00
15	Chennai	32	1830	1.01	1701	1.01	1905	1.00	8086	1.00
16	Pulicat	30	2470	1.01	2300	1.01	2576	1.00	11020	1.00
18	Gudur	40	2730	1.01	2539	1.03	2845	1.00	12432	1.00
19	Nellore	20	2000	1.01	585	1.02	5900	1.00	26221	1.00
20	Kavali	40	2810	1.01	2610	0.93	2928	1.00	13168	0.99
22	Surya Lanka	37	450	1.13	418	1.14	1238	1.07	2186	1.01
24	Machilipatnam	100	1192	1.02	1106	1.02	1242	1.03	5871	0.98
26	Sacromental	30	2000	0.99	2000	0.99	652	1.00	20591	0.99
27	Kakinad	50	1813	1.02	1681	1.02	1890	1.00	9231	1.02
29	Visakhapatnam	49	1153	1.00	1069	1.00	1203	1.00	6093	1.00
30	Bhimunipatnam	58	1313	1.01	1216	1.01	1370	1.00	7027	1.01
32	Kalingaptnam	44	1325	1.00	1227	1.00	1382	1.00	7253	0.99
33	Baruva	55	1046	1.01	969	1.01	1092	1.00	5896	1.00
34	Gopalpur	83	1271	1.01	1176	1.01	1327	1.00	7345	1.00
35	Chilka Mouth	92	1049	0.99	971	0.99	1096	0.99	6267	1.00
36	Puri	85	1517	0.99	1403	0.99	1584	0.99	9113	0.99
37	Devi River	34	1887	0.99	1745	0.99	1971	0.98	11398	1.00
38	Paradip	41	569	0.93	526	0.90	594	0.88	3516	0.90

Table 4.4 Continued

St No	Station Name	Shelf width	M_2		S_2		N_2		K_1	
			SP	AF	SP	AF	SP	AF	SP	AF
39	False Point	65	446	1.06	412	1.09	466	1.08	2809	1.01
40	Shortt Island	104	445	1.21	411	1.31	465	1.28	2858	1.05
41	Chandipur	160	840	1.78	776	2.33	878	1.72	5658	1.07
43	Sagar Roads	195	614	1.93	567	2.53	642	1.88	4257	1.13
45	Pussur River	100	677	1.25	625	1.27	708	1.04	4690	0.93
46	Tiger Point	110	657	1.21	606	1.28	687	0.99	4619	0.94
49	Chittagong	-	254	1.54	235	1.65	-	1.89	-	1.57
50	Cox Bazaar	-	232	1.32	214	1.70	-	2.00	-	1.19
52	Akyab	81	434	1.11	401	1.13	453	1.09	2651	0.99
57	Gya bay	56	2000	1.02	2000	1.02	2403	1.00	12117	1.00
60	Basien River	185	796	1.08	739	1.07	581	1.12	3880	1.10
63	Elephant	-	-	1.95	-	2.13	-	2.57	-	1.45
65	Amherst	-	-	2.41	-	2.71	-	2.21	-	1.64
66	Double Island	-	-	2.25	-	2.76	-	2.37	-	1.70
68	Bentick Sound	-	-	2.33	-	2.70	-	2.13	-	1.61
70	Sinbyubyin	204	509	1.76	473	1.85	530	1.38	2284	1.10
72	Mergui	220	386	2.00	359	2.25	402	1.63	1674	1.10
76	Pulua basin	145	711	1.51	662	1.56	739	1.32	2903	1.01
78	Klong	88	639	1.10	596	1.10	665	1.03	2547	1.01
81	KoHyaKya	157	303	1.34	282	1.41	315	1.12	1184	1.03
83	Pulua Lela	145	316	1.60	294	1.86	328	1.43	1222	1.24
86	Pinang	-	-	1.68	-	1.94	-	1.40	-	1.57
90	Pelabuhan Kl.	-	-	2.40	-	2.45	-	1.68	-	2.39
110	Sibolga	-	-	1.11	-	1.11	-	1.00	-	1.01

Figure 4.25 The amplification factor (AF) of M_2, S_2, N_2 and K_1 tide plotted against the shelf width. The stations far insde the head bay, Gulf of Martaban and Malacca Strait have been excluded.

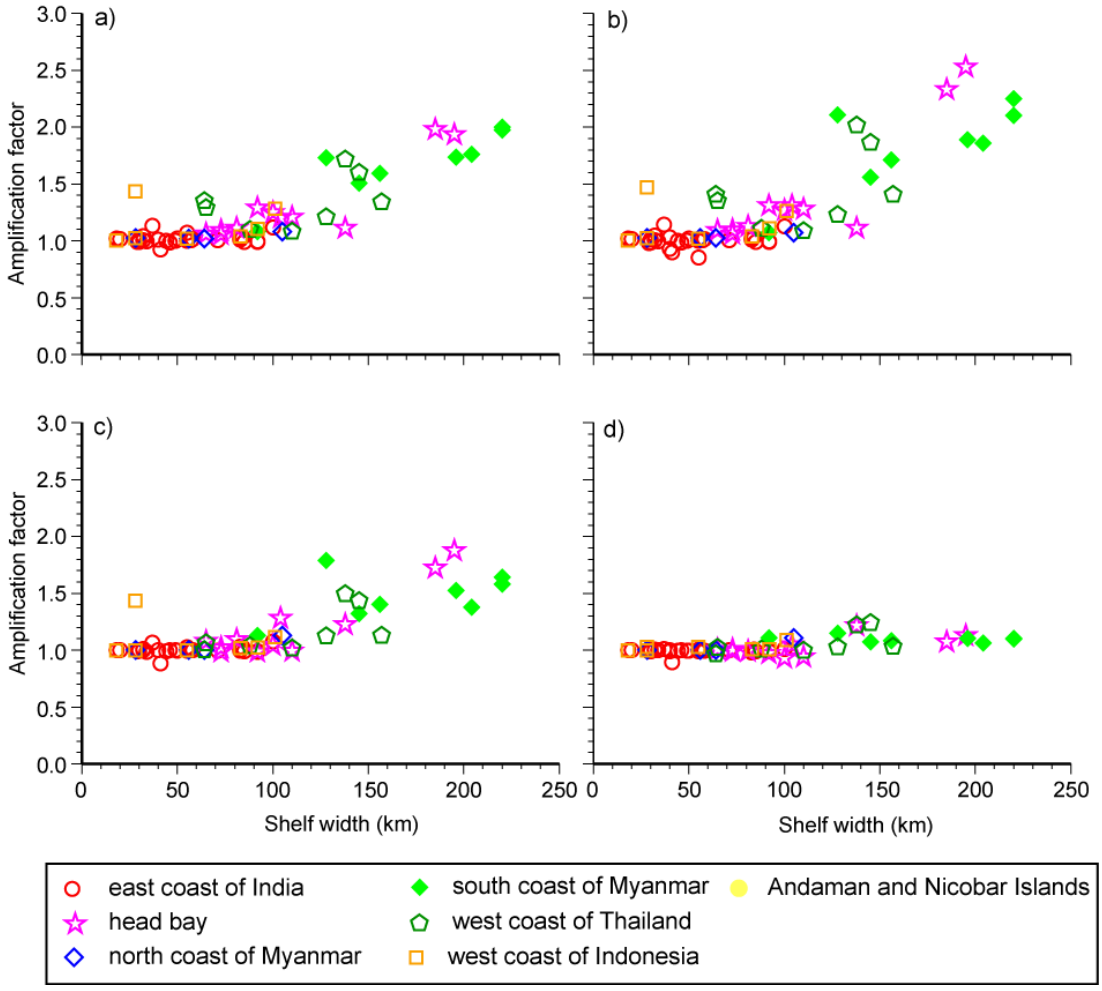

Figure 4.26 Detailed view of co-range and co-tidal lines of M_2 tide in the a) head bay, showing the degenerate amphidromic points b) along the western and c) north-eastern coast of Bangladesh.

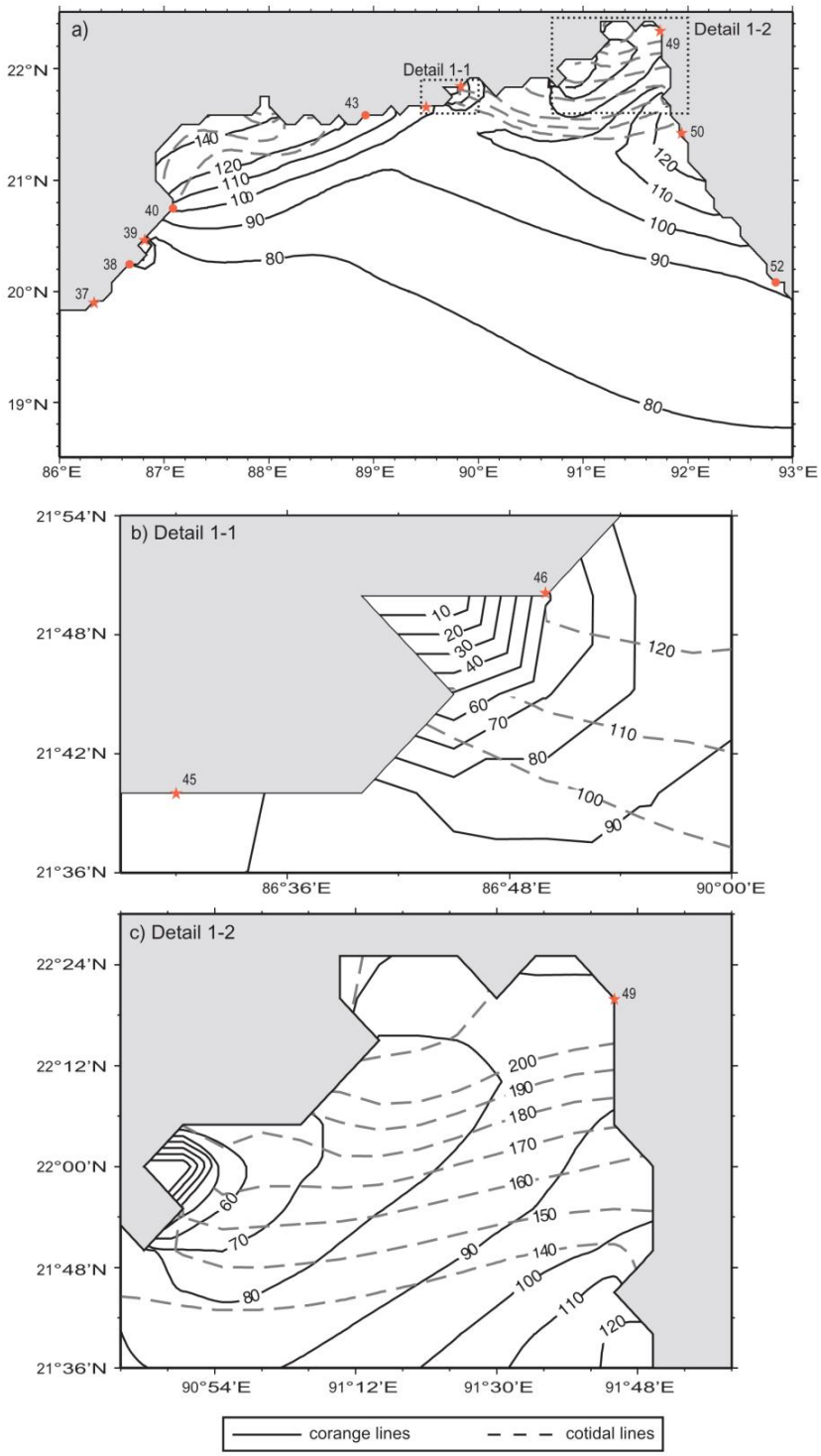

Figure 4.27 Detailed view of co-range and co-tidal lines of S_2 tide in the a) head bay, showing the degenerate amphidromic points b) along the western and c) north-eastern coast of Bangladesh..

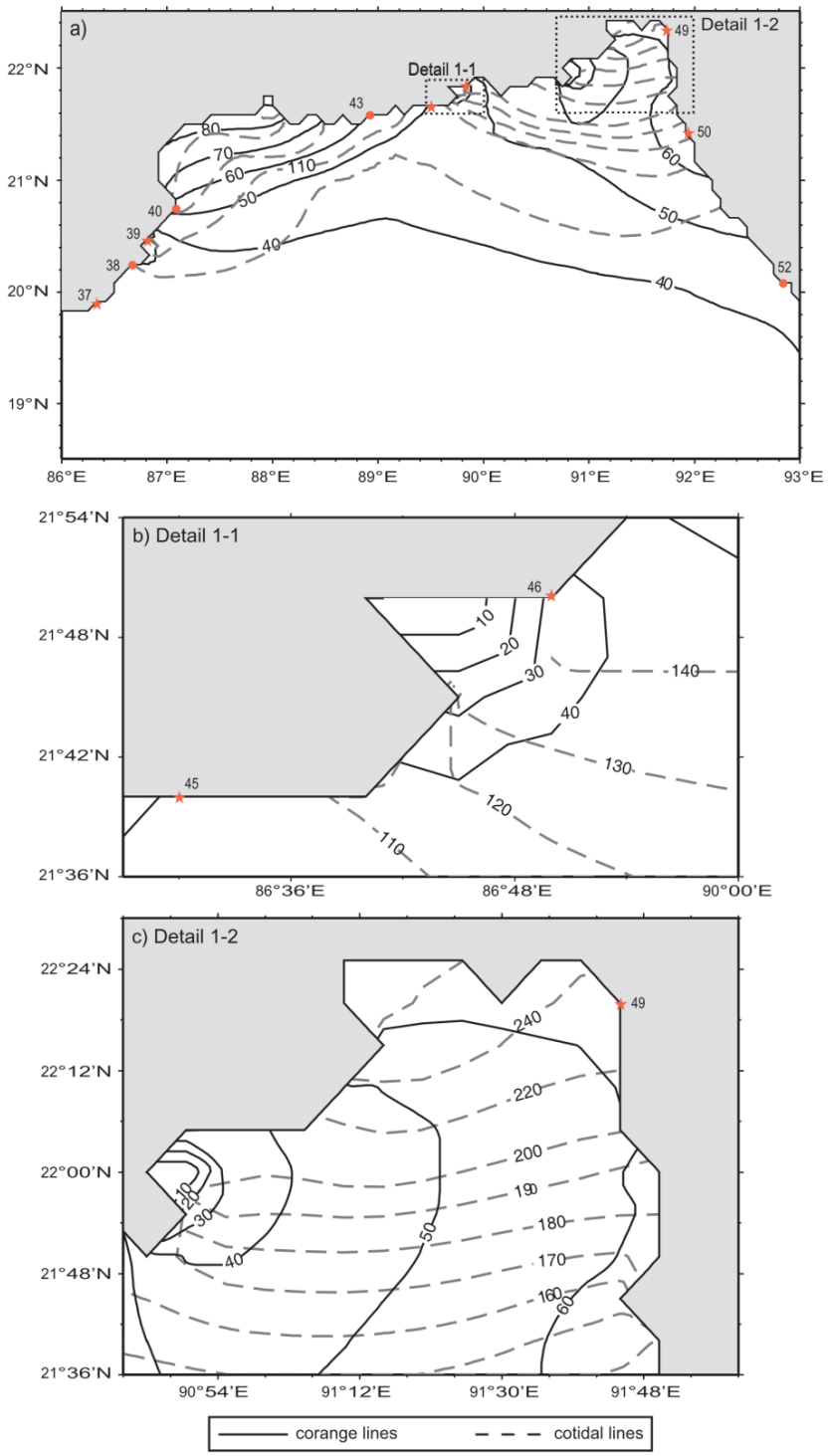

Figure 4.28 Detailed view of M_2 tidal chart showing the co-range and co-tidal lines for the Gulf of Martaban and along the southern coast of Myanmar.

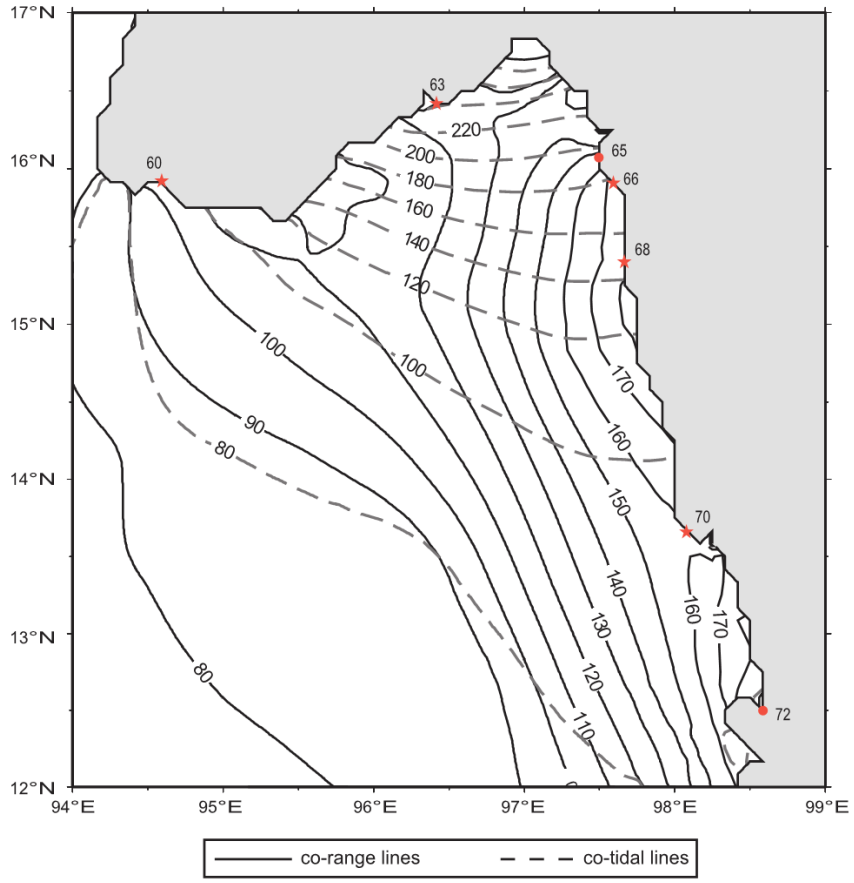

Figure 4.29 Same as Figure 4.28, but for S_2 tide.

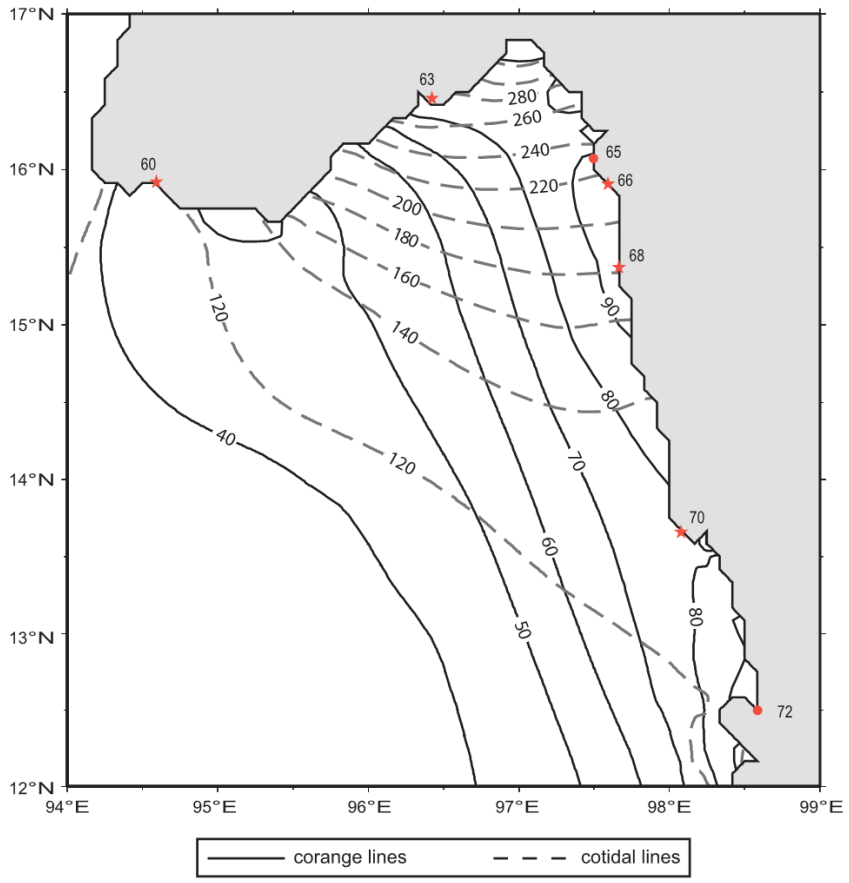

Malacca Strait

The semi-diurnal tides (M_2, S_2, N_2) while entering the Malacca Strait from the northern end show an increase in amplitude towards the southern region with maximum amplitude obtained at about 2.5°N (i.e. at Pelabuhan Klang, the amplitudes are as high as 130, 60 and 30 cm, respectively).

While analysing the co-range and co-tidal charts for the diurnal tide K_1 (Figure 4.32), we found that along the coast of Bay of Bengal, K_1 attains maximum amplitudes (approximately 20 cm at Pelabuhan Klang) in the Malacca Strait. Even the amplitudes of O_1 tide increases in the Malacca Strait (Figure 4.24), attaining a significant value of 12 cm at Pelabuhan Klang. It is probably the funnel shaped geometrical configuration and shallow bathymetry (depths of average 50 m) of the Malacca Strait, which are favourable for the increase in amplitudes of both semi-diurnal and diurnal tides.

However, the amplitudes of the semi-diurnal and diurnal tides are found to decrease south of 2.5°N. The amplitude of M_2 tide decreases from 2.5°N (120 cm) to 2°N (60 cm), and then again increases towards the southern open boundary. The co-range and the co-tidal pattern for M_2 tide shown in Figure 4.30 are similar to the distribution obtained by Rizal [2000]. The decrease in the amplitude of M_2 tide is due to the presence of a virtual amphidromic point. The position of the virtual amphidromic point, as depicted from Figure 4.30, could be located somewhere far inland to the north-east, which is in agreement with the findings of the Rizal [2002]. The distribution of amplitudes of S_2 and N_2 and diurnal tide K_1 tide also shows signatures of virtual amphidromic point. A fine resolution tidal model for Malacca Strait is needed to confirm the presence of virtual amphidromic point.

Figure 4.30 Detail view of tidal chart of M_2 tidal chart showing co-range and co-phase lines in Malacca Strait.

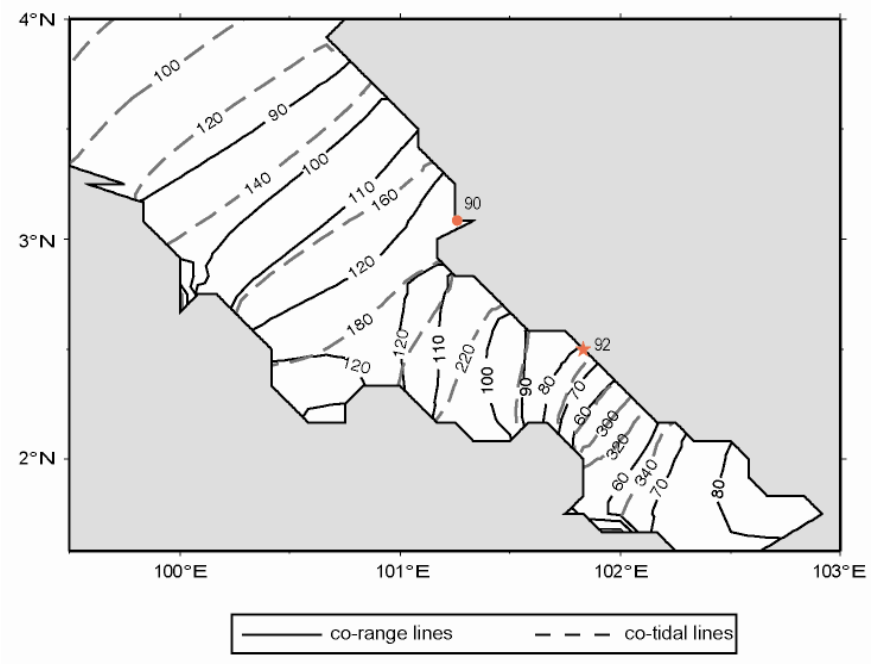

Figure 4.31 Same as Figure 4.30, but for S_2 tide.

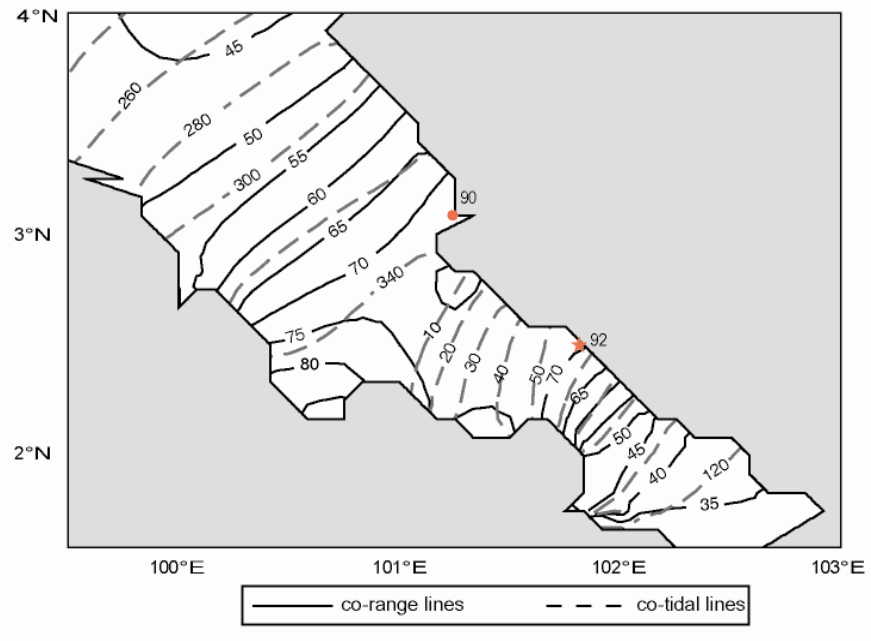

Figure 4.32 Same as Figure 4.30, but for K_1 tide.

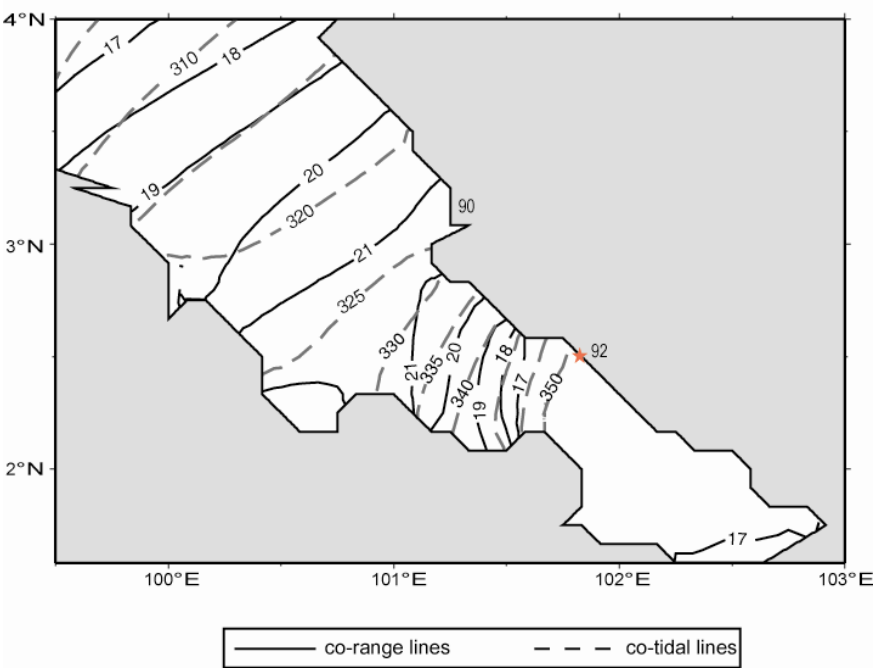

There is a difference in the pattern of the amphidromic points found in the eastern head bay and that in the Malacca Strait. The degenerate amphidromic point observed in the head bay is easily identifiable whereas the Malacca Strait has a purely virtual amphidromic point. This is in accordance to the conclusion of Rizal [2002] who showed that the displacement of the amphidromic systems away from the central axis decreases with the increase in the latitude and therefore the probability of occurrence of virtual amphidromes in higher latitudes is less. It is noted that Rizal and Sundermann [1994] and Rizal [2000] simulated the semi-diurnal constituent M_2 in the Malacca Strait and explained the features exhibited by the M_2 tide in terms of virtual amphidromic point. However, these studies lacked the availability of tidal information along the north western open boundary. The present work, which has the advantage of accurate open boundary conditions, is assessed to provide more accurate results.

4.7 Conclusions

A 2D vertically integrated model, developed by Unnikrishnan et al. [1999], was used for the simulation of tides in the Bay of Bengal. The numerical model was thoroughly validated by comparing the simulated composite tides as well as the model derived tidal constituents with observations at different stations covering the entire coastline. The simulated tidal elevations at Paradip, Visakhapatnam and Chennai for a period of 30 days agreed fairly well with the observed tide gauge data, with an RMSE less than 7.5 cm. A reasonable agreement was obtained between the model derived and the observed amplitude and phases of the semi-diurnal and diurnal constituents with RMSE less than 7 cm and 9.5°. It is concluded from the RMS misfit (ORM), being less than 9 cm for all the model derived constituents, that despite the differences between the amplitudes and phases of model derived and observed constituents at a few stations, the model has the capability of reproducing the tidal regime in the area and has sufficient fine grid to capture the near shore tidal variations.

The tidal model was used to simulate each of the major semi-diurnal and diurnal constituents separately in order to develop co-tidal and co-range charts for the constituents M_2, S_2, N_2, K_1 and O_1 for the Bay of Bengal. The characteristic of the tidal constituents in Bay of Bengal and the characteristic features observed in the shallow regions such as head bay, Gulf of Martaban and Malacca Strait were analyzed and illustrated elaborately.

The semi-diurnal tides (M_2, S_2, and N_2) are found to amplify nearly twice in the head bay, along the southern coast of Myanmar and in the Gulf of Martaban. The diurnal constituent K_1 amplifies significantly only in the north eastern end of the head bay and in the Gulf of Martaban. The continental shelf in the head bay and along the southern coast of Myanmar is about 200 km wide and the amplitudes of semi-diurnal tides are doubled in these regions while the diurnal tides amplify only marginally, which is consistent with CB theory. In the north eastern end of the head bay and the Gulf of Martaban, the geometrical configuration of the coastline, in addition to the wide continental shelf, could also contribute to the amplification of both semi-diurnal and diurnal constituents. In

the Malacca Strait, the amplitudes of both semi-diurnal and diurnal tides are found to increase gradually from the northern end to the 2.5°N. The highest amplitudes of diurnal tides, K_1 and O_1, are observed in the Malacca Strait.

The co-tidal and co-range charts of M_2 and S_2 tidal constituents show the presence of two degenerate amphidromic points in the head bay; one in the central part and other in the north eastern end of the head bay. A virtual amphidromic point for M_2 is identified in the Malacca Strait.

The study on the propagation of tides and the distribution of amplitudes and phases of semi-diurnal and diurnal constituents in the Bay of Bengal has been scarce. Therefore, the present study has focussed on the identification of characteristics features in the distribution of major tidal constituents in the Bay of Bengal, especially in shallow regions such as head bay, Gulf of Martaban and Malacca Strait.

Chapter 5

Simulation of storm surges in the Bay of Bengal

5.1 Introduction

As a first step towards increasing the accuracy of storm surge simulation, a 2D model was developed to simulate the tides in the Bay of Bengal as described in Chapter 4. The validation of the tidal model results showed that the model was able to capture the observed tidal characteristics in the Bay of Bengal. Now that the accuracy of the tidal model is evaluated, we modified the model to simulate the storm surges (hereafter referred to as storm surge model) caused due to different low pressure systems that developed in the Bay during the past years.

The meteorological forcing for the storm surge model was obtained from the cyclone model of Holland using the data available for 136 low pressure systems (LPS) that occurred during 1974-2000 in the Bay of Bengal. The storm surge model was driven by the combined effect of tides and meteorological parameters to get the total water levels and with tides alone to compute the surge component as a difference between the elevations of two simulations. The annual maxima of sea levels, extracted from the simulations, were fitted with Gumbel distribution using r-largest annual maxima method to estimate the return periods and return levels of extreme events at 26 stations along the east coast of India. Though the model domain covered the entire Bay of Bengal, the return levels were evaluated only along the east coast of India. This work is documented in Sindhu and Unnikrishnan [2012].

Similar work has been carried out by Jain et al. [2010], who estimated the expected total water level for each coastal district of the maritime states along the east coast of India. However, the methodology followed by Jain et al. [2010] is slightly different from the present study as they had carried out storm surge simulations for

synthetic cyclonic events developed from statistically projected cyclone intensities based on the analysis of historical data. The major improvement of the present study over Jain et al. [2010] is the inclusion of the meteorological and tidal forcing simultaneously in the model in order to allow for tide-surge interaction. The non-linear interaction between tides and surge and its substantial impact on the resultant total sea level have been studied by Horsburgh and Wilson [2007], Butler et al. [2007], Johns et al. [1985] and emphasized in several earlier works as a step towards improvement for accurate assessment of total water level.

A description of the models used to generate cyclones and storm surges are given in Sections 5.2.1 and 5.2.2 respectively. The model validation using the observed hourly sea level is described in Section 5.3. The return levels of extreme sea levels are discussed in Section 5.4. The results of the study are summarized in Section 5.5.

5.2 Data and methodology

The meteorological parameters represented by wind field and core pressure associated with a cyclone and tides are the major input to drive the storm surge model. The tidal elevations were obtained from FES2004 global tidal dataset, as defined in Chapter 4 while the wind fields and Mean Sea Level pressure (MSLP) fields were generated using Holland cyclone model. The schematization of Holland cyclone model and storm surge model and the input data required to drive these models are described in the following sections.

5.2.1 Holland cyclone model

The large pressure drop at the core and the strong wind field around the core are the prominent feature of a tropical cyclone; the former produces surge in the deeper part of the bay, while the latter acting on the continental shelf produces the major and disastrous surge. Accordingly, it becomes essential to provide accurate wind and pressure field as the input to the storm surge model.

The MSLP is determined by using the model of Holland [1980] following Flather [1994] as

$$p = p_c + (p_n - p_c)exp[-(r_m/r)^b] \quad (5.1)$$

where, p is the atmospheric pressure at radius r, p_c is the core pressure, p_n (1010 hPa) is the ambient pressure, r_m is the radius of maximum winds and b is a scaling parameter that defines the shape of a cyclone with values ranging from 1 to 2.5. The parameter $(p_n - p_c)$ gives the pressure drop at the core of the cyclone.

Empirically b is defined as [Hubbert et al., 1991; Tang et al., 1997]

$$b = 1.5 + (980 - p_c)/120 \quad (5.2)$$

where p_c is in hPa.

The symmetrical wind profile is estimated [Holland, 1980] from the gradient wind equation as given below, from which the components of wind stress, w_x and w_y are derived

$$V_g = \left\{ \frac{b\left(\frac{r_m}{r}\right)^b (p_n - p_c)exp\left[\left(\frac{r_m}{t}\right)^b\right]}{\rho_a} + \frac{r^2 f^2}{4} \right\}^{1/2} - \frac{r|f|}{2} \quad (5.3)$$

where ρ_a is the density of air and $f = 2\omega sin\varphi$ is the Coriolis parameter (as defin ed in Section 2.2). The maximum winds occur when $\left(\frac{r_m}{r} \cong 1\right)$, which implies

$$V_{max} = \left\{ \frac{b(p_n - p_c)}{e\rho_a} \right\}^{1/2} \quad (5.4)$$

5.2.2 Storm surge model

The storm surge model was developed from the tidal model by incorporating the stress terms and the MSLP fields in the vertically integrated equations of momentum (Equations (2.2) and (2.3)) described in Section 2.2. Therefore, the equations of continuity and the momentum equations in the x and y directions are as follows:

$$\frac{\partial \eta}{\partial t} + \frac{\partial U}{\partial x} + \frac{\partial V}{\partial y} = 0 \quad (5.5)$$

$$\frac{\partial U}{\partial t}+\frac{\partial}{\partial x}(uU)+\frac{\partial}{\partial y}(vU)-fV\ =-g(h+\eta)\frac{\partial \eta}{\partial x}-\frac{1}{\rho}\frac{\partial p}{\partial x}+\frac{\tau_{sx}}{\rho}$$

$$-\frac{C_d U\sqrt{U^2+V^2}}{(h+\eta)^2}+A_H\nabla^2 U \qquad (5.6)$$

$$\frac{\partial V}{\partial t}+\frac{\partial}{\partial x}(uV)+\frac{\partial}{\partial y}(vV)+fU=-g(h+\eta)\frac{\partial \eta}{\partial y}-\frac{1}{\rho}\frac{\partial p}{\partial y}+\frac{\tau_{sy}}{\rho}$$

$$-\frac{C_d V\sqrt{U^2+V^2}}{(h+\eta)^2}+A_H\nabla^2 V \qquad (5.7)$$

The symbols in Equations (5.5), (5.6), and (5.7) have been defined in detail in Section 2.2, except $\bar{\tau}_s$, the surface stress which is parameterized as a quadratic of the surface wind velocity ($\bar{W}$) as

$$\bar{\tau}_s = k\rho_a \bar{W}|\bar{W}|;\ \bar{W}=\sqrt{w_x^2+w_y^2} \qquad (5.8)$$

where, k is the surface drag coefficient and ρ_a is the air density. The drag coefficient k in Equation (5.8) is given as $k \times 10^3 = 0.8 + 0.0065\bar{W}$ suggested by Wu [1982], taking into account the increase in sea surface roughness with increase in wind speed.

The Equations (5.5), (5.6), and (5.7) are transformed into finite difference form as described in Section 2.4.

In addition to the governing equations, the open boundary is modified by applying a radiation type condition [Heaps, 1973], shown by Equations (5.9) and (5.10).

Along southern boundary:

$$v+\left(\frac{g}{h}\right)^{\frac{1}{2}}\eta=0 \qquad (5.9)$$

Along western boundary:

$$u + \left(\frac{g}{h}\right)^{\frac{1}{2}} \eta = 0 \tag{5.10}$$

Unnikrishnan et al. [2006, 2011] used a similar code for the simulation of surges driven by the wind field and surface pressure fields obtained from regional climate models (HadRM2 and PRECIS, respectively).

5.2.3 Cyclone data for Holland model

The inputs required for the generation of cyclone using Holland model are the radius of maximum winds, core pressure and the position of the core of the cyclone. Holland [1980, Table 2] showed that the mean errors and maximum errors associated with MSLP fields obtained using Equation (5.1) decreases with increase in radius of maximum winds and has minimal value at 100 km and 40-60 km. Experiments with different radii of maximum wind showed that defining 50 km as the radius of maximum winds in the cyclone model of Holland produced a more realistic surge simulation results.

For the present study, a set of 136 low pressure systems (LPS), identified during the period 1974-2000, were used. National Institute of Oceanography [2004] examined the hourly tide gauge data of 27 years (1974-2000) at Paradip, Visakhapatnam and Chennai for storm surge events and identified the associated meteorological events based on the information from the Indian Daily Weather Report and Mausam, published by the Indian Meteorological Department. The report gave a detailed account of the position and the pressure of the cyclone core for each LPS event at each day of its development till the landfall for the events identified during 1974-1988. The information about the cyclone tracks for the events that occurred during 1989-2000 were available in-house, a brief summary of which has been provided in the report.

A total of 136 cyclonic events were identified during the past 27 years (1974-2000), which were analyzed for their intensities and classified, as per Table 1.3 into Super Cyclonic Storms (SCS), Cyclone Storm (CS), Deep Depression

(DD) and Depression (D). Among the 136 LPS events identified, 30 were D, 41 DD, 26 CS, and 37 SCS. It is depicted from the monthly frequency distribution of the events (Figure 5.1) that highest frequency of CS (25%) and SCS systems (49%) occur in the month of November. Cyclone formation is found to be prominent during the monsoon and post monsoon months with rare formations in the months from January to April. Figure 5.2 shows that the cyclones with core pressure 990-995 hPa, which corresponded to a wind speed of 25 – 30 knots, had the highest frequency of occurrence in the considered period.

Figure 5.1 Monthly frequencies of cyclones classified as Depression (D), Deep Depression (DD), Cyclone Storm (CS) and Super Cyclonic Storms (SCS) for the period 1974 - 2000. Data Source: Indian Daily Weather Report and Mausam, published by the Indian Meteorological Department.

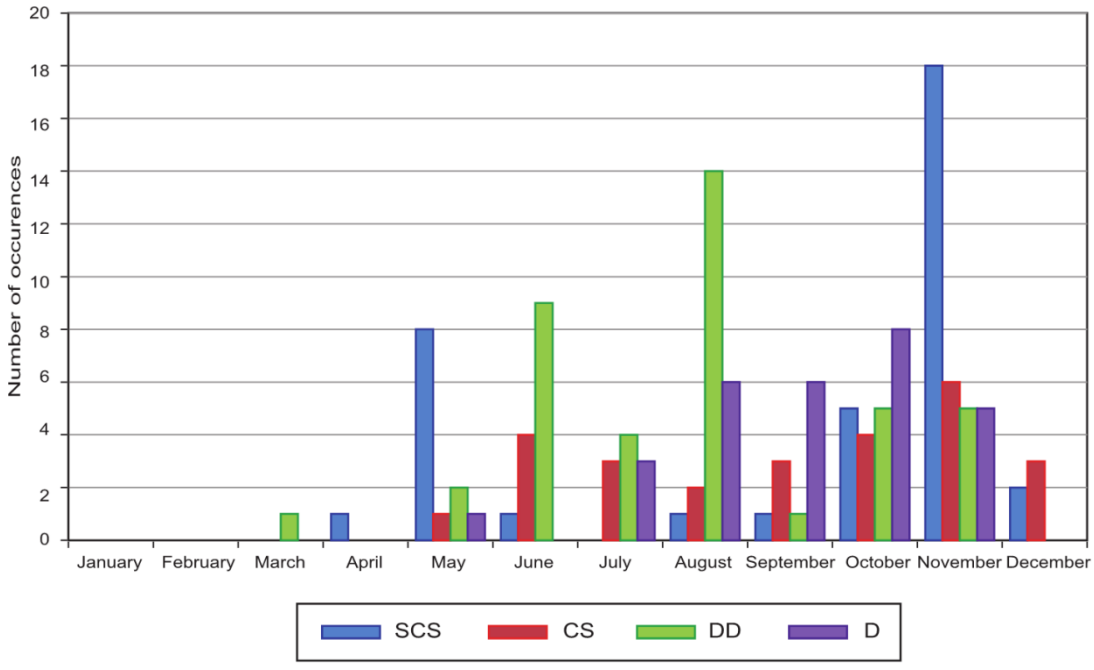

Figure 5.2 Frequency distribution of a) wind speed (knots) (binned into 5 knots) and b) core pressure (hPa) (binned into 5 hPa classes) of cyclones identified during the period 1974 - 2000. Data Source: Indian Daily Weather Report and Mausam, published by the Indian Meteorological Department.

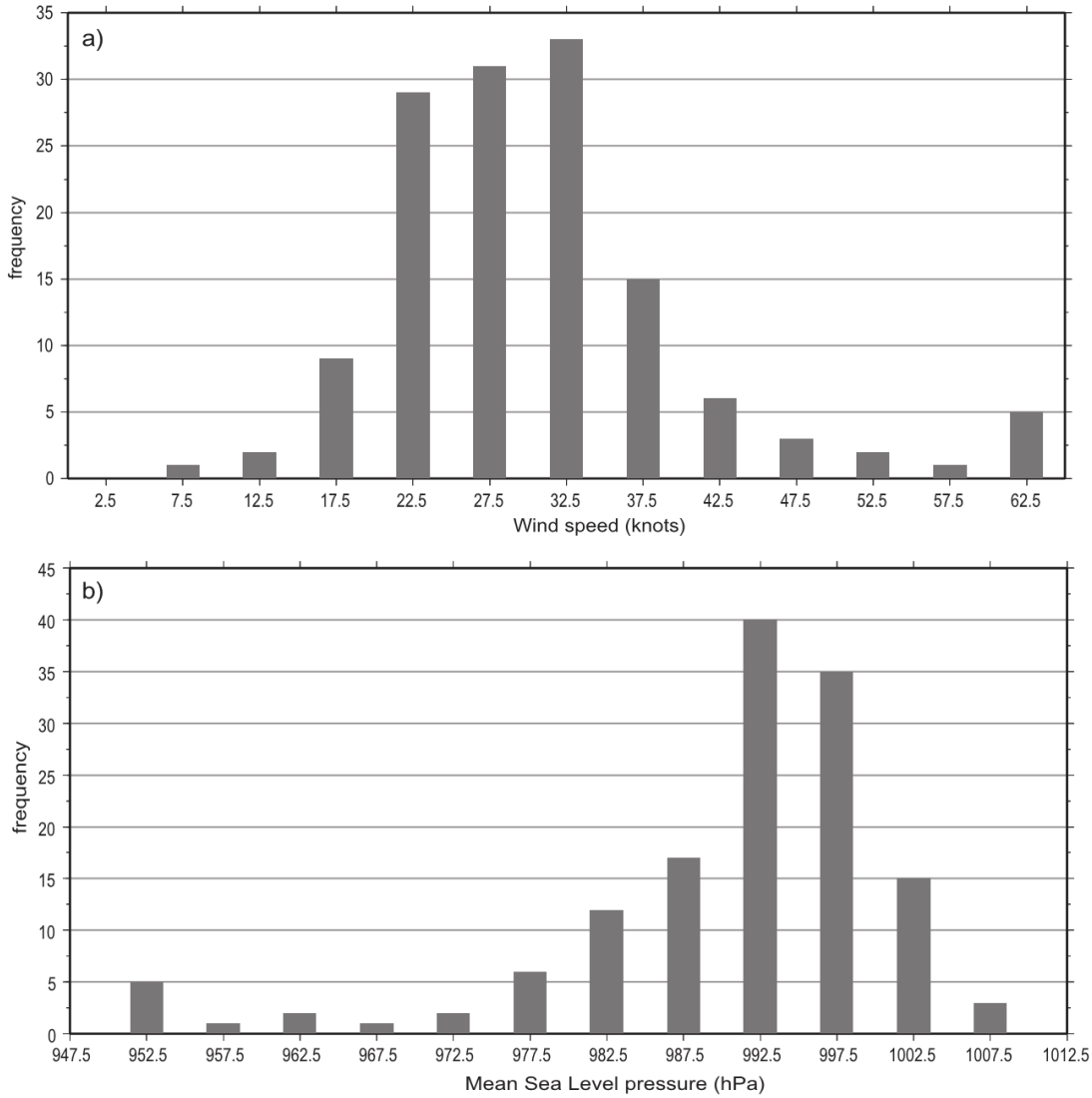

The tracks of cyclones that crossed different coasts of the Bay of Bengal each year and the frequency distribution of events crossing each state along the east coast of India are shown in Figures 5.3 to 5.5 and Figure 5.6, respectively. It is found that along the coast of Bay of Bengal at least three cyclonic events occur every year with maximum number of events not exceeding 7 during the period 1974 -2000. Out of the 136 LPS that formed in the Bay during the specified period, 100 (73%) systems crossed the coast of India, 13 (9%) crossed Bangladesh, 10 (7%) crossed Myanmar and 2 (1%) crossed Sri Lanka and 11 (8%) weekend or dissipated over sea. It is evident from Figure 5.6 that out of the 100 cyclones which crossed the Indian coast during the considered 27 years, Orissa had the largest fraction of 43% followed by Andhra Pradesh with 29%, West Bengal 16% and Tamil Nadu 12%. Orissa had the highest number (37 out of 57) of cyclone during the monsoon months while Andhra Pradesh had the highest frequency of cyclones in the month of October and November (9 out of 18) and some scattered events during the monsoon months.

5.2.4 Schematization

The model domain (Figure 4.7) and the bathymetry (Figure 4.8) for the storm surge model are similar to that of tidal model. The model domain, as shown in Figure 4.1, extends from 1.5°N to 23°N and 79.8°E to 103°E with open boundaries along 79.8°E and 1.5°N.

The storm surge model was driven simultaneously with tides prescribed along the open boundaries and wind forcing and Mean Sea Level Pressure (MSLP) to simulate the surges caused due to each LPS event. The tidal forcing was included in the storm surge model itself, rather than adding the individual tidal model output and the surge model output, in order to take into account the non-linear interaction between tides and surges. The composite tidal elevations at the open boundaries were extracted from FES2004 global tidal model, as described in

Figure 5.3 Tracks of cyclone that formed in the Bay Bengal during the period 1974-1982 in different months. Data Source: Indian Daily Weather Report and Mausam, published by the Indian Meteorological Department.

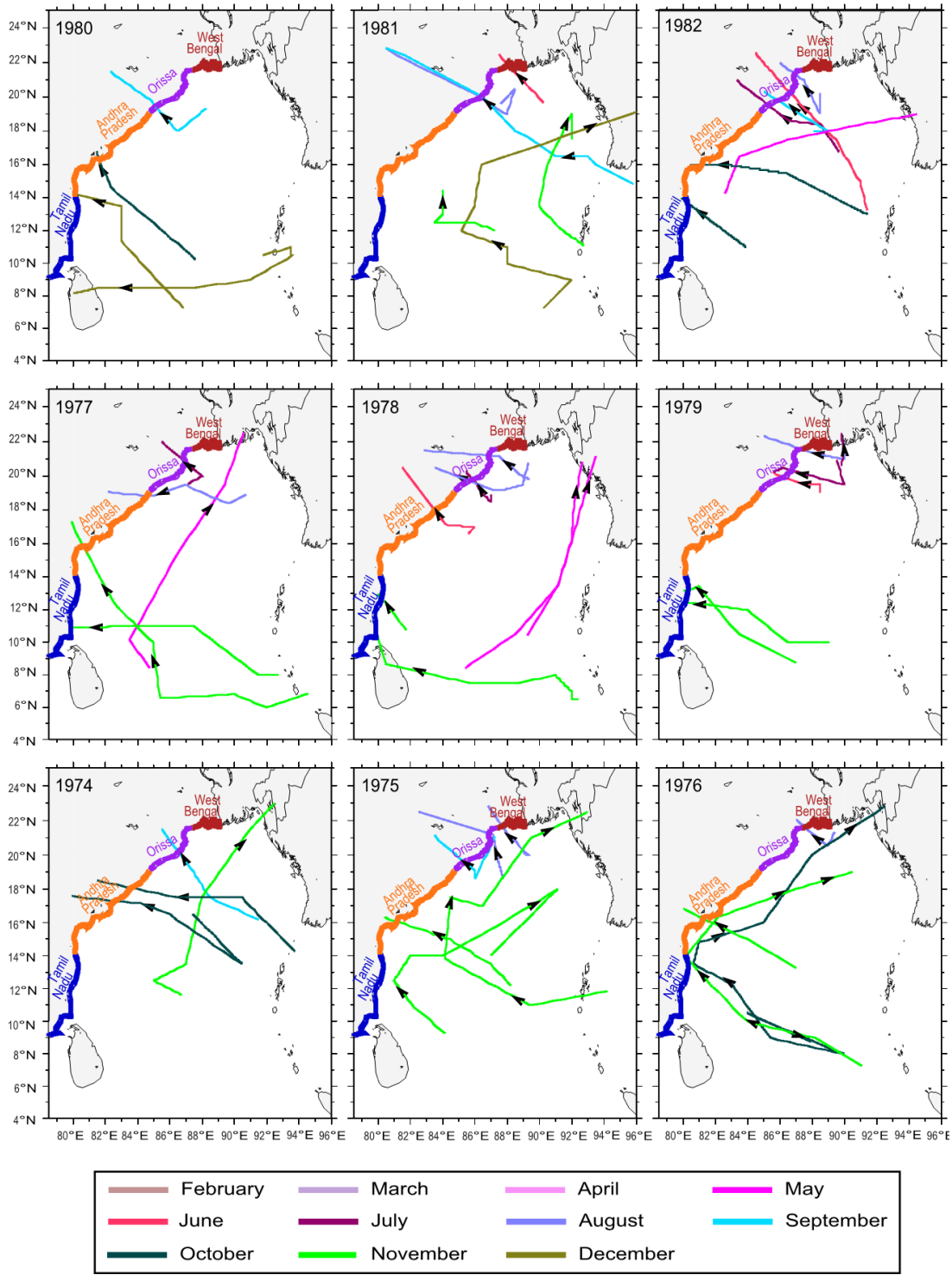

Figure 5.4 Same as Figure 5.3, but for the period 1983-1991.

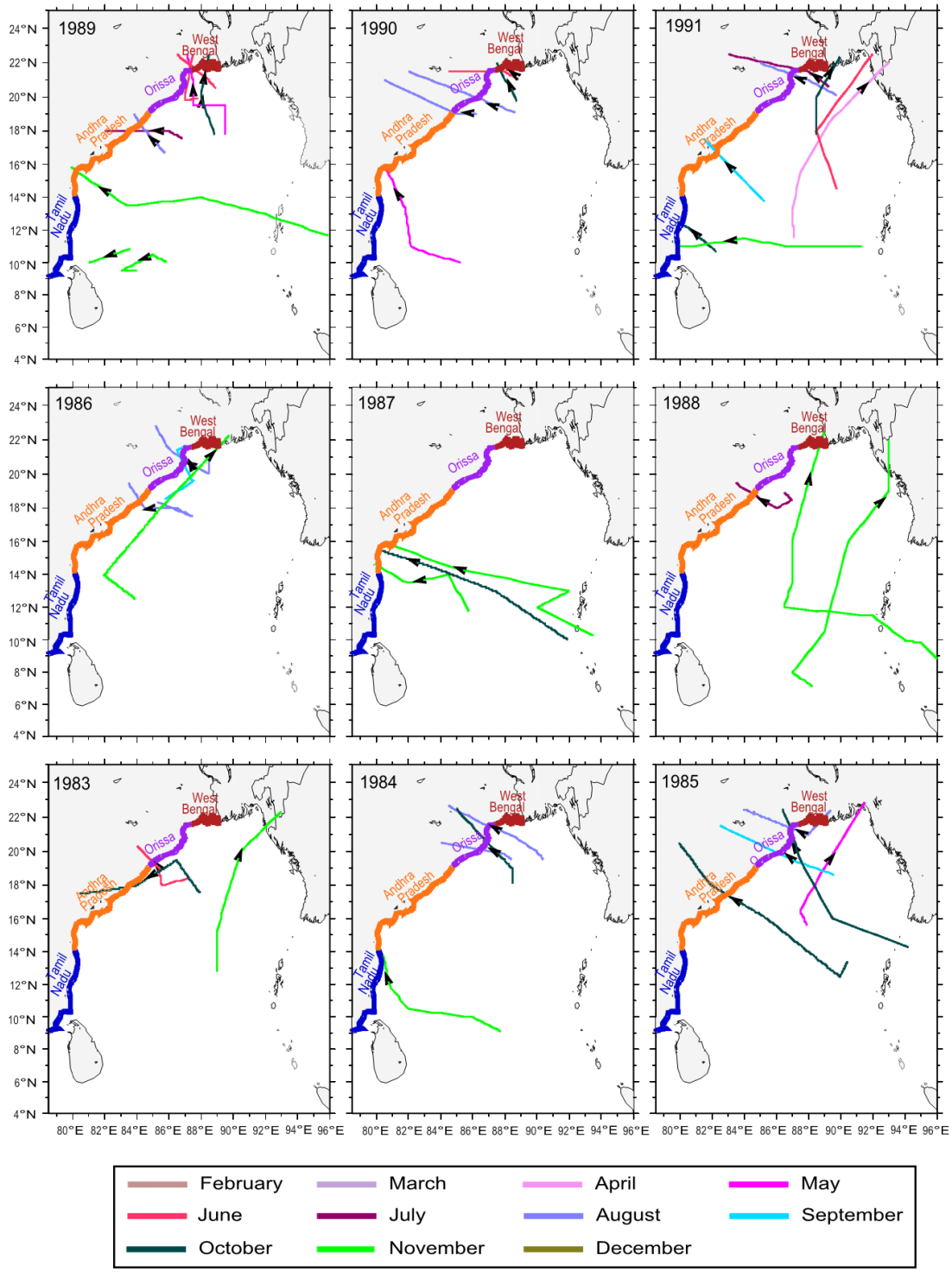

Figure 5.5 Same as Figure 5.3, but for the period 1992-2000.

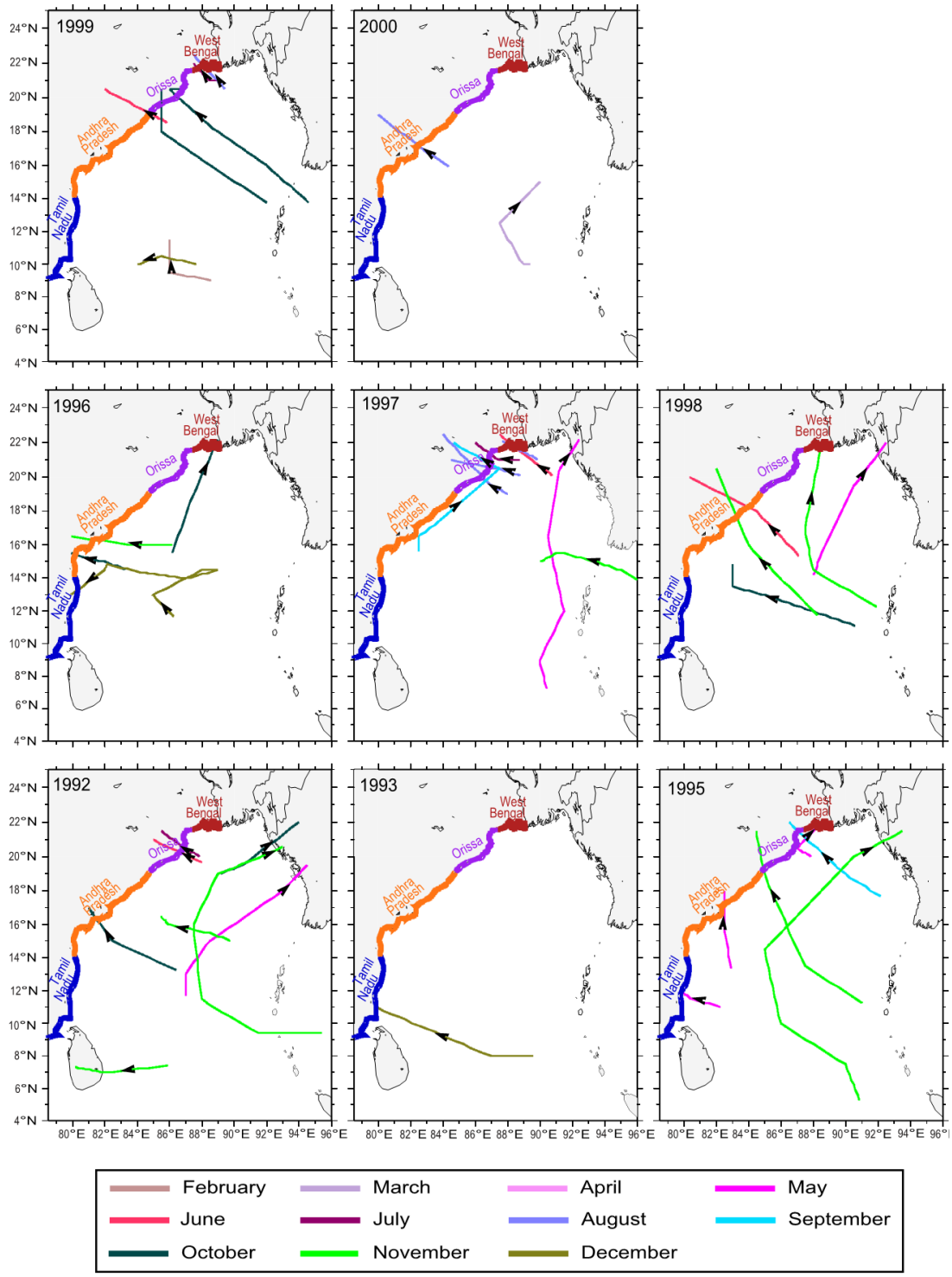

Figure 5.6 Monthly frequencies of cyclones that hit the states of Tamil Nadu, Andhra Pradesh, Orissa and West Bengal located along the east coast of India during the period 1974 – 2000. Data Source: Indian Daily Weather Report and Mausam, published by the Indian Meteorological Department.

.

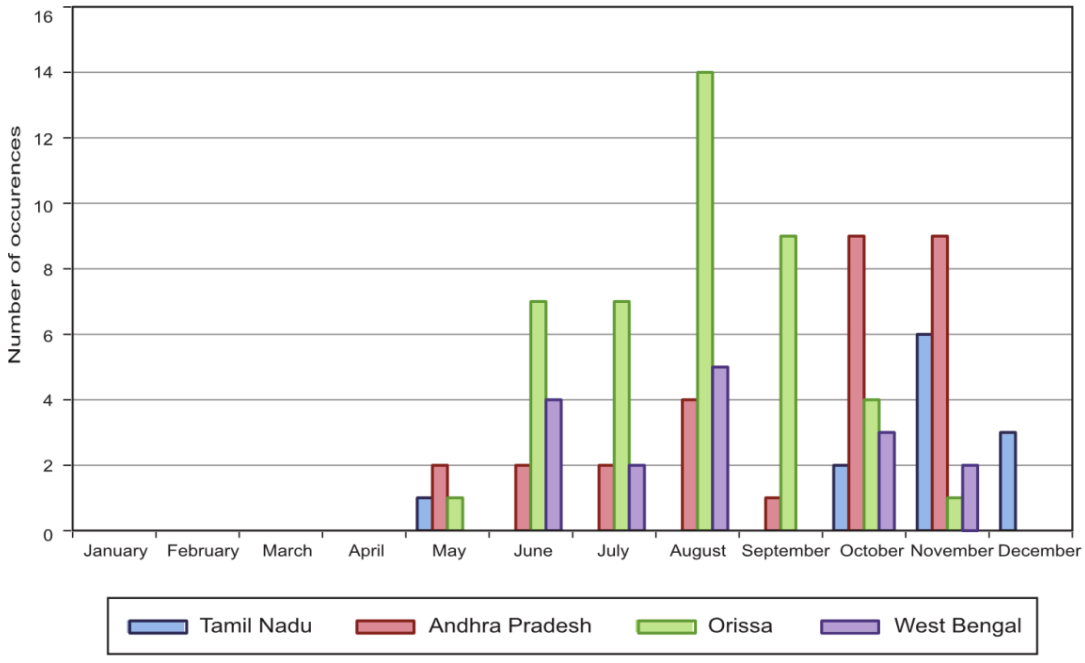

Section 4.2.2, for a period of 15 days starting from 4 days prior to the first day of cyclone formations for each event. In order to derive the meteorological forcing, the core pressure and the position of the cyclone core obtained for each of the 136 events were interpolated to every 3 hours and used in the cyclone model of Holland to derive the MSLP field and wind field (Equations (5.1) and (5.3), respectively) for each grid point and at every time step of the storm surge model. The storm surge model was run 4 days prior to the first day of cyclone formation for all the events to provide sufficient spin-up time. Therefore, the storm surge simulation provided the total sea level and the depth mean current due to combined effect of tide and meteorological forcing. In order to compute the storm surge component of total sea level, the storm surge model was run with tidal forcing alone for each event and the resulting tidal elevations were subtracted from the total sea level.

5.3 Validation of the storm surge model

The model results were validated by comparing the simulated level defined at the grid closest to tide gauge location and the observed hourly tide gauge data at Paradip, Visakhapatnam and Chennai. But the spectral analysis of the time series of observed total sea level as well as the surge level showed annual peaks and some higher frequency peaks, therefore, a band pass filter was applied to them in order to carry out the validation. This filter removed the effect of annual variability as well as the high frequency winds and seiches that are not represented by the surge model. Though the simulation of storm surges were carried out for 136 LPS events that occurred in the past 27 years, the comparison is carried out for total sea level during some selected cyclonic events that crossed Paradip, Visakhapatnam, or Chennai, (tracks shown in Figure 5.7).

Figure 5.7 The tracks of the selected cyclones that caused storm surges at Paradip, Visakhapatnam and Chennai. The storm surges produced due to these cyclonic events at the 3 coastal stations were compared against the available observed sea levels. The coastline of Indian states – Tamil Nadu, Andhra Pradesh, Orissa, and West Bengal are differentiated with different colours.

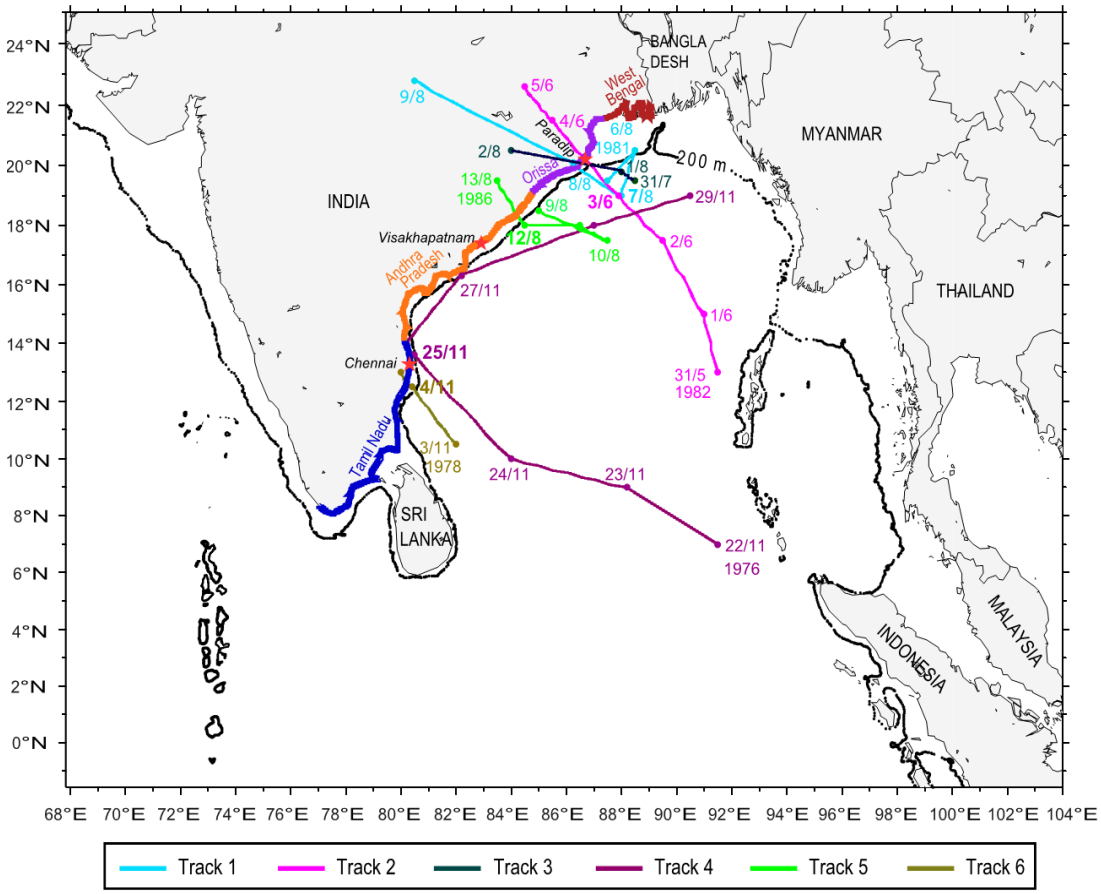

5.3.1 The surge at Paradip due to 7 August 1981 cyclone

A low pressure system was formed over north-western Bay of Bengal on 5 August 1981 and after meandering towards north for a day, it turned, and intensified into a cyclonic storm. Finally, the CS crossed the coast of Orissa at about 40 km north of Puri on the morning of 8 August (Track 1 in Figure 5.7), with a core pressure of approximately 982 hPa, from which the pressure drop and maximum wind speed was estimated to be 28 hPa and 40 knots using Equations (5.1) and (5.4), respectively. The storm surge simulation was carried out from 0000 UTC 1 August to 0000 UTC 9 August 1981. Initially, the model was driven only by tidal forcing until the meteorological forcing was introduced from 0000 UTC 5 August. The model simulation was carried out using tidal forcing alone for the same period so that the surge component could be derived. Figure 5.8a shows the simulated and the observed total sea level with respect to mean sea level at Paradip during the landfall. Figure 5.8a shows that the simulated peak total sea level of 2.5 m agrees well with the observed peak sea level of 2.35 m. The simulated surge at Paradip reached as high as 0.45 m, which is similar to the observed peak surge of 0.43 m.

5.3.2 The surge at Paradip due to 3 June 1982 cyclone

A depression that formed over the central Bay of Bengal on 1 June 1982 intensified into a CS and then into a SCS with its core pressure dropping to 980 hPa on 3 June. The storm crossed the coast of Orissa close to Paradip on 3 June (Track 2 in Figure 5.7). The pressure drop at the core of the cyclone and the maximum wind speed around the core was determined to be 30 hPa and 42 knots. The model was integrated from 0000 UTC 27 May to 0000 UTC 5 June 1982. The meteorological forcing was included in the model from 0000 UTC 31 May. The simulated and the observed total sea level are shown in Figure 5.8b. The simulated peak sea level (2.8 m) and the surge elevations (0.7 m) are in close agreement with those of observed peak levels (2.9 m and 0.8 m), respectively.

5.3.3 The surge at Paradip due to 1 August 1984 cyclone

A deep depression with core pressure 992 hPa developed on 1 August 1984 with its core at 19.8°N, 88°E from a low-pressure system in the northern bay and crossed the coast of Orissa between Puri and Paradip (approximately 25 km north of Paradip) on 1 August (Track 3 in Figure 5.7). The core pressure and thereby the pressure drop just before landfall was found to be 992 hPa and 18 hPa, respectively. The simulation of the surge event was carried out from 0000 UTC 27 July to 0000 UTC 2 August 1984 with meteorological forcing from 0000 UTC 31 July. Figure 5.8c shows a good agreement between the simulated and the observed sea level with peak values of 3.05m and 3.0 m respectively. Model simulation shows a peak surge of 0.33 m at Paradip, which is in close agreement with the observed surge of 0.4 m.

5.3.4 The surge at Visakhapatnam due to 25 November 1976 cyclone

A low pressure system which formed over the southern Bay of Bengal on 22 November 1976, moved northwest, steadily intensified into a DD that skirted the coast of Andhra Pradesh up to 27 November and then finally moved north-eastward to the coast of Arakan weakening into deep depression on 30 November morning (Track 4 in Figure 5.7). The DD had a core pressure of 996 hPa which corresponded to a pressure drop of 14 hPa. The storm surge simulation was started from rest on 0000 UTC 18 November 1976 with the tidal forcing alone and then from 0000 UTC 22 November, the model was driven by tidal forcing as well as the meteorological forcing. From Figure 5.8d, it can be seen that the simulated and the observed sea level matches well with each other with approximately same peak value of 1.6 m. The simulated maximum surge component (0.25 m) matches with the observed maximum surge component (0.22 m).

5.3.5 The surge at Visakhapatnam due to 12 August 1986 cyclone

A deep depression (core pressure less than 992 hPa) that developed from a low-pressure system over north-west Bay of Bengal crossed the coast of northern Andhra Pradesh near Kalingapatnam (approximately 10 km north of it) in the night of 12 August 1986 (Track 5 in Figure 5.7). The lowest pressure recorded was 985 hPa at Kalingapatnam. Initially, the tidal forcing drove the surge model from 0000 UTC 5 August to 0000 UTC 8 August and thereafter the meteorological forcing was also introduced. The simulated peak (1.65 m) and the observed peak (1.8 m) sea level match well (Figure 5.8e). The simulated maximum surge component is 0.1 m, which is less than the observed maximum surge component.

5.3.6 The surge at Chennai due to 4 November 1978 cyclone

A deep depression with a core pressure of 1002 hPa crossed the coast of Tamil Nadu, 50 km south of Chennai, around noon of 4 November 1978 near Cuddalore, weakened into a depression and entered into the Arabian Sea on 5 November (Track 6 in Figure 5.7). The pressure drop and the maximum winds were estimated to be 8 hPa and 20 knots, respectively. The model was allowed to spin up by forcing with tides alone for four days prior to 0000UTC November 3, after which meteorological forcing was introduced in the model. According to observations, Chennai was affected by a peak surge of 0.2 m and a maximum total sea level of 1.2 m (Figure 5.8f) whereas the model simulation shows a maximum surge component of 0.3 m and a peak total sea level of 1.3 m.

Figure 5.8 The time series of total sea level simulated (continuous line) at Paradip due to a) 7 August 1981 cyclone, b) 3 June 1982 cyclone, and c) 1 August 1984 cyclone, at Visakhapatnam due to d) 25 November 1976 cyclone and e) 12 August 1986 cyclone and at Chennai due to f) 4 November 1978 cyclone compared with observed total sea level (dotted line). The tracks of these cyclones are shown in Figure 5.7. The arrow points to the time at which the peak surge occurred at the mentioned station.

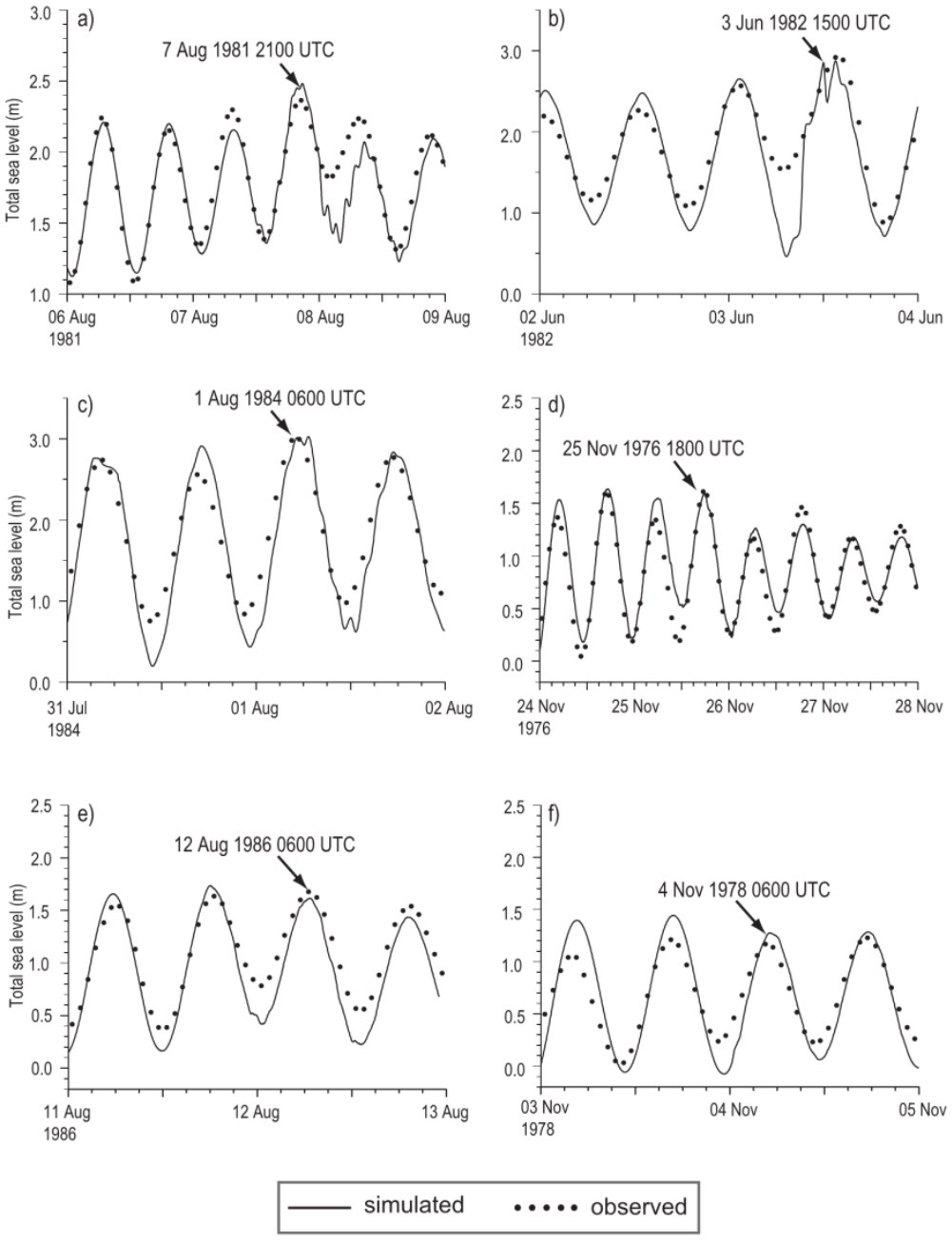

The time series plot of observed and simulated elevations (Figure 5.8) shows the importance of the timing of the surge occurrence. Though the cyclone that hit Paradip on 3 June 1982 was more intense than that of 1 August 1984, leading to a higher surge elevation but the total sea level associated with the former event was much less as compared to that of the latter event. The reason is that the peak surge associated with landfall of 1 August cyclone occurred at the time of high tide at Paradip. Had the peak surge due to 3 June 1982 cyclone occurred 3-4 hours later, the resulting total sea level and damage would have been much higher. Thus it is very important for the forecasters to know the tidal condition of an area and the time of the occurrence of the peak surge during a cyclone event in order to issue a warning.

Figure 5.8 and the error statistics (Table 5.1) for the above events indicate that the model can reproduce the observations reasonably well. The model results could, thereby, be used for the analysis of extreme events in regions where long period observations do not exist.

Table 5.1 Error statistics showing the comparison between the simulated and the observed surge component for stations shown in Figure 5.7**.**

Station name	LPS event	Standard deviation		Mean Error, ME (m)	RMSE (m)
		Observed surge (m)	Simulated surge (m)		
Paradip	08 Aug 1981 03 Jun 1982 01 Aug 1984	0.12 0.17 0.15	0.08 0.07 0.06	-0.001 0.001 0.001	0.08 0.15 0.12
Visakhapatnam	25 Nov 1976 12 Aug 1986	0.04 0.15	0.04 0.05	0.02 0.02	0.06 0.12
Chennai	04 Nov 1978	0.06	0.07	0.04	0.05

5.4 Extreme sea level analysis

The risks associated with storm, as mentioned in Section 1.1.6 can be quantified by estimating the return periods of extreme events which are inversely related to

the exceedance probability of an event. In the present work, we have used the r-largest annual maxima method introduced by Smith [1986] and described by Tawn [1988] which is an extension of the widely used classical annual maximum method of Gumbel [1958]. This method has been chosen as it allows us to use more than one value of extreme sea level for each year, thereby allowing more reliable estimates of return periods with less number of years of data. For the r-largest annual maxima method, we used the software prepared in the Proudman Oceanographic Laboratory, UK [D. Blackman, personal communication], in which the annual maxima can be allowed to have any of the three Generalized Extreme Value (GEV) distributions. We used Gumbel distribution (GEV Type I) following Unnikrishnan et al. [2004]. They extracted the annual maxima for the period 1974-1988 from hourly tide gauge data at Paradip, Visakhapatnam and Chennai and showed that the plot of the annual maxima against a function $(-ln\,(ln\,P))$, where P is the cumulative probability density function, produced a straight line suggesting that Gumbel distribution can be used for the analysis. The cumulative distribution function for Gumbel fit can be written as

$$G(x;\alpha,\beta) = exp\{exp[-(x-\alpha/\beta)]\} \tag{5.11}$$

where, α and β are the location and the scale parameters, respectively. The 'r-largest annual maxima' were selected following the criteria suggested by Tawn and Vassie [1989] that 'r' must be large enough to obtain a reasonable estimate of the parameters and that the values selected should fall in the tail of the distribution. The r-largest maxima approach has been used by Bernier and Thompson [2006]; Lowe et al. [2001]; Flather et al. [1998]; Tsimplis and Blackman [1997] for studying the changes in extreme sea levels due to regional climate change. Bernier et al. [2007] and Marcos et al. [2009] mapped the distribution of extreme sea levels in the Southern Europe and Northwest Atlantic, respectively by applying the r-largest maxima methodology on the available long tide gauge records as well as on the output of a 2D surge model at locations having poor data.

McInnes et al. [2009] estimated storm surge return levels along the south-eastern coastline of Australia by simulating individually the surge events

identified in the tide gauge records for the northern Bass Strait. They performed r-largest GEV analyses with r=2, r=3 and r=4 on the simulated surge heights and selected 2-largest GEV fits to estimate the return levels as it gave smaller uncertainties.

5.4.1 Return periods of extreme events along the east coast of India

The statistical analysis was carried out on the annual maxima of pressure drop (ΔP), simulated total sea level and surge component. For each LPS event in the Bay of Bengal, the surge component maxima were obtained first and then the total sea level maxima were picked up by defining a window width of 48 h consisting of 24 h before and 24 h after the occurrence of peak surge in order to avoid the maxima that may be only due to spring tide. The annual maxima of total sea level and the surge component were then fitted to Gumbel distribution to obtain the scale and the location parameters and thereby the return period was estimated as the reciprocal of Gumbel cumulative distribution function.

The 5-year and 50-year return levels for the total sea level and surge levels were estimated using the annual maxima for the period 1974-2000 for different stations along the east coast of India, selected from the 114 stations shown in Figure 4.7. As seen from Figure 4.7 and Table 4.1, among the 43 stations located along the east coast of India, 5 are Standard Ports and 13 are Secondary Ports. Apart from these port stations, 8 other main stations were also found to be included in these 43 stations, which are tabulated (in italics) in Table 5.2. Therefore, the return levels were estimated for 26 major stations along the east coast of India using the r-largest maxima method. For most of the stations in the present study, it was found that considering ‘r’ greater than 3 led to inclusion of non-extreme values in the extreme value estimation. Therefore, statistical estimations were done for; one maximum per year (r=1), two maxima per year (r=2) and three maxima per year at each station. The sensitivity of the estimates to the value of 'r' used in the analysis is demonstrated in Table 5.2.

Table 5.2 The 5-year and the 50-year simulated return levels at 26 stations along the east coast of India obtained by the analysis of the surge (difference between the total sea level and tidal elevation) maxima through the r-largest annual maxima method. The station numbers correspond to the stations shown in Figure 4.7 and tabulated in Table 4.1. The return levels at each station are given for different 'r' values, one maximum per year (r=1), two maxima per year (r=2), and 3 maxima per year (r=3). The estimated standard errors associated with the return levels are given in brackets. The shelf width (km) at each station grid point is also shown.

St no	Station Name	Shelf Width (km)	5 year return surge level			50 year return surge level		
			r=1	r=2	r=3	r=1	r=2	r=3
10	Nagapattinam	84	0.13 (0.024)	0.11 (0.01)	0.10 (0.012)	0.29 (0.05)	0.22 (0.031)	0.18 (0.023)
11	*Porto Nova*	20	0.10 (0.019)	0.09 (0.01)	0.08 (0.012)	0.22 (0.04)	0.19 (0.03)	0.17 (0.023)
12	Cuddalore	57	0.10 (0.018)	0.08 (0.01)	0.08 (0.011)	0.21 (0.038)	0.17 (0.025)	0.15 (0.02)
13	Pondicherry	71	0.13 (0.025)	0.11 (0.02)	0.10 (0.014)	0.30 (0.053)	0.24 (0.036)	0.21 (0.028)
15	**CHENNAI**	32	0.08 (0.013)	0.07 (0.01)	0.07 (0.01)	0.16 (0.027)	0.14 (0.02)	0.13 (0.016)
16	*Pulicat*	30	0.16 (0.028)	0.14 (0.02)	0.13 (0.016)	0.34 (0.058)	0.28 (0.04)	0.25 (0.031)
18	*Gudur*	40	0.25 (0.041)	0.21 (0.03)	0.19 (0.023)	0.52 (0.085)	0.41 (0.057)	0.36 (0.044)
19	*Nellore*	20	0.12 (0.021)	0.10 (0.01)	0.09 (0.012)	0.26 (0.046)	0.20 (0.03)	0.18 (0.023)
20	*Kavali*	40	0.27 (0.044)	0.21 (0.03)	0.19 (0.024)	0.56 (0.091)	0.42 (0.058)	0.36 (0.045)
22	Surya Lanka	37	0.55 (0.101)	0.46 (0.07)	0.43 (0.058)	1.20 (0.212)	0.96 (0.144)	0.84 (0.113)
24	*Machilipatnam*	100	0.38 (0.066)	0.32 (0.05)	0.30 (0.039)	0.81 (0.138)	0.66 (0.097)	0.57 (0.075)
26	Sacromento Shoal	30	0.13 (0.024)	0.11 (0.02)	0.11 (0.014)	0.28 (0.051)	0.23 (0.034)	0.20 (0.027)
27	**KAKINADA**	50	0.18 (0.026)	0.15 (0.02)	0.14 (0.015)	0.35 (0.053)	0.29 (0.037)	0.25 (0.028)
29	**VISAKHAPATNAM**	49	0.10 (0.014)	0.09 (0.01)	0.09 (0.010)	0.19 (0.03)	0.17 (0.023)	0.16 (0.02)
30	Bhimunipatnam	58	0.23 (0.038)	0.19 (0.03)	0.18 (0.024)	0.49 (0.08)	0.38 (0.054)	0.35 (0.045)
32	Kalingapatnam	44	0.20 (0.034)	0.17 (0.02)	0.16 (0.02)	0.42 (0.07)	0.34 (0.047)	0.30 (0.037)
33	Baruva	55	0.23 (0.037)	0.21 (0.03)	0.19 (0.023)	0.47 (0.07)	0.40 (0.055)	0.36 (0.044)

Table 5.2 Continued

St no	Station Name	Shelf Width (km)	5 year return surge level			50 year return surge level		
			r=1	r=2	r=3	r=1	r=2	r=3
34	Gopalpur	83	0.26 (0.04)	0.22 (0.03)	0.21 (0.026)	0.53 (0.085)	0.44 (0.058)	0.39 (0.048)
35	Chilka Mouth	92	0.34 (0.05)	0.29 (0.04)	0.26 (0.032)	0.67 (0.103)	0.55 (0.071)	0.50 (0.059)
36	*Puri*	85	0.39 (0.053)	0.37 (0.04)	0.34 (0.04)	0.76 (0.114)	0.70 (0.089)	0.63 (0.075)
37	Devi River Entrance	34	0.27 (0.043)	0.24 (0.03)	0.22 (0.026)	0.56 (0.09)	0.46 (0.059)	0.42 (0.05)
38	**PARADIP**	41	0.47 (0.075)	0.41 (0.05)	0.40 (0.046)	0.97 (0.15)	0.78 (0.09)	0.73 (0.086)
39	False Point	65	0.95 (0.014)	0.88 (0.01)	0.83 (0.009)	1.87 (0.28)	1.64 (0.202)	1.52 (0.017)
40	**SHORTT ISLAND**	104	0.73 (0.010)	0.73 (0.08)	0.68 (0.073)	1.40 (0.20)	1.36 (0.162)	1.24 (0.134)
41	*Chandipur*	160	1.57 (0.023)	1.49 (0.19)	1.39 (0.016)	3.10 (0.415)	2.83 (0.36)	2.58 (0.298)
43	**SAGAR ROADS**	195	1.39 (0.187)	1.35 (0.16)	1.35 (0.146)	2.60 (0.368)	2.59 (0.31)	2.46 (0.268)

Though the estimated 5-year and 50-year return simulated surge level showed a decrease of 18% and 25%, respectively with the increase of the number of maxima taken per year, the standard errors associated with them reduced considerably (37% and 43%), respectively, a result of increasing sample size of extreme values and thereby, justifying the use of r=3. Therefore, it was decided to include at least 3 maxima (r=3) per year to estimate the return levels.

The statistical analysis was done on the pressure drop of annual extreme events, to get the return periods of the Δp for the Bay of Bengal (Table 5.3). The 5-year return estimate for pressure drop is found to be 43 hPa, suggesting the occurrence of cyclonic storms, but the 50-year and 100-year return estimate for pressure drop is 61 hPa and 72 hPa which can cause severe cyclonic storms.

The spatial variation of return levels of total sea level along the east coast of India (Figures 5.10a and 5.11a) generally increases towards the head bay, the

lowest being at Nagapattinam and the highest being at Sagar Island, which is similar to the increasing tidal range.

Table 5.3 The return periods of pressure drop (Δp) for the cyclones in the Bay of Bengal region. The Δp, used in the estimate of return period, is given as the difference between the core pressure of each cyclone at the time of crossing the coast and the ambient pressure (1010 hPa).

Return Period (years)	ΔP (hPa)
2	30.5
5	42.7
10	50.8
20	58.6
25	61.1
50	68.7
100	76.2

However, the return levels of surge component (Figures 5.10b and 5.11b) show a different pattern. Along the coast of Orissa, the 50-year return levels are smaller in the southern part than those in the northern part with the highest value of 2.6 m at Chandipur. Chittibabu et al. [2004] obtained a similar trend for the 50-year return levels of storm surge maxima along the coast of Orissa and attributed it to the near-shore topography and orientation of coastline of the region. The variations of the return levels of total water levels at different stations along the east coast of India (Figure 5.11b) are found to be consistent with the nomogram developed by Jain et al. [2010]. However the relatively higher estimates obtained by Jain et al. [2010] as compared to the present study could be probably due to the inclusion of wave setup and the linear addition of tidal amplitudes to the maximum surge levels.

The analysis of Figures 5.10b and 5.11b with respect to Figure 5.9 highlights that shallow and wide continental shelves result in larger surges than

deep and narrow shelves. The stations along the coast of Tamil Nadu show lower 5-year and 50-year return levels of surge component than other stations due to its narrow shelf and deeper bathymetry. Along the coast of Andhra Pradesh, Machilipatnam, Surya Lanka, Kavali and Gudur are found to be sensitive regions as they show considerably high return levels of surge component due to their shallow bathymetry. The 50-year surge level (0.8 m) at Surya Lanka is found to be highest along the coast of Andhra Pradesh, which can be attributed to the geometrical configuration of the coastline forming a cove shaped bay at this area. Though Machilipatnam is deeper (6.1 m) than Surya Lanka (5.0 m) (Figure 5.9), the 5-year and 50-year return levels (0.6 m and 0.3 m, respectively) at this station are comparable to those at Surya Lanka and found to be higher than those at Kakinada (with similar depth of 6.0m) by 40 cm. The reason for this characteristic feature is assessed to be the wide shelf (approximately 100 km) as compared to that of Surya Lanka and Kakinada, where its approx 50 km (Table 5.2), which shows the effect of wide shelf on the height of surge component.

The effect of orientation of coastline on the height of surge component can be discerned at Surya Lanka where the return levels are substantially higher by almost 60 cm than that at Kakinada (shelf width = 50 km) in spite of its narrow shelf (about 37 km) and similar bathymetry. This effect was confirmed by analyzing the surge elevation produced at the two stations due to cyclones of similar intensities. For instance, a deep depression with core pressure of 1000 hPa crossed the coast of Surya Lanka on 16 October 1987 to produce a surge of 20 cm while similar system when crossed the coast of Kakinada on September 1991, produced a surge of 5 cm. The highest return levels for surges are obtained along the coast of Orissa, especially the northern coast because of its very wide shelf and shallow bathymetry. Chandipur is found to be highly prone to extreme events with highest 5-year and 50-year return levels of surges (1.4 m and 2.6 m, respectively) followed by Sagar Roads (1.3 m and 2.5 m, respectively) and False Point (0.8 m and 1.5 m, respectively). The total sea level at Chandipur is lower than that Sagar Roads but the return levels of surge component is the highest which could be due to the geometrical configuration coastline in the region. The

50-year return levels at Paradip and Puri (0.7 m and 0.6 m, respectively) are relatively high compared to the stations in the southern coast of Orissa as they are characterized by relatively shallower depths (Figure 5.9). Though the continental shelf at Chilka and Gopalpur (85 km) are as wide as the shelf at Puri, the return levels at these stations are lower by approximately 10 and 20 cm, respectively due to the deeper depths at these stations.

Figure 5.9 A 3D view of the bathymetry along the east coast of India. The shaded portion represents the depth value at each grid nearest to a land point along the east coast of India. The column and the corresponding value show the depth values at 26 stations along the coast. The stations are marked as numbers that correspond to the numbers in Table 5.2**.**

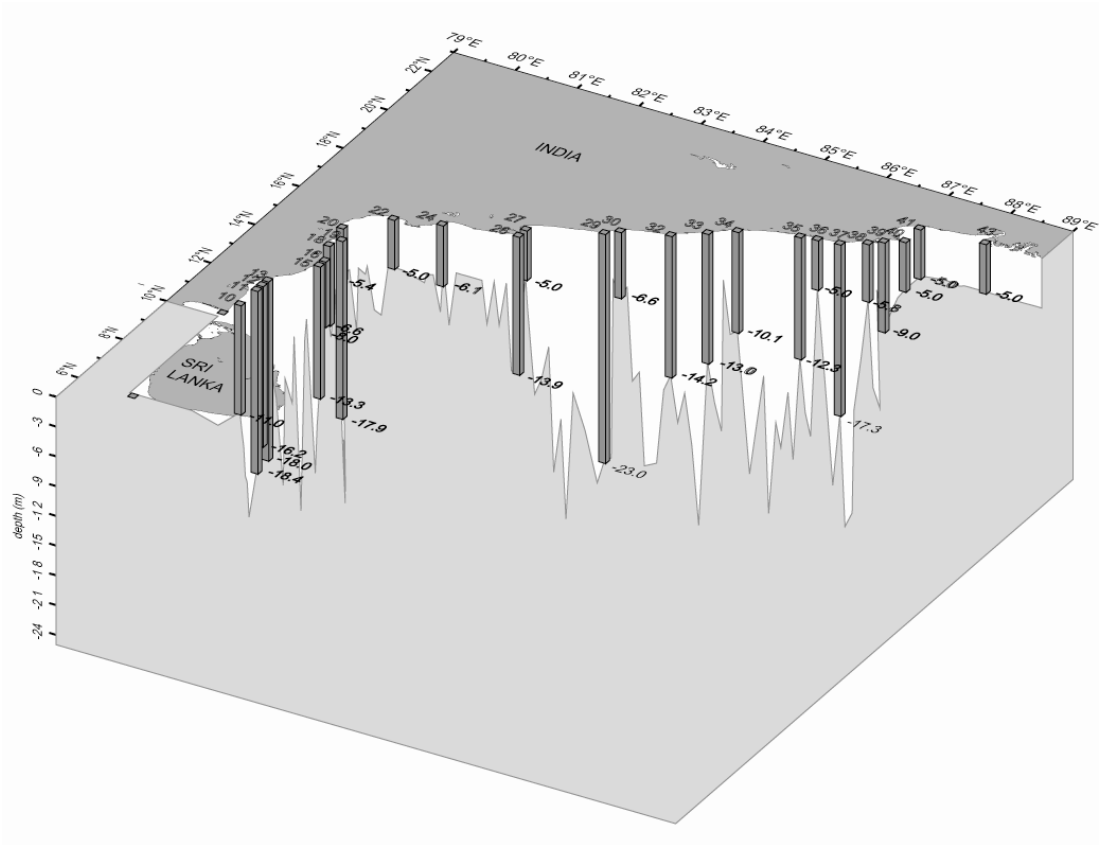

Figure 5.10 The 5-year return a) total sea level and, b) surge level for 26 stations along the east coast of India. The stations are marked as numbers that correspond to the numbers in Table 5.2**.**

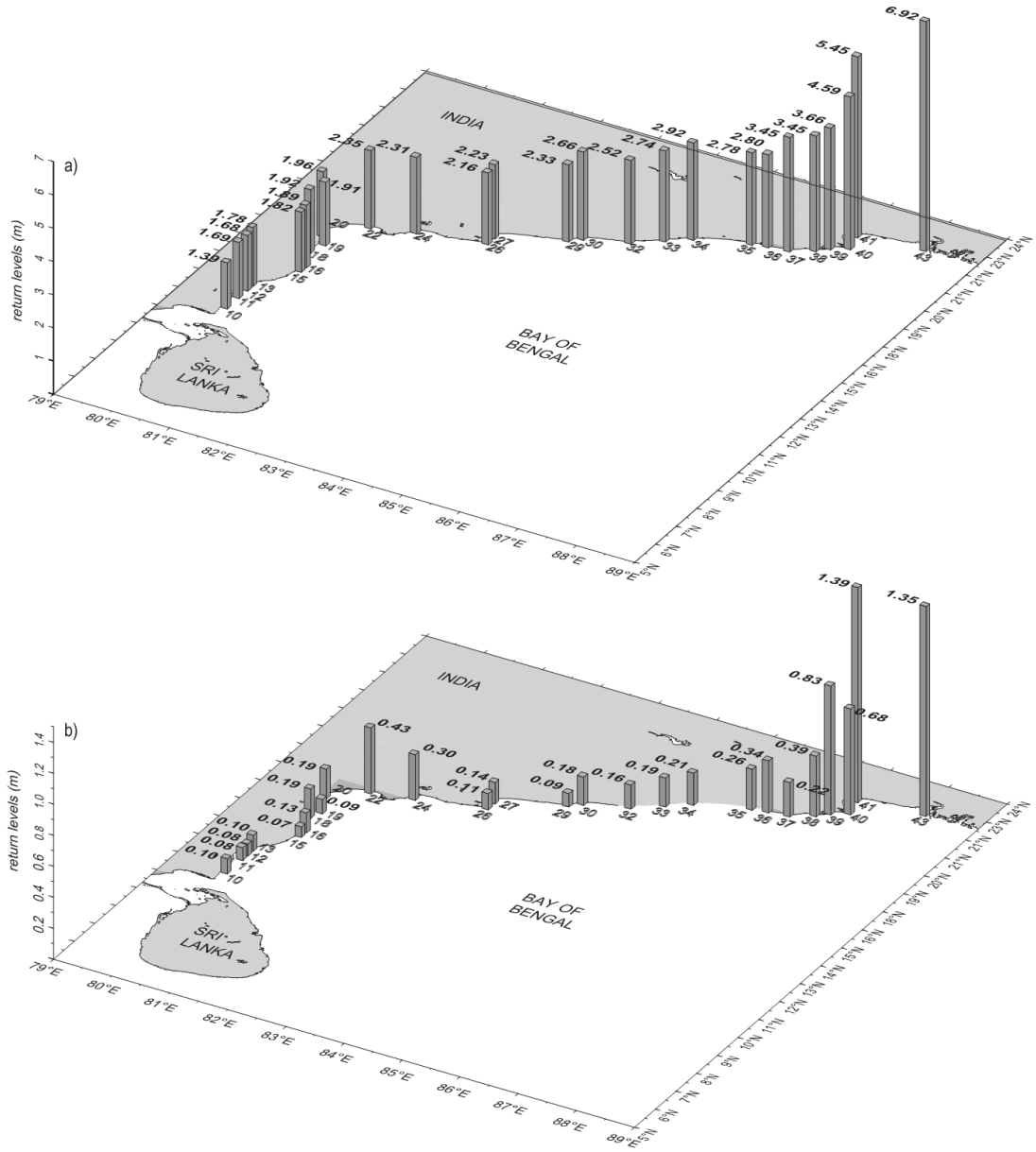

Figure 5.11 The 50-year return a) total sea level and, b) surge level for 26 stations along the east coast of India. The stations are marked as numbers that correspond to the numbers in Table 5.2.

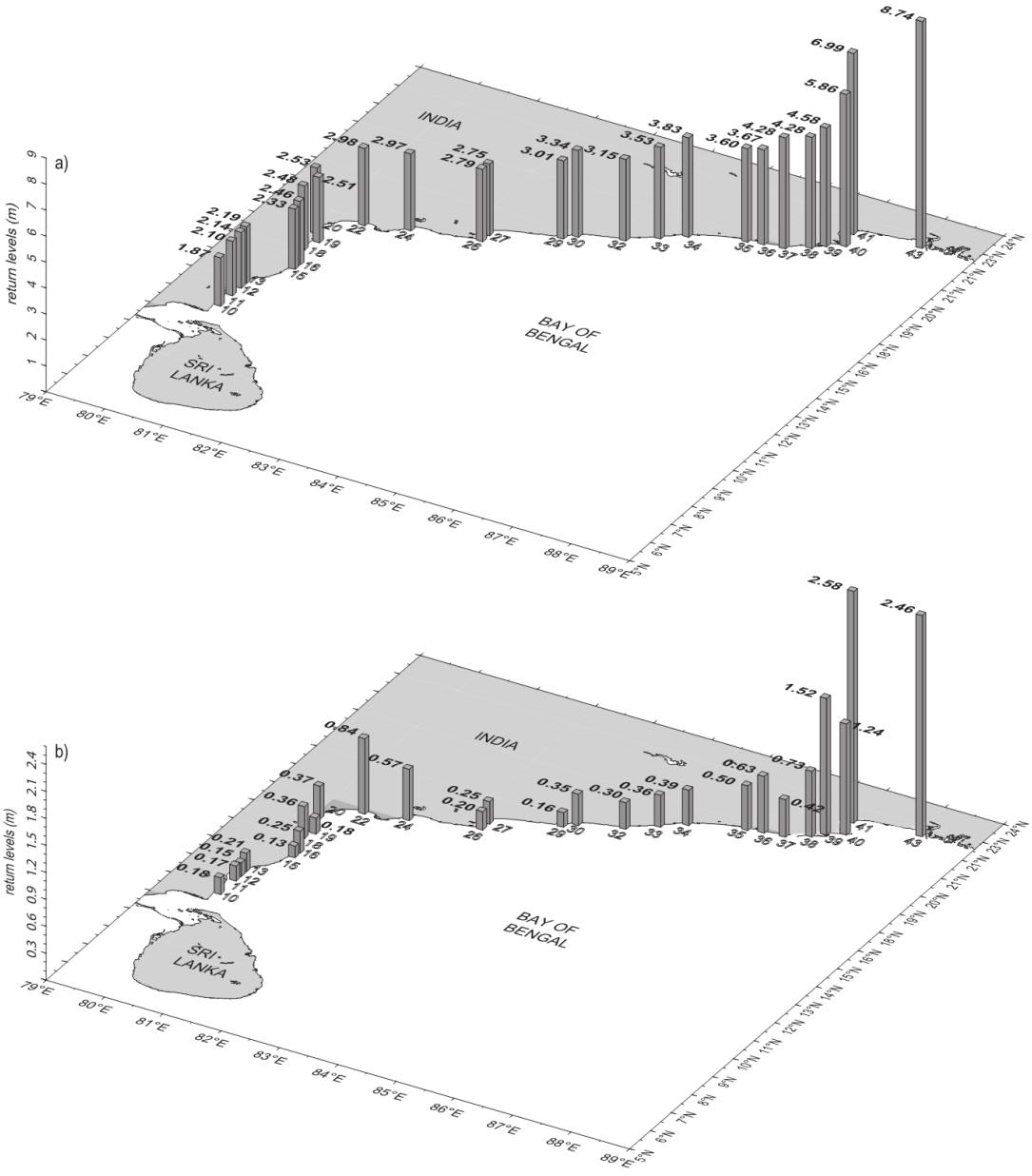

In addition to the 5-year and 50-year return levels, the information on 100-year return levels is also essential for practical purposes, such as design of coastal structures. Therefore, the 100-year return levels for total sea level and surge component, estimated for the 26 stations, are shown in Figure 5.12.

It is noted that the 100-year return level obtained at Chennai, Vishakhapatnam and Paradip are slightly higher than that obtained by Unnikrishnan et al. [2004]. This may be likely due to the fact that they had considered storm surges caused due to cyclones that occurred in a period of 15 years(1974-1988). But in the present study, we have taken into account the cyclones that occurred in the period of 27 years (1974-2000). During this additional period of 12 years, i.e. from 1988-2000, a total number of 64 LPS events occurred in the Bay of Bengal which included the major super cyclones such as the November 1989 SCS that hit Andhra coast and the SCS that hit coast of Orissa and West Bengal in June 1982, April 1991 and October 1999. The simulated storm surge elevations due to these events were also included in the estimation of 5, 50 and 100-year return levels, which are shown in the Figures 5.10, 5.11, and 5.12, respectively.

The 100-year total sea level along the east coast of India is evaluated, on an average, to be 6% higher than the 50-year return levels, with increase being maximum at Nellore where the 100-year return level is higher by 7%. The100-year return level of surge component is estimated to be higher by 14% than the 50-year levels; the highest increase (15%) is found at Cudallore. The pattern in the distribution of 100-year return level along the east coast of India is similar to that of 5-year and 50-year return levels. The comparison of Figures 5.90 and 5.12b imply that the 100-year return levels of surge component are also affected by the geometrical configuration, shelf width and bathymetry. Along the coast of Andhra Pradesh, the highest 100-year surge level is approximately 1 m, observed at Surya Lanka while along the coast of Orissa, the 100-year surge levels reach as high as 3 m at Chandipur.

Figure 5.12 The 100-year return a) total sea level and, b) surge level for 26 stations along the east coast of India. The stations are marked as numbers that correspond to the numbers in Table 5.2.

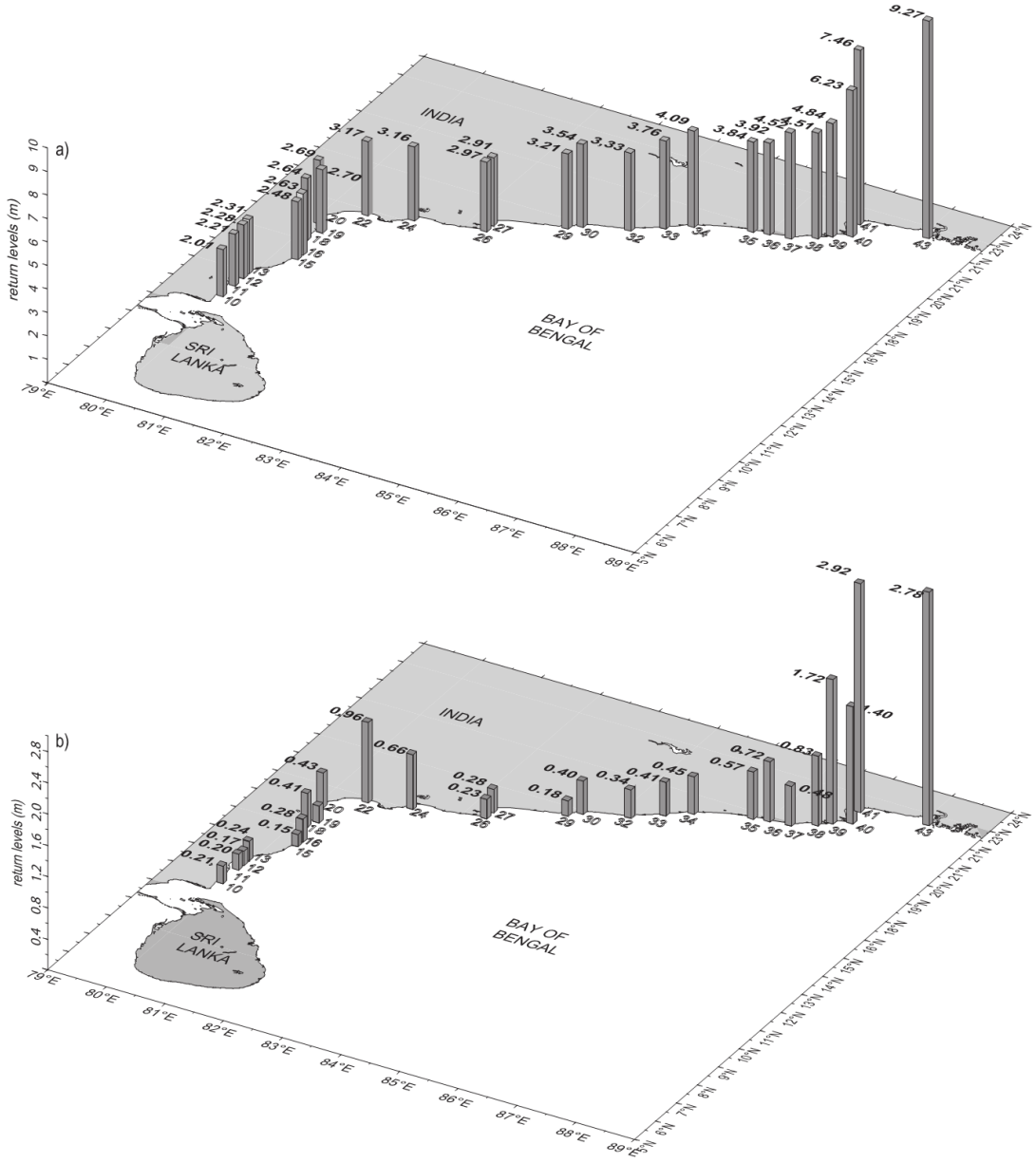

It is therefore shown that, along the east coast of India, the 5-year, 50-year and 100-year return levels of surge components are considerably higher at shallow and wide shelf regions such as Gudur, Kavali, Surya Lanka, Machilipatnam, False Point, Chandipur and Sagar Roads than at deep and narrow shelf regions. Hence accurate bathymetry is a key factor for obtaining accurate model simulation which forms the major advantage of the present work.

5.5 Conclusions

A 2D vertically integrated numerical model was used to simulate storm surge events due to 136 low pressure systems that occurred during the past 27 years (1974-2000) in the Bay of Bengal. The pressure and position of the core at each day of the cyclone development were used in the cyclone model of Holland to derive the wind and pressure field for each of the 136 events. The storm surge model was forced simultaneously with meteorological forcing and tidal forcing, the latter being extracted from the output of global tidal model. The model was also run with tidal forcing alone in order to compute the surge component as the difference between the elevations obtained from the two simulations. A comparison of the simulated total sea level due to some selective events and the observed sea level, obtained from the tide gauges at Paradip, Visakhapatnam and Chennai, showed a good agreement. Moreover, the simulated peak surge components for the same events were also found to agree with the observed peak surge components. The error analysis of simulated surge component corroborated that the model was able to reproduce the observations well.

One of the reasons attributing to the good accuracy achieved by the model could be the use of improved bathymetry data in the simulation. The bathymetry for the model domain was derived from a newly constructed improved ETOPO5 bathymetry dataset which was thoroughly assessed and validated for its accuracy, as described in Chapter 3. The present study, thereby, has the advantage of using a much improved bathymetry dataset for the simulation of storm surges in the Bay of Bengal. In addition, the fine grid resolution of 9 km adopted in the model could also have attributed to the accuracy of the simulated results.

For each year, at least 3 largest events were taken from the simulated total sea level based on the identification of the peak surges. These annual maxima were analysed statistically using r-largest annual maxima method to provide the estimates of return periods of extreme events. Hence, the 5-year, 50-year and 100-year return levels of total sea level and surge component were estimated at 26 stations along the east coast of India.

The return levels (5, 50 and 100-year) of total sea level along the east coast of India show a considerable increase from south to north, with highest value at Sagar Island in West Bengal following the trend of tidal range along Indian coast. However, the return levels of surge components are found to vary spatially depending on the bathymetry, width of continental shelf and orientation of coastline of a region. This is the reason for substantially high return levels at Machilipatnam and Surya Lanka, even though the cyclones developed in the Bay of Bengal generally moves north or north-west, producing more extreme events in the northern part.

The simulation of extreme events of 27 years are considered to be long enough to provide reliable estimates of 5-year, 50-year and 100-year return levels of extreme events along the coast of India. This period includes some of the major super cyclones such as the November 1977 SCS, May 1979 SCS and November 1989 SCS that hit Andhra coast and the SCS that hit coast of Orissa and West Bengal in June 1982, April 1991 and October 1999. Therefore, the present study illustrates that storm surge simulation results can be used to derive the return estimates of extreme events at locations where long period observations of sea level do not exist. The estimated return levels provide useful information for design parameters of offshore and coastal structures.

Chapter 6

Summary

The destruction due to storm surge flooding is a serious concern along the coast of Bay of Bengal. Amongst other natural disasters affecting the coast of India and Bangladesh, storm surges stand out, so far, as the most damaging and as an agent of death and destruction on a scale at least as massive as earthquakes, especially in the head bay region and at some parts along the east coast of India. The high disastrous surges produced at these coastal areas can be caused due to the shallow bathymetry, geometrical configuration of the coastline, wide continental shelf, funnelling effect of the bay and favourable cyclone track. The high death toll could have occurred due to the high population residing in the low-lying coastal areas of India and Bangladesh, which are at higher risks of flooding during cyclonic events. In addition, tidal ranges in the northern Bay of Bengal are very high and the destruction caused by surges can be massive if the surges occur at the time of high tide. Thus real time monitoring and warning of storm surges in the Bay of Bengal is important, for which numerical modelling is the best approach.

As a first step toward simulating the combined effect of tides and surges and prior to the storm surge model, a tidal model was developed to simulate tidal propagation in the Bay of Bengal.

The vertically averaged equation of continuity and the equations of momentum and the numerical techniques used to solve these equations are described in Chapter 2. The model domain has a north-south extension from 1.5°N to 23°N and east-west extension from 79.8°E to 103°E covering the entire Bay of Bengal, with two southern open boundaries along 1.5°N and a western open boundary along 79.8°E. The model domain was spatially discretized into

uniform grids of 5 minute (9.2 km), depending on which the time step was chosen to be 12 seconds.

The major factor that could influence the accuracy of simulated elevations is the actual representation of the bathymetry of the region. The open source datasets such as ETOPO5 are found to have low accuracy in shallow waters (depths less than 200m). Therefore, the lack of open source accurate data for shallow regions encouraged us to develop a modified bathymetric datasets for the region by digitizing the depth contours and sounding depths less than 200 m from hydrographic charts published by Naval Hydrographic Organization. The digitized data was then gridded and combined with ETOPO5 data (masked for depths less than 200m) using appropriate blending techniques. The generation of this dataset is described in Chapter 3. The modified ETOPO5 dataset showed improvements in many regions such as head bay, Gulf of Martaban and around Andaman Island. The improvements in the modified ETOPO5 dataset has been assessed by comparing the tidal elevations simulated using the original ETOPO5 and modified dataset in a tidal propagation model, with the observed tidal levels. With modified dataset, the simulated tidal elevation showed good agreement with the observed levels, while for the original ETOPO5 dataset, the simulated elevations showed lower amplitudes and a shift in phase. Though the domain of the present study covered only Bay of Bengal, the task to generate the reliable dataset was extended to the shallow waters of the entire Indian Ocean. The generation and improvements in the modified dataset for the entire Indian Ocean has been illustrated in Sindhu et al. [2007]. The modified bathymetric data is available in http://www.nio.org/index/option/com_subcategory/task/show/title/Sea-floor%20Data/tid/2/sid/18/thid/113. The data has already been used in many numerical studies [Neetu et al., 2011; Aboobacker et al., 2011; Rao et al., 2010].

The 2D non linear barotropic model, described in Chapter 2, was used to simulate composite tides and the five major tidal constituents (M_2, S_2, N_2, K_1 and O_1). In order to simulate composite tides, the model was driven by tidal elevations extracted from FES2004 and for the simulation of the constituents, the amplitudes and phases of the respective constituent extracted from the FES2004 dataset was

prescribed at the open boundaries. The simulated composite tidal elevations were harmonically analyzed to obtain the amplitudes and phase of the major semi-diurnal and diurnal constituents, which are referred to as model-derived constituents. The model was validated by comparing the simulated composite tides and the model derived constituents with the hourly tide gauge observations available at few stations and the amplitude and phase of the constituents extracted from Admiralty Tide Table, respectively. The root mean square error (RMSE) for the simulated tidal elevation covering a period of 30 days was found to be less than 7.5 cm. The RMSE between the observed and simulated amplitudes (phase) of each of the constituent is; M_2:7.0 cm (9.4°); S_2: 4.4 cm (9°); K_1: 3.5 cm (3°); and O_1: 2.5 cm (38°). The RMS misfit (ORM) is found to be less than 9 cm which illustrates the ability of the model to reproduce the observed tidal characteristics in the region.

In order to analyze the spatial variations in tidal heights and the propagation of tides in the shallow regions of Bay of Bengal, the individually simulated tidal constituents were used to construct co-range and co-tidal charts for each of the five major constituents. The distribution of the semi-diurnal constituents shows a degenerate amphidromic point at the south eastern tip of Sri Lankan coast, but for the diurnal tides it is found to be located along the south-western boundary of the model domain. The semi-diurnal and diurnal tides propagate northward in the central bay, north eastward in the Andaman Sea and southward in the Malacca Strait, with increasing amplitudes. The variation in the amplitudes of diurnal tides across the Bay is very low as compared to the semi-diurnal tides. The detailed analysis of the distribution of semi-diurnal tides in shallow regions such as the head bay, Gulf of Martaban, and Malacca Strait reveals the presence of some characteristic features. The semi-diurnal tides (M_2, S_2, and N_2) are found to amplify nearly twice in the head bay, along the southern coast of Myanmar and in the Gulf of Martaban. The diurnal constituent K_1 amplifies significantly mainly in the north eastern end of the head bay and in the Gulf of Martaban region. The continental shelf in the head bay is wide enough to cause significant amplification of semi-diurnal tides which is in agreement with the Clarke and Battisti [1981]

theory. In the north eastern end of the head bay, the geometrical configuration of the coastline could also contribute to the amplification of semi-diurnal and diurnal constituents. The funnel shaped geometrical configuration of the Gulf of Martaban and wide continental shelf in this region could be the factors responsible for the highest amplification of semi-diurnal tides and relatively significant amplification of diurnal tides in the Gulf. The continental shelf along the southern coast of Myanmar is about 200 km wide and the amplitudes of semi-diurnal tides are doubled in this region while the diurnal tides amplify only marginally, which is in consistent with Clarke and Battisti [1981] theory. In the Malacca Strait, the amplitudes of both semi-diurnal and diurnal tides are found to increase from the northern end to the southern region. Diurnal tides K_1 and O_1 are found to have maximum amplitudes in the Malacca Strait.

Another salient feature observed in the co-tidal and co-range charts of semi-diurnal tide is the presence of degenerate amphidromic point in the head bay and Malacca Strait. However, it is evident from the charts that the magnitude of displacement of amphidromic points away from the central axis to transform into degenerate amphidromic points depends on the bottom friction as well as latitude, as shown by Rizal [2002]. The Malacca Strait (located at 3°N) has a purely virtual amphidromic point for M_2 while the head bay (located at 21°N) is characterized by an easily identifiable degenerate amphidromic point, which agrees with the results of Rizal [2002] who evaluated that the probability of occurrence of virtual amphidromic point decreases with increase in the latitude.

We have, therefore, illustrated in detail the significant characteristics of propagation of tides and the major semi-diurnal and diurnal constituents in the Bay of Bengal, especially in the shallow regions such as head bay, Gulf of Martaban and Malacca Strait, where these studies had been scarce.

Now that the tidal model has been applied to the Bay of Bengal, we modified the 2D vertically integrated tidal model to develop the storm surge model, which has been described in Chapter 5. Storm surges produced due to each of the 136 low pressure systems (LPS) that had occurred in the Bay of Bengal during the past 27 years from 1974-2000, were simulated using the storm surge

model. Out of the 136 LPS that formed in the Bay during the specified period, 100 (73%) systems crossed the coast of India, 13 (9%) crossed Bangladesh, 10 (7%) crossed Myanmar and 2 (1%) crossed Sri Lanka and 11 (8%) weekend or dissipated over sea. It is evident that among the 100 cyclones which crossed the Indian coast during the considered 27 years, Orissa had the largest fraction of 43% followed by Andhra Pradesh 29%, West Bengal 16% and Tamil Nadu 12%. For each of the event, the model was driven simultaneously by tides and wind forcing and MSLP fields. The tidal elevations were extracted from FES2004 and applied at the open boundaries and meteorological forcing, derived from the Holland Cyclone model using the position and core pressure at each day of cyclone development, was applied at each grid point in the form of wind and pressure field. We also simulated the tides alone using the tidal model for the period during which each of the event occurred, so as to compute the surge component as the difference between the elevations obtained from the two simulations. A good agreement was obtained between the simulated total water levels (surge and tide) and observed water levels (RMS error less than 15 cm) caused due to some selected LPS that crossed the coast of Chennai, Visakhapatnam and Paradip.

After validating the model and simulating the total water levels caused by 136 LPS event, we selected, for each event, the peak water levels depending on the time of occurrence of maximum surge component. Thereafter, we sorted out the r-largest total sea level and surge maxima for each year, where '*r*' corresponded to 3. The annual maxima for 27 years were fitted to Gumbel distribution and return periods were estimated as reciprocal of the Gumbel cumulative function. The extreme total water levels and surge component levels corresponding to return periods of 5, 50 and 100 year were computed at 26 stations along the east coast of India. The 5-year and 50-year return levels of total sea level along the east coast of India show a considerable increase from south to north, with the 50-year return total sea levels being as high as 8.7 m and 7.0 m at stations along the north eastern coast such as Sagar Island and Chandipur, respectively. The 100-year total water return levels, being 9 m and 7.4 m, respectively are higher by 7% and 6% as compared to the 50-year return levels at

these two stations, respectively. The high return levels are expected at these stations as the cyclones developed in the Bay of Bengal generally move north or north-west, producing extreme events in the northern part. Moreover, these stations are characterized by high tidal ranges. At some regions in the southern part such as Surya Lanka and Machilipatnam, though 100-year return levels of total sea-level are not very high (3.2 m and 3.2 m, respectively) because of the relatively lower tidal ranges, high return levels of surges (1.0 m and 0.7 m, respectively) are found. In addition to the role of shallow depths (5.0 and 6.1 m, respectively) at the two stations, the high return levels of surges are attributed to the effect of geometrical configuration at Surya Lanka and width (100 km) and orientation of continental shelf at Machilipatnam. Along the coast of Orissa, high return levels are observed at Paradip (0.8 m) and Puri (0.7 m) due to their shallow depths. The highest return level corresponding to 100 year RP for surge component is evaluated to be at Chandipur (3.0 m).

6.1 Concluding remarks

We have illustrated that the storm surge model developed in the present work, is capable of reproducing the observed peak total water levels and surge levels produced due to the passage of a cyclone across a coast. The salient features of the model are:

- Fine grid resolution of 9 km is used.
- Use of newly constructed improved ETOPO5 bathymetry dataset which was thoroughly assessed and validated. It has been illustrated that the use of this improved bathymetry in tidal circulation model produced more accurate results.
- Simultaneous inclusion of tidal elevations and meteorological forcing to drive the storm surge model. This ensures tide-surge interaction which implies accurate simulation of total water levels.
- Large model domain which allows proper representation of the entire track of the cyclone and enables accurate generation and propagation of storm surges

throughout the domain and onto the continental shelf and minimizes the influences of the open boundary condition specification.

- The storm surge model has been developed from tidal model, which itself has been validated and shown to produce accurate results.

The extreme water levels that we have estimated in the present study forms a major input to the design of marine structures built to protect the coast and onshore facilities from huge storms and flooding. However, the total water level is the combined effect of storm surge, high tide and wave set-up. It is evident form the present study that the height of the total sea level at a location during the passage of cyclone depends on the phase of tide at the time of the occurrence of peak surge at that location. Therefore, accurate prediction of wind waves; together with its non-linear interaction with the storm surge is also essential. In order to simulate surges inside the rivers and estuaries, river systems need to be included, which is not considered in the present study.

6.2 Future perspectives

- Simulation methods for including wave set-up in the storm surge models of the Bay of Bengal are not well established yet. Therefore, further studies of inclusion of wave setup are needed.
- Develop coastal inundation models to estimate flooding of low-lying coastal regions in the event of storm surge, which can be applied for real-time cyclone events in order to minimize the damage and allow for pre-planned affective evacuation.
- The present approach of estimating the return levels of extremes events based on the simulation of storm surges caused by LPS systems in the past years can be used to evaluate the return levels in the future climate.

Bibliography

V. M. Aboobacker, P. Vethamony, and R. Rashmi. “Shamal” swells in the Arabian Sea and their influence along the west coast of India. *Geophysical Research Letter*, 38(3):7 pp, 2011.

A. K.Ahuja. Country report on the current status of surveying, mapping and cartographic activities, *Fifteenth United Nations regional cartographic conference for Asia and the Pacific*, Kuala Lumpur, 2000.

O. B. Andersen, P. L. Woodworth, and R. A. Flather. Intercomparison of recent global ocean tide models. *Journal of Geophysical Research*, 100(C12):25261-25282, 1995.

S. D. Attri and A. Tyagi. Climate Profile of India. Technical Report, India Meteorological Department, Pune, IMD Meteorological Monograph No. Environment Meteorology 01/2010:1-129, 2010.

C. Bell, J. M. Vassie, and P. L. Woodworth. POL/PSMSL Tidal Analysis Software Kit 2000. Permanent Service for Mean Sea Level, CCMS Proudman Oceanographic Laboratory, Bidston Observatory, Birkenhead, Merseyside CH43 7RA, U.K, 2000.

N. B. Bernier and K. R. Thompson. Predicting the frequency of storm surges and extreme sea levels in the northwest Atlantic. *Journal of Geophysical Research*, 111:C10009, 2006, doi:10.1029/2005JC003168.

N. B. Bernier, K. R. Thompson, J. Ou, and H. Ritchie. Mapping the return periods of extreme sea levels: Allowing for short sea level records, seasonality and climate change. *Global and Planetary Change*, 57:139-150, 2007.

C. A. Blain, J. J. Westerink, and R. A. Luettich. The influence of domain size on the response characteristics of a hurricane storm surge model. *Journal of Geophysical Research*, 99:18467-18479, 1994.

K. Bury. Statistical Distribution in Engineering. Cambridge University Press, 362 pp, 1999.

A. Butler, J. E. Heffernan, J. A. Tawn, R.A. Flather, and K. J. Horsburgh. Extreme value analysis of decadal variations in storm surge elevations. *Journal of Marine Systems*, 67:189–200, 2007.

D. E. Cartwright and R. D. Ray. Energetics of global ocean tides from Geosat altimetry. *Journal of Geophysical Research*, 96:16897–16912, 1991.

P. Chittibabu, S. K. Dube, P. C. Sinha, A. D. Rao, and T. S. Murty. Numerical simulation of extreme sea levels for the Tamil Nadu (India) and Sri Lankan coasts. *Marine Geodesy*, 25:235–244, 2002.

P. Chittibabu, S. K. Dube, J. B. Macnabb, T. S. Murty, A. D. Rao, U. C. Mohanty, and P. C. Sinha. Mitigation of flooding and cyclone hazard in Orissa, India. *Natural Hazards*, 31:455–485, 2004.

A. M. Choudhury and A. Ali. Prediction of maximum surge heights associated with cyclones affecting Bangladesh - A preliminary investigation. *Nuclear Science and Applications*, 7(B):118-120, 1974.

J. U. Chowdhury. Determination of shelter height in a storm surge flood risk area of the Bangladesh coast. *Water Resources Journal*, ESCAP, Bangkok, ST/ESCAP/SER.C/182:93-99, 1994.

A. J. Clarke and D. S. Battisti. The effect of continental shelves on tides. *Deep Sea Research*, 28A (7):665-682, 1981.

P. K. Das. A prediction model for storm surges in the Bay of Bengal. *Nature*, 239:211–213, 1972.

P. K. Das, M. Miyazaki, and C. P. Jelesnianski. Present techniques of storm surge prediction.*WMO Report* No. 500, Geneva: 87 pp, 1978.

S. K. Dube, P. C. Sinha, and G. D. Roy. The numerical simulation of storm surges a long the Bangladesh coast. *Dynamics of Atmospheres and Oceans*, 9(2):121–133, 1985.

S. K. Dube, A. D. Rao, P. C. Sinha, and P. Chittibabu. A real time storm surge prediction system: An Application to east coast of India. *Proceedings of the Indian Academy of Sciences*, 60:157–170, 1994.

S. K. Dube and V. K. Gaur. Real time storm surge prediction system for the Bay of Bengal. *Current Science*, 68:103–113, 1995.

S. K. Dube, A. D. Rao, P. C. Sinha, T. S. Murty, and N. Bahulayan. Storm surge in the Bay of Bengal and Arabian Sea: The problem and its prediction. *Mausam*, 48:283–304, 1997.

S. K. Dube, P. Chittibabu, A. D. Rao, P. C. Sinha, and T. S. Murty. Extreme sea levels associated with severe tropical cyclones hitting Orissa coast of India. *Marine Geodesy*, 23:75–90, 2000a.

S. K. Dube, P. Chittibabu, A. D. Rao, P. C. Sinha, and T. S. Murty. Sea levels and coastal inundation due to tropical cyclones in Indian coastal regions of Andhra and Orissa. *Marine Geodesy*, 23:65–73, 2000b.

S. K. Dube, P. Chittibabu, P. C. Sinha, A. D. Rao, and T. S. Murty. Numerical modelling of storm surges in the head Bay of Bengal using location specific model. *Natural Hazards*, 31:437–453, 2004.

S. K. Dube, I. Jain, and A. D. Rao. Numerical storm surge prediction model for the North Indian Ocean and the South China Sea. *Disaster and Development*, 1:47-63, 2006.

S. K. Dube, I. Jain, A. D. Rao, and T. S. Murty. Storm surge modelling for the Bay of Bengal and Arabian Sea. *Natural Hazards*, 51:3–27, 2009, doi: 10.1007/s11069-009-9397-9.

S. K. Dube, P. Jismy, and A. D. Rao. Numerical simulation of storm surge associated with severe cyclonic storms in the Bay of Bengal during 2008-11. *Mausam*, 64(1):193-202, 2013.

R. J. Eanes and S. V. Bettadpur. The CSR 3.0 global ocean tide model: Diurnal and semi-diurnal ocean tides from TOPEX/POSEIDON altimetry. *CSR-TM-96-05*, the University of Texas, Centre for Space Research, Austin, Texas, 1996.

G.D. Egbert and S.Y. Erofeeva. Efficient inverse modeling of barotropic ocean tides. *Journal of Atmospheric and Oceanic Technology*, 19:183-204, 2002.

R. A. Flather. A storm surge prediction model for the northern Bay of Bengal with application to the cyclone disaster in April 1991. *Journal of Physical Oceanography*, 24:172–190, 1994.

R. A. Flather, J. A. Smith, J. D. Richards, C. Bell, and D. L. Blackman. Direct estimates of extreme storm surge levels from a 40-year numerical model simulation and from observations. *Global Atmospheric and Oceanic Systems*, 6:165–176, 1998.

G. R. Flierl and A. R. Robinson. Deadly surges in the Bay of Bengal: Dynamics and storm-tide tables. *Nature*, 239:213-215, 1972.

N. L. Frank and S. A. Husain. The deadliest cyclone in history. *Bulletin of the American Meteorological Society*, 52(6):438–444, 1971.

S. K. Ghosh. Prediction of storm surges on the coast of India. *Indian Journal of Meteorology, Hydrology and Geophysics*, 28:157–168, 1977.

A. Goodwillie and working group of GEBCO Sub-Committee on Digital Bathymetry. Centenary Edition of the GEBCO digital Atlas. *User Guide to the GEBCO one minute grid*, 2003 (http://www.bodc.ac.uk/data/online_delivery/gebco).

GRASS Development Team. GRASS 6.0 Users Manual ITC-irst, Trento, Italy, 2005, (http://grass.itc.it/grass60/manuals/html60_user).

E. J. Gumbel. *Statistics of Extreme*. Columbia University Press, New York, 1958.

P. Hall and A. M. Davies. The influence of sampling frequency, non–linear interaction, and frictional effects upon the accuracy of the harmonic analysis of tidal simulations. *Applied Mathematical Modelling*, 29:533-552, 2005.

B. V. Hamon and J. F. Middleton. Return periods of extreme sea levels: the exceedance probability method. *International Hydrographic Review*, LXVI(2):165-177, 1989.

N. S. Heaps. Three-dimensional numerical model for the Irish Sea. *Geophysical Journal of the Royal Astronomical Society*, 35:99–120, 1973.

G. J. Holland. An analytical model of the wind and pressure profiles in hurricanes. *Monthly Weather Review*, 108:1212–1218, 1980.

K. J. Horsburgh and C. Wilson. Tide-surge interaction and its role in the distribution of surge residuals in the North Sea.*Journal of Geophysical Research*, 112:C08003, 2007. doi:10.1029/2006JC004033.

G. D. Hubbert, G. J. Holland, L.M. Leslie, and M. J. Manton. A real time system for forecasting tropical cyclone storm surges. *Weather and Forecasting*, 6:86–97, 1991.

International Hydrographic Bureau. *Tides, Harmonic Constants*; International Hydrographic Bureau, Special Publication No. 26 and addenda, 1930.

International Hydrographic Organisation.IHO Standards for Hydrographic Surveys, Special publication 44, 3rd edition, International Hydrographic Bureau, Monaco, 1987.

F. Jakobsen, M. H. Azam, and M. M. Kabir. Residual flow in the Meghna Estuary on the coastline of Bangladesh. *Estuarine, Coastal and Shelf Science*, 55:587-597, 2002.

F. Jakobsen, M. H. Azam, M. M. Z. Ahmed, and M. M. Kabir. Cyclone storm surge levels along the Bangladeshi coastline in 1876 and 1960-2000. *Coastal Engineering Journal*, 48(3):295-307, 2006.

I. Jain, P. Chittibabu, N. Agnihotri, S. K. Dube, P. C. Sinha, and A. D. Rao. Simulation of storm surges along Myanmar coast using a location specific numerical model. *Natural Hazards*, 39:71-82, 2006.

I. Jain, P. Chittibabu, N. Agnihotri, S. K. Dube, P. C. Sinha, and A. D. Rao. Numerical storm surge prediction model for India and Pakistan. *Natural Hazards*, 42:67-73, 2007.

I. Jain, A. D. Rao, V. Jitendra, and S. K. Dube. Computation of expected total water levels along the east coast of India. *Journal of Coastal Research*, 26(4):681-687, 2010.

I. Jain , A. D. Rao, and K. J. Ramesh. Vulnerability Assessment at Village Level Due to Tides, Surges and Wave Setup, *Marine Geodesy*, 33:245–260, 2010.

E. Jarosz, C. A. Blain, S. P. Murray, and M. Inoue. Barotropic tides in the Bab el Mandab Strait – numerical simulations. *Continental Shelf Research*, 25:1225-1247, 2005.

A. F. Jenkinson. The frequency distribution of the annual maximum (or minimum) values of meteorological elements. *Quarterly Journal of the Royal Meteorological Society*, 81:158–172, 1955.

B. Johns and A. Ali. The numerical modelling of storm surges in the Bay of Bengal. *Quarterly Journal of the Royal Meteorological Society*, 106:1–18, 1980.

B. Johns, S. K. Dube, U. C. Mohanty, and P. C. Sinha. Numerical simulation of the surge generated by the 1977 Andhra cyclone. *Quarterly Journal of the Royal Meteorological Society*, 107:919–934, 1981.

B. Johns, A. D. Rao, S. K. Dube, and P. C. Sinha. Numerical modelling of tide-surge interaction in the Bay of Bengal. *Philosophical Transactions of the Royal Society of London, Series A, Mathematical, Physical and Engineering Sciences*, 313:507–535, 1985.

J.E. Jones and A.M. Davies. An intercomparison between finite difference and finite element (TELEMAC) approaches to modeling west coast of Britain tides. *Ocean Dynamics*, 55:178–198, 2005.

A. Joseph, R. G. P. Desai, P. Mehra, V. SanilKumar, K. V. Radhakrishnan, K. Vijayakumar, K. AshokKumar, Y. Agarwadekar, U. G. Bhat, R. Luis, P. Rivankar, and B. Viegas. Responses of west Indian coastal regions and Kavaratti lagoon to the November 2009 tropical cyclone Phyan. *Natural Hazards*, 57(2):293-312, 2011.

Z. Kowalik and T. S. Murty. *Numerical Modelling of Ocean Dynamics*, World Scientific, 481 pp, 1993.

T. Lay, H. Kanamori, C. J. Ammon, M. Nettles, S. N. Ward, R. C. Aster, S. L. Beck, S. L. Bilek, M. R. Brudzinski, R. Butler, H. R. DeShon, G. Ekström, K. Satake, and S. Sipkin. The Great Sumatra-Andaman Earthquake of 26 December 2004. *Science*, 308:1127-1133, 2005.

T. Lay, H. Kanamori, C. J. Ammon, M. Nettles, S. N. Ward, R. C. Aster, S. L. Beck, S. L. Bilek, M. R. Brudzinski, R. Butler, H. R. DeShon, G. Ekström, K. Satake, and S. Sipkin. Response to Comment on "The Great Sumatra-Andaman Earthquake of 26 December 2004". *Science*, 310:1431b, 2005.

F. Lefevre, F. H. Lyard, and C. Le Provost. FES98: A new global tide finite element solution independent of altimetry. *Geophysical Research Letters*, 27:2717–2720, 2000.

F. Lefevre, F. H. Lyard, C. Le Provost, and E. J. O. Schrama. FES99: A global tide finite element solution assimilating tide gauge and altimetric information. *Journal of Atmospheric and Oceanic Technology*, 19:1345–1356, 2002.

C. Le Provost and M. Fornerino. Tidal Spectroscopy of the English Channel with a numerical model. *Journal of Physical Oceanography*, 15:1009-1031, 1985

C. Le Provost, M. L. Genco, F. Lyard, P. Vincent, and P. Canceil. Spectroscopy of the world ocean tides from a finite element hydrodynamic model. *Journal of Geophysical Research*, 99:24777–24797, 1994.

C. Le Provost, F. Lyard, J. M. Molines, M. L. Genco, and F. Rabilloud. A hydrodynamic ocean tide model improved by assimilating a satellite altimeter-derived data set. *Journal of Geophysical Research*, 103:5513–5529, 1998.

J. A. Lowe, J. M. Gregory, and R. A. Flather. Changes in the occurrence of storm surges around the United Kingdom under a future climate scenario using a dynamic storm surge model driven by the Hadley Centre climate models. *Climate Dynamics*, 18:179-188, 2001.

F. H. Lyard, F. Lefevre, T. Letellier, and O. Francis. Modelling the global ocean tides: modern insights from FES2004. *Ocean Dynamics*, 56:394-415, 2006.

M. Marcos, M. N. Tsimplis, and A. G. P. Shaw. Sea level extremes in southern Europe. *Journal of Geophysical Research*, 114:C01007, 2009, doi:10.1029/2008JC004912.

K. Matsumoto, T. Takanezawa, and M. Ooe. Ocean tide models developed by assimilating TOPEX/POSEIDON altimeter data into Hydrodynamical model: A global model and a regional model around Japan. *Journal of Oceanography*, 56:567-581, 2000.

G. McGranahan, D. Balk, and B. Anderson. The rising tide: assessing the risk of climate change and human settlements in low elevation coastal zones. *Environment and Urbanization*, 19(1):17-37, 2007.

K. L. McInnes, K. J. E. Walsh, G. D. Hubbert, and T. Beer. Impact of sea level rise and storm surges on a coastal community. *Natural Hazards*, 30:187-207, 2003.

K. L. McInnes, I. Macadam, G. D. Hubbert, and J. G. O. Grady.A modelling approach for estimating the frequency of sea level extremes and the impact of climate change in southeast Australia. *Natural Hazards*, 51:115-137, 2009.

F. Mesigner and A. Arakawa. Numerical methods used in atmospheric models. *GARP Publications* Series No. 17, WMO/ICSU Joint Organization Committee, 64 pp.

J. F. Middleton and K. R. Thompson. Return periods of extreme sea levels from short records. *Journal of Geophysical Research*, 91:11707–11716, 1986.

G. B. Mills. International Hydrographic Surveys Standards. *International Hydographic Review*, 75:79-86, 1998.

H. Moe, A. Ommundsen, and B. Gjevik. A high resolution tidal model for the area around the Lofoten Islands, northern Norway. *Continental Shelf Research*, 22:485-504, 2002.

D. A. Mooley and J. Shukla. Main features of the westward-moving low pressure systems which form over the Indian regions during the summer monsoon season and their relation to the monsoon rainfall. *Mausam*, 40:137-152, 1989.

M. T. Murray. A general method for the analysis of hourly heights of the tide. *International Hydrographic Review*, 41(2):91-101, 1964.

T. S. Murty and R. F. Henry. Tides in the Bay of Bengal. *Journal of Geophysical Research*, 88(C10):6069–6076, 1983.

T. S. Murty, R. A. Flather, and R. F. Henry. The storm surge problem in the Bay of Bengal. *Progress in Oceanography*, 16:195–233, 1986.

National Geophysical Data Center. *Data announcement 88-MGG-02*, Digital relief of the Surface of the Earth, National Oceanic and Atmospheric Administration, US Department of Commerce, Boulder, Colorado, USA, 1988.

National Institute of Oceanography. Extreme sea level variability along the coast of India: A report on scenario. *Interim report*. Joint Indo-UK Programme on Impacts of Climate Change in India, Goa, India, 230 pp, 2004, http://drs.nio.org./drs/ bitstream/2264/1191/2/NIO_TR_6_2004_Vol.

S. Neetu, I. Suresh, R. Shankar, D. Shankar, S. S. C. Shenoi, S. R. Shetye, D. Sundar, and B. Nagarajan. Comment on "The Great Sumatra-Andaman Earthquake of 26 December 2004". *Science*, 310:1431a, 2005.

S. Neetu, I. Suresh, R. Shankar, B. Nagarajan, R. Sharma, S. S. C. Shenoi, A. S. Unnikrishnan, and D. Sundar. Trapped waves of the 27 November 1945 Makran Tsunami: Observations and numerical modelling. *Natural Hazards*, 59:1609-1618, 2011.

M. Neteler and H. Mitasova. *Open Source GIS: A GRASS GIS Approach*, Kluwer Academic Publishers, Kluwer, New York, 2002.

N. T. Niyas, A. K. Srivastava, and H. R. Hatwar. Variability and trend in the cyclonic storm over the North Indian Ocean.Technical Report, India Meteorological Department, Pune, IMD Meteorological Monograph No. Cyclone warning 3/2009:1-34, 2009.

D. T. Pugh and J. M. Vassie. Extreme sea levels from tide and surge probabilities. In *Proceedings of the 16th Coastal Engineering Conference, Hamburg, 1978*, American Society of Civil Engineers, New York: 911–930, 1979.

D. T. Pugh. Tides, Surges and Mean Sea-Level. New York, Wiley, 472 pp, 1987.

D. T. Pugh. Changing sea levels. Effects of tides, weather and climate. Cambridge University Press, 280 pp, 2004.

M. F. Qayyum. Prediction of storm surges for Bangladesh coasts by empirical method: Results and discussions. Presented at the *WMO ESCAP 10th Session Panel on tropical cyclones*,22-29 March, 12 pp, 1983.

V. Ramaswamy, P. S. Rao, K. H. Rao, S. Thwin, N. S. Rao, and V. Raiker. Tidal influence on suspended sediment distribution and dispersal in the northern Andaman Sea and Gulf of Martaban. *Marine Geology*, 208**:**33-42, 2004.

A. D. Rao, S. V. Babu, K. V. S. R. Prasad, T. V. Ramana Murty, Y. Sadhuram, and D. K. Mahapatra. Investigation of the generation and propagation of low frequency internal waves: A case study for the east coast of India. *Estuarine, Coastal and Shelf Science*, 88(1):143-152, 2010.

A. D. Rao, I. Jain, and R. Venkatesan. Estimation of extreme water levels due to cyclonic storms: a case study for Kalpakkam coast. *International Journal of Ocean and Climate Systems*, 1, 1-14, 2010.

A. D. Rao, P. L. N. Murty, I. Jain, R. S. Kankara, S. K. Dube, and T. S. Murty. Simulation of water levels and extent of coastal inundation due to a cyclonic storm along the east coastof India. *Natural Hazards*, 2012, doi 10.1007/s11069-012-0193-6.

N. S. B. Rao and S. Mazumdar. A technique for forecasting storm waves. *Indian Journal of Meteorology and Geophysics*, 17:333-346, 1966.

N. S. B. Rao. On some aspects of local and tropical storms in the Indian area. Ph.D. Thesis, University of Jadavapur, India, 262 pp, 1968.

S. Rizal. The role of non-linear terms in the shallow water equation with the application in three-dimensional tidal model of the Malacca Strait and Taylor's Problem in low geographical latitude. *Continental Shelf Research*, 20:1965-1991, 2000.

S. Rizal. Taylor's problem - influences on the spatial distribution of real and virtual amphidromes. *Continental Shelf Research*, 22:2147-2158, 2002.

S. Rizal and J. Sündermann. On the M_2-tide of the Malacca Strait: a numerical investigation. *Deutsche Hydrographische Zeitschrift*, 46(1):61-80, 1994.

R. Robertson, L. Padman, and G. D. Egbert. Tides in the Weddell Sea, In S. Jacobs and R. Weiss, editors, *Oceanology of the Antarctic Continental Shelf, Antarctic Research Series 75*, American Geophysical Union, Washington DC, 1998.

E. W. Schwiderski. Ocean tides, I, Global ocean tidal equations. *Marine Geodesy*, 3:161–217, 1980.

S. S. C. Shenoi, D. Shankar, and S. R. Shetye. Why is Bay of Bengal warmer than Arabian Sea during the summer monsoon? In *Proceedings of the National Symposium METOC - 2004 on Emerging Trends in the Fields of Oceanography and Meteorology*, 05-06 February 2004:87-93, 2004.

S. R. Shetye. Tides in the Gulf of Kutch, India. *Continental Shelf Research*, 19:1771-1782, 1999.

C. K. Shum, P. L. Woodworth, O. B. Andersen, G. D. Egbert, O. Francis, C. King, S. M. Klosko, C. Le Provost, X. Li, J. M. Molines, M.E. Parke, R. D. Ray, M. G. Schlax, D. Stammer, C. C. Tierney, P.Vincent, and C. I. Wunsch: Accuracy assessment of recent ocean tide models. *Journal of Geophysical Research*, 102(C11):25173–25194, 1997.

B. Sindhu, I. Suresh, A. S. Unnikrishnan, N. V. Bhatkar, S. Neetu, and G. S. Michael. Improved bathymetric datasets for the shallow water regions in the Indian Ocean. *Journal of Earth System Sciences*, 116(3):261–274, 2007.

B. Sindhu and A. S. Unnikrishnan. Return period estimates of extreme sea level along the east coast of India from numerical simulations. *Natural Hazards*, 61:1007-1028, 2012.

P. C. Sinha and A. K. Mitra. Tidally induced residual circulation. *Computers and Mathematics with Applications*, 16(1-2):153-167, 1988.

P. C. Sinha, S. K. Dube, A. K. Mitra, and T. S. Murty. A tidal flow model for the Gulf of Kachchh, India. *Marine Geodesy*, 23:117-132, 2000.

P. C. Sinha, I. Jain, N. Bhardwaj, A. D. Rao, and S. K. Dube. Numerical modeling of tide-surge interaction along Orissa coast of India. *Natural Hazards*, 45:413–427, 2008.

R. L. Smith. Extreme value theory based on the r largest annual events. *Journal of Hydrology*, 86:27–43, 1986.

W. H. F. Smith and P. Wessel. Gridding with continuous curvature splines in tension. *Geophysics*, 55**:**293-305, 1990.

M. P. Subeesh. Assessing the consistency of two global tidal models - FES and OTPS - over deep and shallow regions of the Arabian Sea, M.Sc Dissertation, Cochin University of Science and Technology, 1-34, 2010.

Y. M. Tang, P. Holloway, and R. Grimshaw. A numerical study of the storm surge generated by tropical cyclone Jane. *Journal of Physical Oceanography*, 27:963–976, 1997.

J. A. Tawn. An extreme value theory model for dependant observations. *Journal of Hydrology*, 101:227–250, 1988.

J. A. Tawn and J. M. Vassie. Extreme sea levels: The joint probability method revisited and revised. *Proceedings of the Institution of Civil Engineers, Part 2 – Research and Theory*, 87:429–442, 1989.

M. N. Tsimplis and D. Blackman. Extreme sea-level distribution and return periods in the Aegean and the Ionian Seas. *Estuarine Coastal Shelf Science*, 44:79–89, 1997. doi:10.1006/ecss.1996.0126.

UKHO. Admiralty Tide Tables, Volume 3 (2010) – Indian Ocean and South China Sea, NP 203-10. United Kingdom Hydrographic Office, Taunton, 2010.

A. S. Unnikrishnan, S. R. Shetye, and G. S. Michael. Tidal propagation in the Gulf of Khambhat, Bombay High, and surrounding areas. *Proceedings of the Indian Academy of Sciences (Earth and Planetary Sciences)*, 108(3)**:**155–177, 1999.

A. S. Unnikrishnan, D. Sundar, and D. Blackman. Analysis of extreme sea level along the east coast of India. *Journal of Geophysical Research*, 109:C06023, 2004.

A. S. Unnikrishnan, K. R. Kumar, S. E. Fernandes, G. S. Michael, and S. K. Patwardhan. Sea level changes along the Indian coast: Observations and Projections. *Current Science*, 90(3):362–368, 2006.

A. S. Unnikrishnan, M. R. R. Kumar, and B. Sindhu. Tropical cyclones in the Bay of Bengal and extreme sea-level projections along the east coast of India in a future climate scenario. Current Science, 101(3):327-331, 2011.

US National Geospatial-Intelligence Agency. Digital Bathymetric Data Base (DBDB) 5 minute, Fairfax (Virginia), DMA, 1994.

D. Van der Wal and K. Pye. The use of historical bathymetric charts in a GIS to assess morphological change in estuaries. *The Hydrographic Journal*, 110:3-9, 2003.

G. S. Vatsa and R. Kumar. Coastal Mapping and Marine Charts. *Indian Cartographer*, 22:157-161, 2002.

G. S. Vatsa, U. K. Singh, C. M. Doss, and M. P. Gupta. Convergence of Hydrographic Information in Nautical charts. *Indian Cartographer*, 22:166-171, 2002.

P. Wessel and W. H. F. Smith. New version of the Generic Mapping Tools released. *EOS Transanctions, American Geophysical Union*, 76:329, 1995, http://www.agu.org/ eos_elec/95154e.html.

P. Wessel and W. H. F. Smith. New improved version of GMT released. *EOS Transanctions, American Geophysical Union*, 79**:**579, 1998.

World Meteorological Organization (WMO). Tropical cyclone operational plan for the Bay of Bengal and the Arabian Sea. *Tropical Cyclone Programme*, Report No. TCP21, 2010.

J. Wu. Wind stress coefficients over sea surface from breeze to hurricane. Journal of Geophysical Research, 87(C12):9704–9706, 1982, doi:10.1029/ JC087iC12p09704.

Annexure: Published Papers